

Electronic Theses and Dissertations, 2004-2019

2019

Multiphase Flow Modeling of Molten Metal Atomization at High Gas Pressure

Kalpana Hanthanan Arachchilage
University of Central Florida

 Part of the [Mechanical Engineering Commons](#)
Find similar works at: <https://stars.library.ucf.edu/etd>
University of Central Florida Libraries <http://library.ucf.edu>

This Doctoral Dissertation (Open Access) is brought to you for free and open access by STARS. It has been accepted for inclusion in Electronic Theses and Dissertations, 2004-2019 by an authorized administrator of STARS. For more information, please contact STARS@ucf.edu.

STARS Citation

Hanthanan Arachchilage, Kalpana, "Multiphase Flow Modeling of Molten Metal Atomization at High Gas Pressure" (2019). *Electronic Theses and Dissertations, 2004-2019*. 6788.
<https://stars.library.ucf.edu/etd/6788>

MULTIPHASE FLOW MODELING OF MOLTEN METAL ATOMIZATION AT
HIGH GAS PRESSURE

by

KALPANA MADHUSHAN HANTHANAN ARACHCHILAGE
B.Sc.Eng (Hons), University of Moratuwa, Sri Lanka, 2011

A dissertation submitted in partial fulfillment of the requirements
for the degree of Doctor of Philosophy
in the Department of Mechanical and Aerospace Engineering
in the College of Engineering and Computer Science
at the University of Central Florida
Orlando, Florida

Fall Term
2019

Major Professor: Ranganathan Kumar

© 2019 KALPANA MADHUSHAN HANTHANAN ARACHCHILAGE

ABSTRACT

The high-pressure gas atomization is well known as one of the best powder manufacturing processes due to its controllability over powder size distribution. However, with the continuous improvement of new alloys, optimizing the operating parameters to maximize the yield is costly and time-consuming. Therefore, it is essential to understand the high-pressure gas atomization process and the effects of different operational parameters on the powder size distribution.

Two-phase numerical simulations are performed to capture the interfacial dynamic during the atomization process and to obtain the effects of gas pressure, melt flow rate, and thermophysical properties of atomizing gas and the molten metal. The Volume of Fluid (VOF) model is used to capture the melt-gas interface, and in-house post-processing code is developed to obtain the droplet size distributions. Three-dimensional geometry of an annular-slit close-coupled gas atomizer is utilized to investigate the primary atomization process. The current grid resolution is sufficient for capturing primary atomization and some characteristics of the secondary atomization, but it is not adequate to capture all the length scales in secondary atomization. Qualitative comparisons of the cumulative volume graphs indicate that this numerical approach is capable of capturing the trends in the atomization process as in the experiments. It is found that a combination of several interfacial instabilities governs the atomization process. Simulations corresponding to different gas pressures show that the atomization characteristics remain unchanged irrespective of the gas pressure. However, it is found that the rate of the evolution and the effectiveness of the atomization process increases

with the gas pressure. Three melts (aluminum, steel, and an artificial material with intermediate thermophysical properties) are used to investigate the effects of the molten metal properties and found that the rate of the atomization process decreases with increasing melt density, and the yield of the atomized powder is seen to increase. The flow characteristics remain unchanged for all three melts. The melt flow is strongly correlated with flow characteristics and interfacial instability.

ACKNOWLEDGMENT

First and foremost, I wish to thank my advisor, Dr. Ranganathan Kumar, for his guidance and support throughout my graduate career. I am grateful to Dr. Yongho Sohn, Dr. Alain Kassab, and Dr. Bhimsen Shivamoggi, who served as my committee members and gave me valuable feedback towards the successful completion of my dissertation. I am also grateful for all the research and teaching faculty at Department of Mechanical and Aerospace Engineering for the delightful experiences I gained as a student and a teaching assistant. Further, I thank all the great teachers I had since my childhood, especially Dr. A.G.T. Sugathapala, Dr. P.A.B.A.R Perera, and Dr. Y.W.R Amarasinghe for their guidance and support at University of Moratuwa, Sri Lanka.

I want to take this opportunity to thank Dr. Le Zhou and Sharon Park at the Advanced Materials Processing and Analysis Center at University of Central Florida for providing me with the experimental results to validate my numerical approach. Further, I would like to thank Dr. Brandon McWilliams and Dr. Kyu Cho at Weapons and Materials Research Directorate at U.S. Army Research Laboratory for providing the financial support to complete my dissertation. I thank Dr. Paul Wiegand and his staff at UCF Advanced Research Computing Center at University of Central Florida for providing the computational resources and support in obtaining the results presented here.

I wish to thank Dr. Carlos Velez for introducing and teaching the first steps of OpenFOAM, opensource software, which I used extensively in my graduate career. I also should thank my friends and colleagues at the University of Central Florida; Ashkan Davanlou, Pretam Choudhury, Eduardo Castillo, Jonathan Wehkin, James Wilson, Majid

Haghshenas, Mohammad Nooranidoost, Tianyi Li, Bryan Palogan, Andres Cuberlo, and Raghu Veera Manikantachari Kancherla for being the awesome friends anyone could ever ask for. Especially thanking James Wilson for the invaluable conversations, we had on OpenFOAM and research in general.

I take this opportunity to thank my Sri Lankan friends, who have been there for me different phases of my life. I especially thank Nadun Kuruppumullage, Thiwanka Sanjitha, Singith Abeysiriwardena, Navindra Wijeyeratne, Mafaz Zafer, Peshala Thibbotuwawa Gamage, Dhanushka Kularatne, Lakshitha Premathilake, Chathura Wickramaratne, and Milinda Yapa, for being there with me at rough times of my life.

Special thanks to my parents and my sisters for continuously encouraging me and being there for me at every point of my life. I am genuinely blissful for having you all in my life, and nothing in my life would have been possible without you. Last but not least, I wish to thank my beautiful wife, Ashini Jayasinghe. Ever since I met her, she has been the most supportive person in my life. I am grateful for being the best critique of my life and bringing out the best in me. With that, I would like to thank all the great people I mentioned above and could not mention by name, for everything you did for me.

TABLE OF CONTENTS

LIST OF FIGURES	ix
LIST OF TABLES.....	xiii
CHAPTER 1 - INTRODUCTION.....	1
CHAPTER 2 – LITERATURE REVIEW	4
Metal Powder Production Methods	4
High-Pressure Gas Atomization	7
Experimental Studies	11
Numerical Investigations	13
Eulerian – Eulerian Numerical Methods for Interfacial Flows.....	19
Numerical Challenges in Atomization Simulations.....	21
CHAPTER 3 – NUMERICAL MODEL AND CASE SETUP	23
Assumptions and Simplifications in the Simulations	23
Governing Equations	25
Turbulence Modeling.....	28
Post-Processing of the Droplet Size Data	31
Droplet Size Distribution Algorithm	31
Symmetry Boundaries and Identifying Droplets that Leave the Computational Domain.....	34

Droplet Sphericity and Aspect Ratio	36
Simulation Case Setup	37
Computational Grid Comparison	45
Experimental Comparison	48
CHAPTER 4 – DYNAMICS OF ATOMIZING MOLTEN ALUMINUM	51
Interfacial Instabilities in Atomization	51
Interfacial Dynamics	52
Processing of Droplet Size Distributions	62
CHAPTER 5 – EFFECT OF OPERATIONAL PARAMETERS ON THE ATOMIZATION PROCESS AND THE DROPLET SIZE DISTRIBUTION	71
Effect of the Gas Pressure on the Atomization Process	73
Effect of the Melt Properties on the Atomization Process	77
Effect of the Gas Properties on the Atomization Process	87
Effect of the Melt Flow Rate on the Atomization Process	89
CONCLUSIONS	94
LIST OF REFERENCES	98

LIST OF FIGURES

Figure 1 – Classification of metal powder production methods	6
Figure 2 – Schematic of the high-pressure gas atomization process	7
Figure 3 – Basic atomizer geometries, a. Close-coupled atomizer b. Free-fall atomizer.....	9
Figure 4 – Gas inlet types, a. Annular-slit gas nozzle, b. Discrete gas nozzles....	10
Figure 5 – Volume of Fluid (VOF) and Level Set (LS) approaches	19
Figure 6 – Sample mesh with cell numbers. Blue color represents the cells that satisfy the condition ($\alpha \geq ath$)	32
Figure 7 – Cell appending algorithm	33
Figure 8 – Schematic of a 2-D ligament and aspect ratio calculations.....	37
Figure 9 – a. Atomization chamber, b. Gravity-driven melt pouring into the atomization chamber. Photo credit – Laboratory of Materials and Coatings for Extreme Environments, Advanced Materials Processing and Analysis Center at University of Central Florida	38
Figure 10 – Schematic of the atomization assembly. All the dimensions are in mm scale.....	39
Figure 11 – Grid size distribution of three computational grids.....	40
Figure 12 – a. Computational geometry and initial volume fraction distribution (red color – melt stream, blue color – gas stream) b. Localized grid refinements corresponding to mesh 3	42
Figure 13 – Droplet size distribution at 2 ms – effect of grid resolution.....	46

Figure 14 – Normalized cumulative volume – the effect of the grid resolution...	47
Figure 15 – Normalized cumulative volume, a. Experimental results (discrete gas atomizer), b. Simulation results (annular-slit gas atomizer).....	49
Figure 16 – Atomization physics – time evolution of the melt and atomizing gas interaction (Al-N, 1 MPa – mesh 3). Note – until 0.5 ms; images show only up to 30 mm from the melt-tip. 0.75 and 1 ms images show up to 50 mm from the melt-tip. The area enclosed in a white circle is zoomed in to emphasize the dynamics of the melt stream ..	54
Figure 17 – Breakup mechanism of a 3-D melt structure at 1 MPa	56
Figure 18 – Vorticity and turbulence intensity variation with the breakup. 2-D color plots represent the vorticity and turbulence intensity at the mid-plane (45° plane in 90° wedge)	57
Figure 19 – Secondary atomization process – ligament breakup (color scheme – interface normal vorticity, red and yellow – positive values and blue – negative values)	59
Figure 20 – Ligament formation (primary atomization process) – zoomed views show the interfacial dynamics (molten steel atomization) in the domain of 15 to 30 mm from the melt-tip in the axial direction. The used time frames are from 0.35 ms to 0.5 ms with 0.05 ms time intervals.....	62
Figure 21 – Time evolution of the number of droplets along the axial direction (blue – droplet $AR \leq 2$, yellow – droplet $AR > 2$).....	63
Figure 22 – Time evolution of the number of droplets – post-processing droplet size data.....	64

Figure 23 – Time evolution in the number of droplets, a) all the droplets compared to those at $Z > 75$ mm domain b) mean diameter variation ($Z > 75$ mm and $AR < 2$).....	65
Figure 24 – Cumulative volume graphs, a. Experimental Results (Close-coupled, discrete gas atomizer), b. Simulation results – the effect of droplet discrimination (close-coupled, annular-slit gas atomizer).....	68
Figure 25 – Droplet size distributions, a. all droplets (2.4 ms), b. discriminated droplets (2.4 ms, $Z > 75$ mm), c. time evolution of the discriminated droplet size distributions.....	69
Figure 26 – Time evolution comparison of 1 and 2.5 MPa gas pressures	73
Figure 27 – Effect of gas pressure (Mesh 3), a. time evolution of the number of droplets, b. time evolution of mean diameter ($Z > 75$ mm, $AR < 2$).....	74
Figure 28 – Normalized cumulative volume, a. Experimental results (close-coupled, discrete gas atomizer), b. Numerical results – mesh 1 (close-coupled, annular-slit gas atomizer).....	76
Figure 29 - Time evolution of the melt and gas interaction (effect of melt properties).....	78
Figure 30 – Early stages of the atomization process – vorticity (2-D images show the cross-sectional view at 30° . The black color contours show the melt-gas interface (melt is present at the left side of the contour). The color plots indicate the vorticity perpendicular to the cross-section. Yellow color represents the vorticity vector pointing towards the page, and the blue color represents the opposite direction.....	80

Figure 31 - Time evolution of the number of droplets – effect of melt properties, a. Original distribution, b. Updated distribution.....	81
Figure 32 - Mean droplet velocities as a function of droplet diameter at 2 ms – effect of melt.....	82
Figure 33 - Normalized cumulative volume graphs – effect of molten metal properties.....	84
Figure 34 - Droplet size distributions (2 ms) – $Z > 75$ mm (blue color – droplets with $A.R \leq 2$, yellow color – droplets with $A.R < 2$).....	85
Figure 35 - Time evolution of mean diameter – effect of melt properties (Cases 7, 8 and 9, 2.0 ms, $Z > 75$ mm, $AR < 2.0$).....	85
Figure 36 – Effect of atomizing gas on the aluminum atomization process, nitrogen (top row), argon (bottom row).....	88
Figure 37 – Effect of the atomizing gas on aluminum atomization, a. The size distribution of the secondary atomized droplets, Aluminum – Nitrogen (left), Aluminum – Argon (right), b. Comparison of normalized cumulative volume of the secondary atomized droplets (2 ms).....	89
Figure 38 – Time evolution of melt-gas interaction – effect of melt flow rate (cases 7, 11, and 12).....	90
Figure 39 – Effect of melt flow rate (cases 7, 11, and 12), a. time evolution of the number of droplets, b. normalized cumulative volume, c. droplet size distribution.....	91

LIST OF TABLES

Table 1 – Grid Statistics.....	41
Table 2 – Boundary Conditions	43
Table 3 – Thermophysical properties of aluminum melt and nitrogen.....	51
Table 4 – Simulation Matrix	71
Table 5 – Thermophysical Properties	72
Table 6 – Characteristic time scales – effect of inlet gas pressure	75
Table 7 – Characteristic time scales – effect of melt properties	86
Table 8 – Characteristic time scales – effect of melt flow rate.....	93

CHAPTER 1 - INTRODUCTION

Demand for metal powder manufacturing has increased immensely within the last decade due to the continuously growing applications in rapid prototyping, injection molding, cold or hot isostatic pressing, powder forging, and additive manufacturing. Metal powder used in additive manufacturing is required to have precisely tailored metal powder with a specific size, shape, and morphology (Motaman, Mullis, Cochrane, & Borman, 2015). Annual worldwide metal powder production exceeds 700,000 tons, and the powder sizes ranging from 0.1-1000 micrometers. In addition to the common metals and alloys such as steel and aluminum, nickel and cobalt-based superalloys are also available in powder form. Many powder production methods have been developed over the years and tailored for different metals/alloys and applications. However, tailoring powder manufacturing processes to obtain a particular quality powder is not always economically feasible.

Among many powder manufacturing methods, high-pressure gas atomization (Alan Lawley, 1978; Motaman et al., 2015) is considered as the most effective and energy-efficient method. It is a commercial metal powder manufacturing method, and it is known for its superior controllability over the powder size distribution (Anderson, White, & Dehoff, 2018; Motaman et al., 2015). In high-pressure gas atomization, pressurized gas is utilized to atomize the molten metal or the alloy. The kinetic energy transferring from the high-pressure gas to the molten metal stream deforms (Firmansyah et al., 2014) the melt stream into ligaments which then break up into droplets of size ranging from micron to millimeter. The surface tension forces tend to make these droplets

spherical, and the large temperature gradients across the melt-gas interface result in rapid solidification (Alan Lawley, 1978; Mates & Settles, 2005a). The timescales in which these forces take place vary, which determines the shape of the solidified powder. Since gases usually have relatively low thermal conductivity, the solidification process is relatively long. Therefore, the gas atomization process often produces spherical metal powder (Alan Lawley, 1978).

The atomization process can be divided into two categories as primary and secondary atomization. Bulk liquid stream deforming into ligaments and large droplets are categorized as primary atomization in atomization literature. Secondary atomization occurs when these ligaments and droplets further breaking up into smaller droplets. Several studies have been performed to study these two breakup mechanisms (Kaiser, Li, Yang, & Lee, 2018; Mates & Settles, 2005b, 2005a; Motaman et al., 2015; Shinjo & Umemura, 2010, 2011a, 2011b; Umemura & Wakashima, 2002). Even though gas atomization is one of the widely used methods in industrial scale, higher operating cost is one of its most significant issues (Kaiser et al., 2018). Nitrogen is often used as the atomizing gas due to cost limitations. To obtain a higher solidification rate, some applications required to have more expensive atomization gases with higher heat transfer coefficient (Rai, Lavernia, & Grant, 1985) (i.e., argon). Therefore, it is necessary to optimize melt-gas interaction and understand how expanding gas affects the atomization process. Many studies have been performed considering different operating parameters and atomizer geometries to optimize the powder atomization process. Physics governing the secondary atomization process (Reitz & Diwakar, 1986, 1987; Sadhal, 2011; Zeoli &

Gu, 2008a) is extensively studied in using experimental, numerical, analytical approaches. However, the primary atomization process in high-pressure gas atomization has not been satisfactorily examined. Since primary atomization characteristics significantly vary with the operational and geometrical parameters, understanding the effects of these parameters on the primary atomization is crucial for optimization purposes (Shinjo & Umemura, 2010, 2011b). The primary purpose of current investigation is to fill this void by accurately capturing the two-phase flow phenomenon and obtaining trends in powder yield for different operational.

CHAPTER 2 – LITERATURE REVIEW

This chapter provides an overview of previous research work on metal powder production methods followed by the experimental and numerical investigations performed on different gas atomization processes.

Metal Powder Production Methods

To date, many metal powder production methods have been developed, and the suitable method has been selected based on the metal/alloy, cost, and powder specifications required for the intended application. Lawley (Alan Lawley, 1978) divided the powder production process into four main categories, such as chemical, mechanical (Zhang, 2004), electrolytic (Basak, Krishnan, Kumar, Abdullah, & Anantharaman, 2014), and atomization (Metz, Machado, Houabes, Elkhatib, & Hassanzadeh, 2008). Figure 1 shows the classification of metal powder production methods. Chemical methods often use a metal compound and a reducing agent. Tungsten powder (Alan Lawley, 1978) is typically prepared by using ammonia or hydrogen as the reducing agent and managed to obtain powders in the range of 1-7 μm . Electrolytic methods use electrodeposition phenomenon to gather high-quality fine particles near electrodes. Particle sizes can be controlled by adjusting the physical properties of electrolytes, electrodes, and voltages. This method is extensively used for copper, beryllium, nickel, and tin powder production. High energy processes like ball, hammer, or roll mills are categorized under mechanical means. These methods are extensively used in flake powder production for the paint and

ink industry (iron, copper, etc...). In the atomization methods, molten metals or alloys go through a forced atomization process.

This process can be further categorized as gas atomization, water atomization (Saeedipour, Schneiderbauer, Plohl, Brenn, & Pirker, 2017), gas-solid (two-phase atomization) (Si, Tang, Zhang, Wang, & Wu, 2017), and centrifugal atomization (Lagutkin, Achelis, Sheikhaliev, Uhlenwinkel, & Srivastava, 2004). Water atomization uses pressurized water jets to atomize the melt. Apart from the low energy efficiency, the process provides irregularly shaped powder often with rough oxidized surfaces. It is due to the higher thermal conductivity (i.e., the heat conductivity of the water is much higher than that of gases) and the active chemical interaction with the atomizing medium. In the gas-solid atomizer, high-pressure gas is mixed with solid particles to increase momentum of the continuous phase. The pressure-swirl gas atomization (Xing gang Li & Fritsching, 2017) is a hybrid atomization method, which introduces a swirl at the melt inlet in addition to the high-pressure gases. The centrifugal forces acting on the melt stream facilitates creating liquid sheets, which then easily atomized using high-pressure gases.

Chen et al. (Chen et al., 2018) investigated the production of Ti-6Al-4V powders obtained from gas atomization, plasma rotating electrode process, and plasma atomization. Micro-structure, porosity, and pore features are examined and found that the porosity and pore size of the powders highly depends on the powder size. The powder obtained from the gas atomization showed the highest porosity.

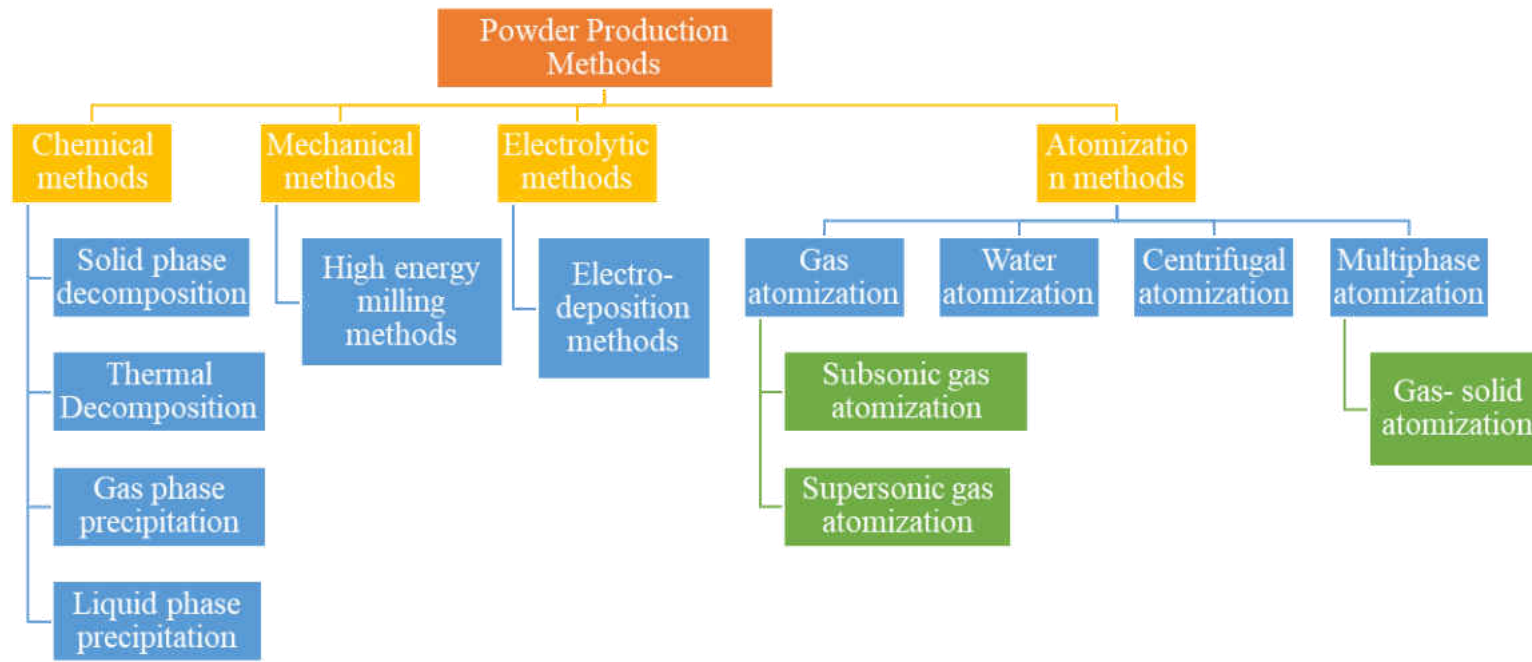


Figure 1 – Classification of metal powder production methods

High-Pressure Gas Atomization

Figure 2 shows a schematic of the high-pressure gas atomization process. Initially, the metal or alloy must be heated above its melting temperature (i.e., alloys need to be heated above its liquidus temperature corresponding to the composition). Usually, melt superheats of 200 to 300 K is maintained to avoid solidification at the melt-tip, obstructing the melt flow. The molten melt is then poured into the crucible and let it flow into the atomizer under gravity. With a time delay, the high-pressure atomizing gas is introduced to the atomizer. It is a common practice in powder manufacturing industries to introduce the gas flow with a delay to reduce the melt backflow so that it will not clog the melt-tip.

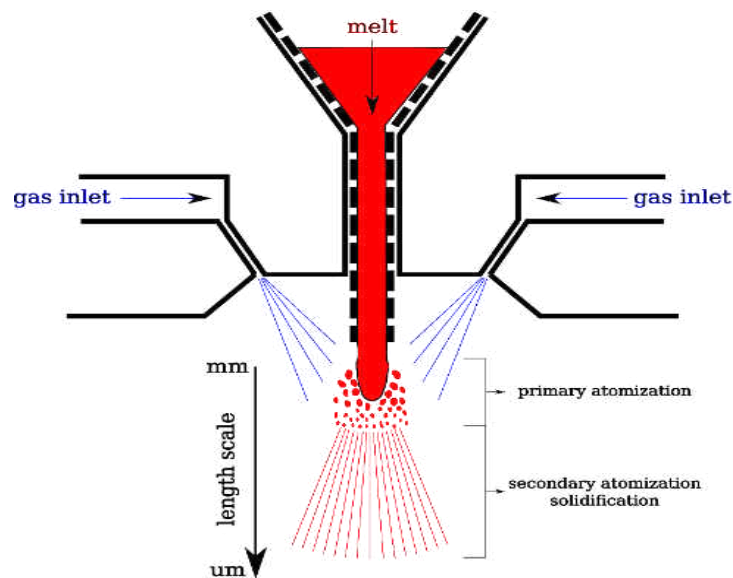


Figure 2 – Schematic of the high-pressure gas atomization process

Once the pressurized atomizing gas introduced into the atomization chamber, it goes through a sudden expansion, gaining higher momentum. Also, the temperature

of the gas drops significantly, creating a steep temperature gradient across the melt-gas interface. The melt-gas interaction initiates near the melt-tip. Initially, the melt stream is forced to deform, forming sheets and ligaments. These ligaments will eventually break up into smaller droplets, as shown in Figure 2. The length scales reduce from millimeter (length scale of the melt-tip) to micrometer scale. Heat and momentum transfer through the gas-melt interface facilitates the atomization process. The rate of interfacial transfer depends on the driving potential and the interfacial area. The cumulative interfacial area increases with the atomization process, facilitating more interfacial transport. These increments in the interfacial transport will increase the break-up process by several order of magnitudes (Fritshing & Uhlenwinkel, 2012).

Different types of nozzle geometries are developed for high-pressure gas atomization. These geometries can be divided into two categories as confined (close-coupled) atomizers and free fall atomizers, based on how the melt tube and gas nozzles are located (Fritshing & Uhlenwinkel, 2012; Motaman et al., 2015; Zeoli, Tabbara, & Gu, 2011).

Figure 3 shows a schematic of these two types. Gas flow in the close-coupled atomizer directly interacts with the melt exiting from the melt tube, and in free fall atomizer, the melt flows freely under gravity for some distance before the gas jet impinges. Close-coupled atomizer usually provides much finer powder compared to free fall atomizers (Zeoli et al., 2011). However, close-coupled atomizers often suffer from “lick back problem.” (J.T, 2013). Having reverse melt flow near the melt tube due to positive aspiration pressure and solidifying near the melt tube tip is called the “lick back problem” (Motaman, Mullis, Cochrane, McCarthy, & Borman, 2013).

However, this lick back problem is critical only at the beginning of the operation, where the nozzle tip is not appropriately heated. Free-fall atomizers are less problematic than close-coupled atomizers as the melt tube exit, and the gas nozzles are well separated.

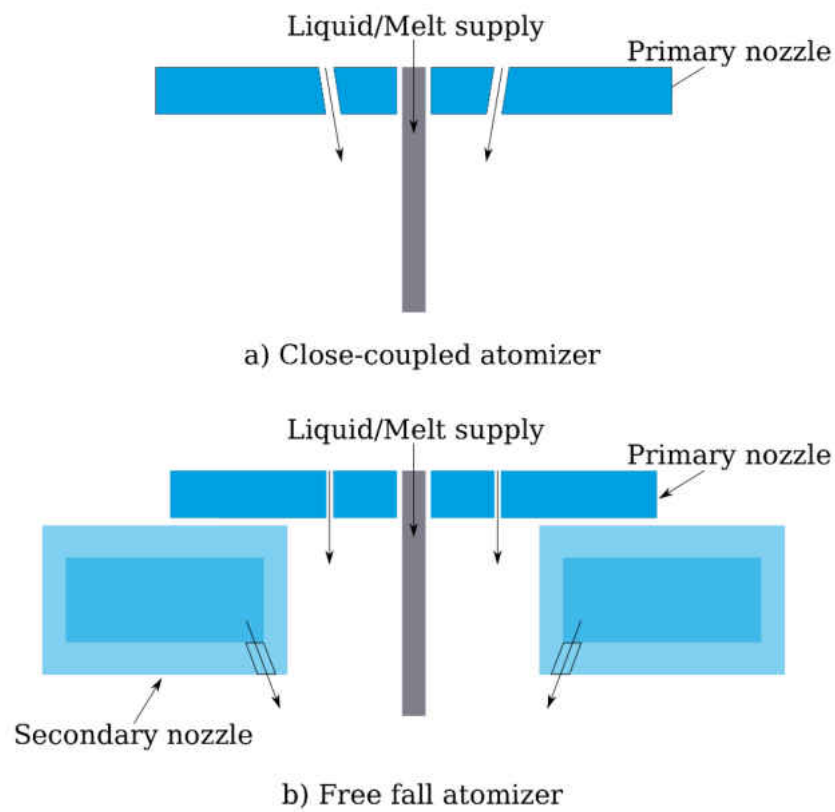


Figure 3 – Basic atomizer geometries, a. Close-coupled atomizer b. Free-fall atomizer

As shown in Figure 3b, the secondary nozzle is contributed to the main disintegration process due to the shear force acting on the melt stream. Primary nozzles are used to create a co-flow to counteract the backflow resulting from the secondary nozzle flow (Fritshing & Uhlenwinkel, 2012). Primary and secondary gas pressures must be adjusted to obtain proper atomization. This complexity limits the

applicability of the free fall atomizer (Fritsching, 2004; Heck, Fritsching, & Bauckhage, 2000).

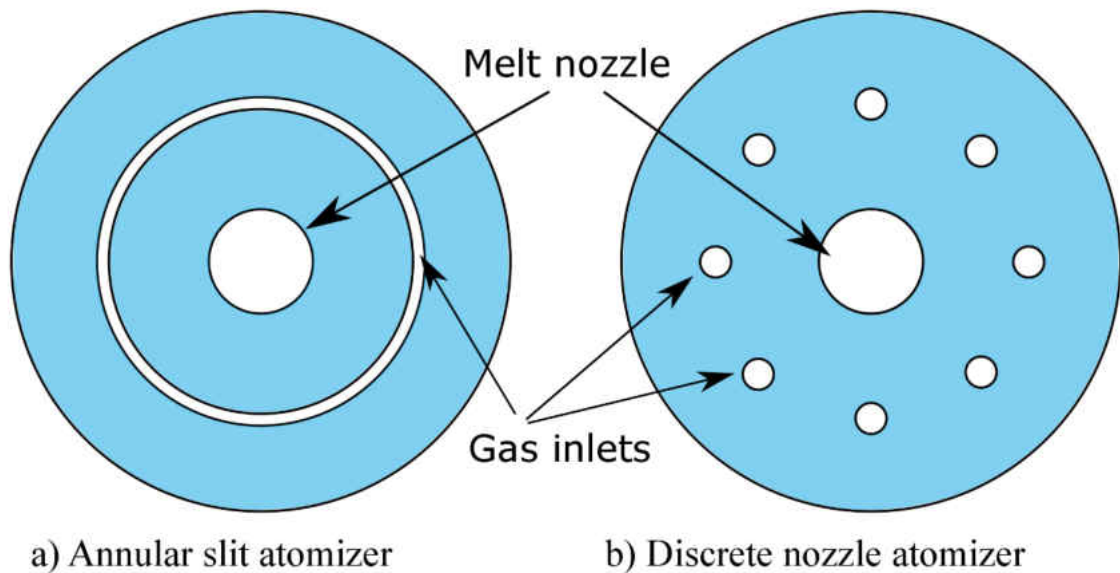


Figure 4 – Gas inlet types, a. Annular-slit gas nozzle, b. Discrete gas nozzles

The next subcategory of the gas atomizers is based on the geometry of the gas nozzle. They are annular-slit atomizers and discrete nozzle atomizers (Heck et al., 2000). As the name implies, annular-slit atomizers have a continuous gas slot around the melt tube, as shown in Figure 4a. Discrete gas nozzle atomizers (Figure 4b) consist of a set of individual nozzles around the melt tube. These nozzles could be a constant diameter, purely convergent or convergent-divergent nozzles (for supersonic flow) (Motaman et al., 2015). The constant diameter and purely convergent nozzles will create a choked flow, while convergent-divergent nozzles will permit controlled expansion with supersonic exit velocity. In a comparison of axisymmetric and non-axisymmetric nozzle geometries (Miller, Miller, Mourer, & Christensen, 1997), non-axisymmetric nozzle geometries are provided finer yield compared to axisymmetric

geometries. However, most of the numerical work is based on annular slit atomizers due to the simplicity of the geometry (Zeoli et al., 2011).

Experimental Studies

The first investigation on gas atomization for metal powder production conducted by S. Thompson in 1948 (Thompson, 1948). He used a close-coupled gas atomizer to study the effect of gas pressure, melt temperature, and melt flow rate on powder size distribution. Ayers and Anderson (Ayers, J.D., Anderson, 1985) studied the impact on stagnation pressure on powder sizes. They obtained the best yield when the static pressure at the melt inlet is minimized. Unal (Unal, 1987) studied the atomization process of an aluminum alloy for different atomizing gases. He used helium, nitrogen, and argon as the atomizing gas and studied various combinations of stagnation pressures, gas to melt flow rate ratios, and melt superheat temperatures. He observed a slight variation in powder size distribution when the melt temperature is increased above 1100 K (for Al alloy). This is due to the temperature dependence of melt viscosity and surface tension. Helium provided the finest powder distribution, and the powder sizes increased with increasing gas density (argon provided the coarsest powder distribution). He correlated the mean diameter of the powder distribution to be directly proportional to the square root of the melt flow rate. In a subsequent study, Unal (Ünal, 1989) utilized Schlieren images to study the supersonic flow characteristics in gas-only flow in a close-coupled gas atomizer. Miller et al. (Miller et al., 1997) studied the influence of axisymmetric and non-axisymmetric gas nozzle geometries and found that non-axisymmetric nozzles provide a better yield of finer powder. Strauss (J. T. Strauss, 1999) used preheated gas to increase the gas

momentum without raising the gas pressure and managed to reduce the mean diameter of the powder distribution. However, the lower limit of the diameter range remained unchanged irrespective of the gas temperature. Preheating the atomizing gas also reduces the operation cost as it lowers the gas consumption. In a subsequent study (J. Strauss, 2000), he introduced a new parameter, the normalized gas energy rate, which correlates well with the mean diameter at a wide range of operating conditions. The normalized gas energy rate is defined as the ratio between gas kinetic energy and melt mass flow rate.

Open and closed wake condition is another operating condition that has been studied extensively. Closed wake occurs, when a flow circulation region below the melt-tip is independent of the surrounding flow structures. It is due to a normal shock that appears around this flow region. This normal shock, also called Mach disk, is acting as a shield isolating it from the surrounding. Ting et al. (Ting, Peretti, & Eisen, 2002) studied this phenomenon to investigate its effect on powder yield. The wake-closure pressure was obtained for that specific atomizer geometry. Closed wake condition is found to be a favorable condition to get finer yield as the interaction between the Mach disk, and the melt stream creates pulsating characteristics in the melt stream.

Mates et al. (Mates, S.P., Ridder, S.D., Biancanello, 2000) studied four different gas nozzle geometries (three with discrete gas nozzles and one with annular-slit gas nozzle – all gas nozzles had a converging area) to obtain the relationship between geometry, supersonic jet length, and dynamic pressure. Long supersonic jets and large dynamic pressures are found to be favorable to improve the melt-gas interaction. A comprehensive overview of the close-coupled gas atomizer with

converging and converging and diverging gas nozzles was presented by Mates and Settles (Mates & Settles, 2005a, 2005b). Using microsecond exposure Schlieren images, it is found that the primary breakup occurs within three to four melt nozzle diameters (Motaman et al., 2015) and secondary breakup up to ten melt nozzle diameters (Mates & Settles, 2005a, 2005b) in the axial direction. The supersonic shock structures were immensely affected by the presence of melt interfaces.

Anderson et al. (Anderson et al., 2018) provided a summary of the research needs in processing feedstock metal powder for the development of additive manufacturing. The importance of the gas atomizer nozzles and spray chamber designs to improve the yield, while minimizing the satellite formation and powder porosity. As the optimum powder sizes for the most additive manufacturing process are limited to a very narrow diameter range, less than 20% of the total powder yield can be utilized as feedstock material.

Numerical Investigations

Espina et al. (Espina, P.E., Ridder, S.D., Biancaniello, F.S., Mattingly, 1989) used the method of characteristics (MOC) to solve for the two-dimensional shock wave structures. MOC is a powerful compressible flow analysis approach, and it is capable of estimating the shock wave characteristics with the inviscid flow assumption.

With the development of the computational facilities and advancement of the computational fluid dynamics (CFD) techniques, computational fluid dynamic tools have been extensively utilized to study the high-pressure gas atomization process. CFD studies on high-pressure gas atomization can be divided into three categories

considering the numerical approach. The first category is the gas-only, single-phase simulations (Allimant, Planche, Bailly, Dembinski, & Coddet, 2009; Aydin & Unal, 2011; Mi, Figliola, & Anderson, 1997; Motaman et al., 2015; Tong & Browne, 2009). These CFD simulations were mainly utilized to study the effect of gas nozzle geometry, melt tube geometry, and atomizing gas properties on the shock wave characteristics. Piomelli (Piomelli, 1992) performed a gas-only CFD simulation to study the effect of stagnation pressure, turbulence, and taper angle on shock wave structures using different close-coupled atomizer designs. Figliola and Anderson (Figliola, R.S., Anderson, 1993) obtained velocity and pressure values from the gas-only simulations and introduced discrete Lagrangian particles to find the path of the individual particle in two-dimension axisymmetric computational geometry.

Mi et al. (Mi, J., Figliola, R.S., Anderson, 1996; Mi et al., 1997) conducted several gas-only simulations to study the effect of stagnation pressure, protrusion length, and the melt-tip geometrical conditions on the gas flow field using an annular, convergent-slit gas nozzle with a taper angle of 45° . Simulations were conducted in two-dimensional computational geometry and $k - \epsilon$ method used to model the turbulence. They found that the Mach disk moves axially downward with increasing stagnation pressure. They also found that the long protrusion lengths limit the filming mechanism, while the short protrusion lengths destabilize the process. Ting et al. (Ting, J, Anderson, 2004) conducted a CFD investigation to study the effect of gas pressure on the recirculation zone and the presence of secondary circulation zone below the Mach disk. Six gas pressures varying from 0.69 to 7.58 MPa were used for this particular study. Authors hypothesized that in the presence of melt in the atomizer, the Mach disk would disappear, creating pulsating behavior confirming the

previously reported observations (Lubanska H, 1970). They found that the aspiration pressure decreases with increasing operating pressure at open wake condition, and aspiration pressure increases with operating pressure at closed wake condition. Tong and Browne (Tong & Browne, 2009) compared annular-slit and discrete gas nozzles using compressible, gas-only CFD simulations and observed distinct characteristics of the gas flow structures near the melt-tip.

The second CFD simulation type is two-phase flow based on the Eulerian-Lagrangian approach. In the Eulerian-Lagrangian approach (E-L), gas (the continuous phase) flow is simulated using the Eulerian method and the discrete, melt flow is simulated using Lagrangian formulation. The coupling between the two phases are obtained by force and energy balance (if heat transfer is considered). The secondary breakup of the droplets is modeled using empirical and semi-empirical breakup models. The first simulation in the E-L approach was conducted by Kuntz and Payne (Kuntz, D.W., Payne, 1995). A two-dimensional computational mesh of a close-coupled gas atomizer was considered for the simulation. It should be noted that the melt and gas flow dynamics were decoupled (momentum and energy transfer is only limited to one direction from gas flow to melt droplets), and the obtained gas velocities were used to break up the melt droplets. Grant et al. (Grant, Cantor, & Katgerman, 1993b, 1993a) studied the inflight dynamics and thermal history of the melt droplets. It is found that droplet diameter, droplet distribution (other droplets), and the gas momentum transfer significantly affect the path of the individual droplet.

Hattel et al. (Hattel, Pryds, Thorborg, & Ottosen, 1999; Pryds, Hattel, & Thorborg, 1999) developed a mathematical model to study the inflight cooling and solidification of melt droplets by using the energy balance between continuous and

discrete phases. The inflight heat transfer models were divided into four categories as liquid cooling, undercooling, solidification, and solid cooling. Multiple droplets with different sizes were introduced at prespecified locations to initiate the Lagrangian particles. Breakup models were not included in this study. Three different atomizing gases were used and found that argon provides the best solidification rate. It was found that the bigger droplets move a much longer distance in the axial direction before it solidifies entirely. Also, the higher melt-gas ratios found to be pushing the solidification location further downstream.

Zeoli et al. (Zeoli & Gu, 2008b) proposed an isentropic plug nozzle to improve the melt-gas interaction. They reported that conventional annular-slit nozzles consume a significant amount of energy for the sudden expansion of the atomizing gas. In the proposed method, the gas expansion occurs isentropically; hence, the energy transferring to the melt phase can be improved. Significant improvement in gas dynamics and the powder yield was observed in the proposed isentropic plug design on the contrary to the conventional annular-slit design. In a subsequent study, Zeoli et al. (Zeoli & Gu, 2008a) combined the secondary breakup models and droplet cooling and solidification models to study different aspects of the atomization process. Undercooling, recalescence, peritectic, and segregated solidification models were included. The thermal history of the individual droplets was deeply correlated with the initial droplet diameter. Firmansyah et al. (Firmansyah et al., 2014) studied the two-way coupling between gas and droplet using E-L formulation. 1-5 μm diameter droplets were used to initiate the simulation, and their interaction with the supersonic flow structures was investigated. It is found that the presence of the melt in the gas flow changed the flow patterns significantly, resulting bimodal distribution in

mass size distribution. Thompson et al. (Thompson, Hassan, Rolland, Sienz, & LSN Diffusion Ltd, 2016) compared three breakup models (Kelvin Helmholtz model, Kelvin Helmholtz Rayleigh transport model, and Taylor analogy break-up (TAB) model) and found that Kelvin Helmholtz Rayleigh transport model is more suitable for the high-pressure gas atomization simulations. The simulations used an axisymmetric computational geometry, and discrete particle model with two-way coupling was utilized to study the breakup dynamics. Xinggang et al. (X Li, Sander, & Ellendt, 2013) implemented a complicated three-phase atomization approach, where the gas flow was modeled using Eulerian approach, and the metal and ceramic powder were modeled using Lagrangian method. A mixture of high-pressure gases and ceramic powder was used to atomize the molten metal. Interaction between gas-melt and melt-ceramic powder were investigated in detail.

The third CFD type is two-phase, Eulerian-Eulerian (E-E) type simulations, where both phases are simulated using the Eulerian approach. More information on these types of methods will be discussed in the subsequent sections. Conducting E-E type simulations are computationally expensive and numerically complicated. However, it is essential to understand the physics behind the primary atomization as both thermal and hydrodynamic aspects of the droplet breakup are severely correlated with the initial droplet size, droplet distribution, and the initial droplet location. Unlike the Eulerian-Lagrangian method, Eulerian-Eulerian methods solve for the interface; hence, they are capable of capturing the physics-based breakup process without using any empirical or semi-empirical models. In E-L methods, the common practice is to initiate the simulation with a given droplet distribution. However, it is impossible to obtain a realistic initial droplet distribution without accurately modeling

the primary atomization process. Therefore, it is often initiated with a random distribution or constant diameter droplets near the melt-tip. Thus, the E-E techniques are superior to the E-L formulations.

Tong and Browne (Tong & Browne, 2008) conducted the first E-E simulation in high-pressure gas atomization for metal powder production; the Front-tracking method was utilized to differentiate two-phases. Both phases were assumed to be incompressible, and to simplify the computational complications; only a two-dimensional computational geometry was used. The importance of the melt-gas interaction towards the gas flow and the atomization process were discussed. In a subsequent study, Tong and Browne (Tong & Browne, 2009) studied the influence of aspiration pressure in the presence of molten metal. They added the physics of gas compressibility and studied its interaction with the weakly compressible melt phase. They reported the significance of using compressible gas flow by comparing the incompressible and compressible simulations.

Zeoli et al. (Zeoli et al., 2011) conducted a three-dimensional, Volume of Fluid (VOF) based CFD investigation to study the primary atomization process. Reynolds Stress Model was utilized to capture the turbulence effects. Three nozzle types (a conventional annular-slit nozzle, swirling gas atomizer, and an inner jet gas atomizer) were considered for this investigation. It was found that the inner jet gas atomizer provides the best powder yield among the other nozzles and swirling gas nozzle does not provide an additional improvement over the conventional annular-slit nozzle. In a subsequent study, Zeoli et al. (Zeoli, Tabbara, & Gu, 2012) conducted several simulations to obtain the melt dynamics. Three modes of melt characteristics

for different gas to melt flow rate ratios were identified. They referred these modes as nozzle filming, mixed filming, and pinch off and no-filming conditions.

Hernandez et al. (Hernandez, F; Riedemann, T; Tiarks, J; Kong, B; Regele, J.D; Ward, T; Anderson, 2019) used a 5-equation compressible flow model coupled with the VOF model to study the close-coupled gas atomizer. In their preliminary results, they compared their gas-only results with the existing literature and validated the compressible flow approach. Then, they conducted the E-E, two-phase flow simulations to study the jetting and filming of the melt stream. However, as they pointed out, the computational grid resolution used in their numerical investigation is not fine enough to capture the droplet size distribution.

Eulerian – Eulerian Numerical Methods for Interfacial Flows

This section describes the main Eulerian-Eulerian numerical simulations that are being utilized to simulate interfacial flows.

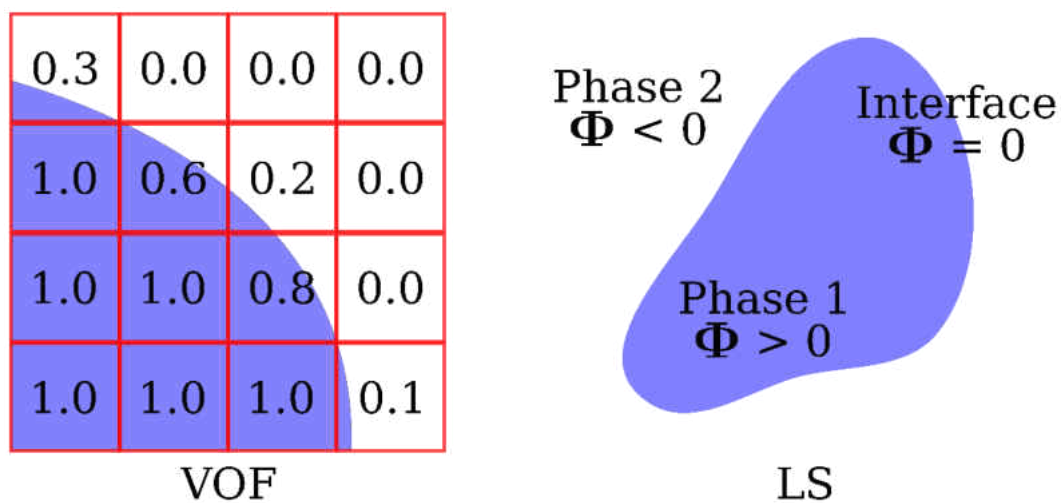


Figure 5 – Volume of Fluid (VOF) and Level Set (LS) approaches

Figure 5 shows a schematic of the VOF approach (Hirt & Nichols, 1981), and LS (Osher & Sethian, 1988; Sussman, 1994) approaches. In the VOF method, the volume fraction is utilized to obtain the amount of liquid (discrete phase) in each computational node. The volume fraction is defined as the ratio between the liquid volume and the cell volume. Therefore, the volume fraction has values within 0 and 1; one represents the liquid phase, and the zero represents the gas phase. The intermediate values represent the interfacial cells. The thermophysical properties are defined based on the volume fraction and have jump conditions at the interface. The main drawback of this method is the representation of the interface. More information on this method will be provided in the next chapter.

In the Level-set method, the interface is captured using the signed distance function. As the name implies, the distance function represents the shortest, normal distance to the interface (Figure 5). The value becomes either positive or negative based on the phase it locates. The convention is to have positive values in the liquid phase and negative values in the gas phase. The value zero represents the interface location. Therefore, it provides a smooth interface, unlike in the VOF method. Thus, the surface tension implementation (applying jump conditions at the interface) in the LS method is more accurate. However, the VOF method has better mass conservation than the LS method.

To mitigate these drawbacks and enhance the advantages of each method, Bourlioux (Bourlioux, 1995) proposed a hybrid method with a coupling between VOF and LS methods. Different implementations are being proposed to improve these hybrid methods in terms of accuracy and computational requirement (Albadawi,

Donoghue, Robinson, Murray, & Delauré, 2013; Haghshenas, Wilson, & Kumar, 2017; Sussman & Puckett, 2000).

Numerical Challenges in Atomization Simulations

The main challenge in the atomization simulations is the high grid resolution required to capture both primary and secondary atomization process. Many studies have reported the presence of artificial or fake droplets when the grid resolution is not enough to capture the interfacial dynamics (Gorokhovski & Herrmann, 2008; Shinjo & Umemura, 2010). They reported that the error of having artificial droplets could only be minimized by increasing the grid resolution. However, it is not possible to eliminate it.

Several empirical criteria are reported in the literature to estimate the required grid density (Desjardins, Moureau, & Pitsch, 2008; Hasslberger, Ketterl, Klein, & Chakraborty, 2019). The often-utilized empirical criterion is to have at least ten grid points along the smallest length scale of the droplet or the ligament.

Shinjo and Umemura (Shinjo & Umemura, 2010) used a criterion that ensures the order of the local aerodynamic Weber number is in the order of $\mathcal{O}(1)$. This condition is adopted from the previously reported critical Weber number condition. This was first reported in 1931 by Weber (Weber, 1931). If a droplet or a ligament has a Weber number that is greater than the critical Weber number, this droplet or the ligament has the possibility of disintegrating into much smaller droplets. The value of the critical Weber number is about ten (Choudhury, 2015; Davanlou, Lee, Basu, & Kumar, 2015; Hanson, Domich, & Adams, 1963; Saha, Lee, Basu, & Kumar, 2012) however, the value is smaller for highly turbulent flows (Hinze, 1955). However, a

trial and error approach has to be followed as the local velocities cannot be accurately estimated beforehand. They investigated the effect of these artificial droplets and found that the breakup process is not altered due to the presence of artificial droplets; however, the speed of the instability growth is found to be slightly affected.

Hasslberger et al. (Hasslberger et al., 2019) utilized the Kolmogorov length scale (Davies & Batchelor, 1954) to calculate the grid spacing to investigate flow topologies in primary atomization. The Kolmogorov scale is the smallest dissipative length scale that has to be resolved for Direct Numerical Simulation. However, they have reported that this criterion is not sufficient for two-phase flow simulations due to the cascade nature of the atomization process. However, a universal approach to calculate the required grid resolution has not been found so far. Herrmann (Herrmann, 2011) and Ling et al. (Ling, Fuster, Zaleski, & Tryggvason, 2017) argued that it is not possible to obtain the grid independent solution for aspects like droplet size distribution.

CHAPTER 3 – NUMERICAL MODEL AND CASE SETUP

This chapter provides the governing equations for the immiscible two-phase (Eulerian-Eulerian) system to simulate the high-pressure gas atomization process. Assumptions used in these simulations will be explained, and finally, the numerical case setup will be described in detail. OpenFOAM software (H. G. Weller, Tabor, Jasak, & Fureby, 1998) is used to simulate the atomization process. OpenFOAM is a robust, finite volume method based opensource software that provides a user-modifiable platform to implement new solvers.

Assumptions and Simplifications in the Simulations

Ideally, the numerical simulations of the gas atomization process should be able to capture all the length scales in the atomization process. Additionally, they need to capture the shock wave structures, their interaction with the breakup process, and heat transfer and solidification of the droplets. Due to the rapid cooling process, thermophysical properties of melt and gas phases vary as a function of temperature. However, several assumptions had to be made to simplify the computational complexity in terms of numerical and computational power limitations.

The first factor is the computational geometry and grid resolution. Since the atomization process deals with many length scales (size of the atomizer is in meter scale, melt diameter is in millimeter scale, and the secondary atomized droplets are in micron or submicron length scale), it is computationally impossible to capture all these length scales. Therefore, the computational geometry is reduced to a cylindrical geometry with 100 mm in the axial direction and 25 mm in radial direction. (more information on the atomization geometry will be provided in the subsequent section).

Only a 90° wedge in the cylindrical geometry is utilized for the computational simulations to further reduce the computational power requirement while preserving the three-dimensional nature of the atomization process. As discussed in the previous Chapter, a universal criterion to estimate the required grid resolution for atomization simulations is not developed so far. According to the empirical relationship often utilized in literature, to numerically capture the breakup of a 100 μm droplet, it is required to have a grid with at least 10 μm . Similar grid resolution for the current computational geometry will result 50 – 100 billion computational nodes, which is not possible to handle using the current state of the art computational facilities. As the scope of the present investigation is to guide the powder manufacturing industries to optimize their atomization process, it is required to develop a practically feasible, but adequate grid resolution to capture key characteristics of the primary and secondary atomization process. Therefore, strategically placed additional grid refinements are imposed in the areas where melt-gas interactions occur.

Since the gas atomization process usually required higher gas pressures to atomize the high-density melt stream, it is inevitable to have supersonic flow structures inside the atomization chamber. Capturing these shock structures in single-phase CFD simulations required additional care on the stability conditions as well as careful consideration of differencing schemes. Shock waves create infinite gradients, and it is necessary to use ‘upwinding’ type interpolation and gradient schemes to capture it accurately.

Two-phase simulations create additional complications due to melt-gas interactions. In the gas atomization simulations, the melt-gas interface acts as a solid wall due to the high-density ratio (i.e., for aluminum and nitrogen, the density ratio is

around 2400). In the presence of multiple ligaments and droplets, capturing such reflection waves further complicates the numerical approach, even with ‘upwinding’ type differencing schemes. In literature, there are few two-phase flow CFD investigations (Tong & Browne, 2009; Zeoli et al., 2012) that discuss the shock wave structures. However, they utilized a relatively coarser grid resolution, hence the error of calculating gradients can be minimized. Further, due to the coarse grid resolution, only the central liquid core and few other droplets are captured. Therefore, the complications due to multiple reflection waves were also minimized. The present study assumes the gas flow to be incompressible, even though it is a crucial factor in the high-pressure gas atomization process. This simplification is made primarily as it is essential to have a higher grid resolution to capture the atomization process and to obtain the droplet size distributions. The numerical complications would be unavoidable due to the large melt-gas density ratio and the interaction of the supersonic structures with multiple melt-gas interfaces.

Since the effect of thermophysical properties of melt on the atomization process is investigated, constant thermophysical properties were considered for the simulations.

Governing Equations

Since VOF based numerical simulations provide a diffuse interface compared to the LS method, it is required to capture the interface location to impart accurate interfacial forces. OpenFOAM software provides two advection schemes to advect the volume fraction in VOF. These two methods are algebraic advection and the geometrical advection methods. In the algebraic approach, compression velocities are

used to reduce the smearing of the liquid-gas interface. The algebraic advection scheme implemented in OpenFOAM is using a special numerical scheme named MULES (Multidimensional Universal Limiter with Explicit Solution) developed by Weller (Henry G Weller, 2008). OpenFOAM allows using sub-iterations (Deshpande, Anumolu, & Trujillo, 2012; Jasak & Weller, 1995) in time to ensure the boundedness of the volume fraction while maintaining a relatively larger time step. In the geometrical method, interface is reconstructed based on the volume fraction at neighboring cells. The geometrical method implemented in OpenFOAM uses a newly proposed geometrical scheme, ‘isoAdvector’ (Roenby, Bredmose, & Jasak, 2016; Roenby, Larsen, Bredmose, & Jasak, 2017). The isoAdvector geometrical advection scheme is found to be providing a much sharper interface compared to the algebraic method while ensuring phase mass conservation. Since the gas atomization process results in higher momentum, using the algebraic method could result in extremely high interface smearing. Therefore, the geometrical approach is utilized in all the simulations presented in this study. The continuity equation implemented in the single-fluid approach is provided in Equation 1.

$$\frac{\partial \rho}{\partial t} + \nabla \cdot (\rho \vec{U}) = 0 \quad (1)$$

ρ denotes the single-fluid density and \vec{U} is the velocity vector. Equation 2 provides the momentum equation.

$$\frac{\partial(\rho \vec{U})}{\partial t} + \nabla \cdot (\rho \vec{U} \otimes \vec{U}) = -\nabla p + \nabla \cdot \mathbf{T} + \rho \vec{g} + \vec{F}_\sigma \quad (2)$$

p denotes the static pressure. \mathbf{T} is the stress tensor for a Newtonian fluid, and \vec{F}_σ is the surface tension force, which are provided in Equation 3 and 4, respectively.

$$\mathbf{T} = \mu \left(\nabla \vec{U} + (\nabla \vec{U}^T) \right) - \frac{2}{3} \mu (\nabla \cdot \vec{U}) \mathbf{I} \quad (3)$$

$$\vec{F}_\sigma = \sigma \kappa \vec{n} \delta \quad (4)$$

μ , σ , κ , \vec{n} , and δ being the one-fluid dynamic viscosity, interfacial surface tension coefficient, interfacial curvature, interfacial unit normal vector, and the Dirac delta function that provides the value of one at the interfacial nodes. As shown in Equation 4, the surface tension force is modeled as a volumetric force, which only provides non-zero values at the interfacial cells. This method is called the Continuum Surface Force method (CSF) and was introduced by Brackbill et al. (Brackbill, Kothe, & Zemach, 1992). Interfacial curvature and Dirac delta function are calculated as $-\nabla \cdot \vec{n}$ and $|\nabla n|$, respectively and the interfacial unit normal vector is calculated as $\frac{\nabla \alpha}{|\nabla \alpha|}$.

The single-fluid thermophysical properties (density and viscosity) are calculated using volume averaging, as shown in Equation 5 and 6.

$$\rho(\alpha) = \rho_l \alpha + \rho_g (1 - \alpha) \quad (5)$$

$$\mu(\alpha) = \mu_l \alpha + \mu_g (1 - \alpha) \quad (6)$$

Where subscripts l and g denote the liquid and gas phase properties, and α is the volume fraction. In addition to these equations, the VOF method required to solve for the volume fraction (α) to capture the interface. Equation 7 shows the volume fraction advection equation.

$$\frac{\partial \alpha}{\partial t} + \nabla \cdot (\alpha \vec{U}) = 0 \quad (7)$$

The pressure-velocity coupling is solved using the Pressure-Implicit Method for Pressure Linked Equations (PIMPLE) method. This method is a combination of PISO – Pressure Implicit with Splitting Operators (Issa, 1986) and SIMPLE – Semi-Implicit Methods for Pressure Linked Equations (Patankar, 1980) algorithms.

Turbulence Modeling

The breakup process is mainly governed by the shear stresses at the interface. Therefore, accurate evaluation of these shear stresses is crucial in atomization simulations. Due to the higher inertia in the melt stream, it poses higher resistance towards the atomizing gas. Therefore, the relative velocity between the melt and gas phases at the interface acting as a boundary layer at the melt-gas interface. Thus, it is required to have a fine computational grid to resolve the turbulent boundary layer. In general turbulence modeling, the boundary layer occurs near the wall, and it is advised to create additional mesh refinements near the wall to accurately capture the boundary layer effects. Since the melt interface continuously changes and goes

through many topological changes, it is not possible to have additional refinements without using an adaptive mesh.

In terms of the numerical simulations, there are three different approaches to include the turbulence into the flow solutions. They are Direct Numerical Simulation (DNS), Large Eddy Simulations (LES), and Reynolds Averaged Navier-Stokes equations (RANS). These methods are categorized based on the way they resolve different size eddies. The large eddies contain large amounts of energy, and they are highly dependent on the geometrical and flow parameters. These large eddies break into smaller eddies once its energy decay due to dissipation. Therefore, these smaller eddies contain less amount of energy compared to the larger eddies and often considered to be isotropic.

In the DNS method, it is required to solve for all the length and time scales without using any modeling. Therefore, it requires an extremely fine computational mesh and mainly utilized in low Reynolds number applications. However, in two-phase atomization simulations, the length scale reduces to the micrometer scale. Therefore, obtaining the length scales required for DNS is computationally impossible. In the RANS method, all the turbulence eddies are modeled without resolving their length scales. Additional equations are utilized to obtain the Reynolds stress terms, and they were included in the momentum equation as source terms. Since RANS methods use modeling instead of solving the eddies, it needs a relatively coarser grid resolution than other methods. However, RANS models are not capable of accurately capturing the geometrical and flow effects. LES can be identified as a compromise between the computational requirements and accuracy limitations in DNS and RANS methods, respectively. In LES, large eddies are resolved without

using any modeling, and the smaller eddies are modeled as they are independent of the flow and geometrical characteristics. Therefore, the LES models have higher accuracy than RANS models and less computational requirements than DNS.

Considering these factors, LES is utilized to capture turbulence effects in the atomization process. In this study, these small eddies are modeled using the one-equation eddy viscosity model (Farvardin & Dolatabadi, 2013; A. Yoshizawa, 1986; Akira Yoshizawa & Horiuti, 1985) and sub-grid scale stress tensor τ_{sgs} is approximated as

$$\tau_{sgs} \sim \frac{2}{3} k_{sgs} I - \nu_{sgs} [\nabla \vec{U} + (\nabla \vec{U})^T] \quad (8)$$

Where k_{sgs} subgrid-scale kinetic energy, and it is calculated using Equation 9.

$$k_{sgs} = \frac{1}{2} (\overline{UU} - \bar{U}\bar{U}) \quad (9)$$

The transport equation of the subgrid-scale kinetic energy is given in Equation 10.

$$\frac{\partial k_{sgs}}{\partial t} + \nabla \cdot (k_{sgs} \bar{U}) = \nabla \cdot [(\nu + \nu_{sgs}) \nabla k_{sgs}] - \epsilon - \nu_{sgs} \bar{S}^2 \quad (10)$$

Equation 11-13 complete the model. The smooth filtering coefficient Δ is taken as one.

$$\epsilon = \Delta C_\epsilon (k_{sgs})^{1.5} \quad (11)$$

$$v_{sgs} = \Delta C_k (k_{sgs})^{0.5} \quad (12)$$

$$\bar{S} = \frac{1}{2} [\nabla \bar{U} + (\nabla \bar{U})^T] \quad (13)$$

The coefficients C_ϵ and C_k are taken as 1.05 and 0.07, respectively.

Post-Processing of the Droplet Size Data

As mentioned earlier, the VOF method uses the volume fraction to discriminate the two phases in the computational grid. The values of 1 and 0 represent the two phases, and intermediate values provide the interface between two phases (Figure 5). Therefore, it is not straightforward to identify each droplet and to obtain the size, location, and velocities of those droplets. A post-processing utility is developed to identify these droplets.

Droplet Size Distribution Algorithm

Volume fraction (α) is utilized to determine the cells which consist of liquid. Due to the numerical diffusion, there can be second phase cells with small α values, usually in the order of 10^{-12} or smaller. Therefore, a threshold value (α_{th}) is utilized to remove these cells from the calculation (William, 2016), and the value used in this study is 0.1. Mesh cells having an indicator function at or above the threshold value are considered as the dispersed or liquid phase. OpenFOAM allocates a number to each cell in the computational geometry, and it can be used to obtain the attributes of

the computational mesh such as mesh volume, and other state variables. The rest of the algorithm is explained using a sample mesh, as shown in Figure 6.

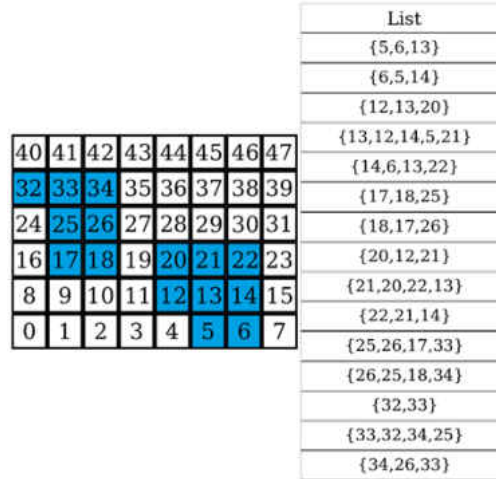


Figure 6 – Sample mesh with cell numbers. Blue color represents the cells that satisfy the condition ($\alpha \geq \alpha_{th}$)

In the example, there are 48 cells, and only 15 cells (colored in blue) are identified as the cells that satisfy the threshold condition ($\alpha \geq \alpha_{th}$). Then, by going through each liquid cell and identifying the neighboring cells (North, East, West, South, Front, and Back cells) that meet the threshold condition, a list can be generated, as shown in Figure 6. As an example, grid number 4, 6, and 13 are the neighboring cells of the cell number 5. However, only 6 and 13 cells satisfy the threshold condition; hence, the list entry of $\{5,6,13\}$ is generated.

These sets are then compared and append if they have common elements. This mechanism is implemented in Matlab. Let the generated list is defined as $L = \{l_0, l_1, l_2, \dots, l_n\}$ where, $l_i = \{p_0, p_1, p_2, \dots, p_m\}$.

```

for i = 1 to n + 1 do
  if L{i} ≠ {0} then
    for j = 1 to n + 1 do
      if i ≠ j then
        if (L{i} ∩ L{j}) = {0} then
          L{j} = L{i} ∪ L{j}
          L{i} = {0}
        end
      end
    end
  end
end
end
end

```

Figure 7 – Cell appending algorithm

This algorithm shown in Figure 7 will simplify the list, and each non-zero element will give all the cell IDs of a particular droplet. According to the example in Figure 6, the two non-zero elements of the list L are {5,6,12,13,14,20,21,22} and {17,18,25,26,32,33,34}. Then the centroid, volume, and velocities can be calculated using the summation over the cell numbers of each droplet, as shown in Equation 14-16.

$$\text{Droplet volume, } \mathcal{V}_i = \sum_{L_i} \mathcal{V}_j \alpha_j \quad (14)$$

$$\text{Droplet centroid, } (C_x, C_y, C_z) = \frac{\sum_{L_i} (x_j, y_j, z_j) \mathcal{V}_j \alpha_j}{\sum_{L_i} \mathcal{V}_j \alpha_j} \quad (15)$$

$$\text{Droplet Velocity } (U_i, V_i, W_i) = \frac{\sum_{L_i} (U_j, V_j, W_j) \mathcal{V}_j \alpha_j}{\sum_{L_i} \mathcal{V}_j \alpha_j} \quad (16)$$

Where \mathcal{X} , \mathcal{Y} , and \mathcal{Z} are the cell centroid values in three coordinates, \mathcal{V} is the cell volume and U , V , and W being the cell velocities in the three coordinates. Once the droplet volume is obtained, equivalent droplet diameter can be estimated by assuming a perfect sphere.

Even though the algorithm provided in Figure 7 is capable of distinguishing the cells corresponding to each droplet, handling several millions of sets can be time-consuming. To reduce the computational time, the total number of sets (n) are divided into a user-specified number of groups, and then the compared and appended within the group. Then the simplified sets in each group can be processed together to obtain the final distribution.

Symmetry Boundaries and Identifying Droplets that Leave the Computational Domain

As mentioned earlier in the assumptions, only a smaller portion of the atomizer geometry is considered to reduce the computational requirements. A 90° wedge of the cylindrical geometry is employed to further reduce the computations. Several complications in the droplet size distributions arise due to these assumptions. Identifying the droplets that share boundaries with the symmetry boundaries (to calculate the droplet volumes) and capturing the droplets that leave the computational domain are the main issues. Few modifications are included in the post-processing code to mitigate these errors.

The velocities and the volumes of the droplets that share boundaries with either one or both symmetry boundaries have to be adjusted. In the modified post-processing code, the droplets that share nodes with symmetry boundaries are identified and adjusted their volumes and velocities accordingly. As an example, the

volume of the droplets that are located in the axis of the wedge (which share nodes with both symmetry boundaries) should be multiplied by 4, and the volume of the droplets that are only on one symmetry boundary has to be multiplied by 2. The droplets that do not satisfy the above conditions are also identified, and their mirror images also considered when calculating the total number of droplets and total volume.

Identifying the droplets that leave the computational domain is problematic. It is possible to find the amount of liquid that passes through the outlet boundaries using surface integral of the liquid flux at the outlet boundaries. However, it only provides the volume. Identifying the size and number of droplets is not possible. Real-time calculation of droplet distribution will solve this issue. However, it will increase the computational time immensely. Therefore, a new post-processing method is proposed to approximate the droplets that leave the computational domain within a given period. As an example; let's take the droplet distribution at time t and approximate the droplets that leave the computational domain from time t to $t + dt$. Assuming the size and velocity of the droplets do not change within this time interval, the new location of all the droplets at $t + dt$ can be approximated as

$$\vec{C}_i(t + dt) = \vec{C}_i(t) + \vec{U}_i(t) \times dt \quad (17)$$

$\vec{C}_i(t)$ and $\vec{U}_i(t)$ denote the location and the velocity of the i^{th} droplet at time t . If $\vec{C}_i(t + dt)$ is not within the computational domain, the i^{th} droplet can be added to the droplet distribution at $t + dt$ as a droplet that left the computational domain. In this study, the time interval is taken as 0.2 ms.

Droplet Sphericity and Aspect Ratio

The atomization process evolves in the axial direction, and due to the surface tension force, ligaments and large droplets tend to deform and/or break up (secondary breakup) into spherical droplets. Therefore, sphericity of a droplet or a ligament can be used to understand the level of atomization of that droplet or ligament. In other words, the aspect ratio of the droplet can be used to understand the droplets that went through the secondary breakup process. Aspect ratio is defined as the ratio between the longest dimension of the droplet or ligament to the diameter of volume equivalent. A schematic of a ligament in two-dimensional mesh and the aspect ratio calculation procedure is shown in Figure 8. The span of the ligament (dx and dy) can be obtained by the centroid of the particular cell. Then, the longest dimension in 2-D can be calculated as $\sqrt{dx^2 + dy^2}$. It can be expanded for 3-D calculations by obtaining the z-directional span, dz. However, the aspect ratio calculation is an estimation as the exact location of the interface and centroid of the cell do not coincide with each other. Therefore, discriminating droplets solely based on the aspect ratio of unity is not accurate; hence, the secondary atomized droplets are identified by using an upper limit to the aspect ratio. In this study, the aspect ratio less than 2 droplets are identified as secondary atomized droplets.

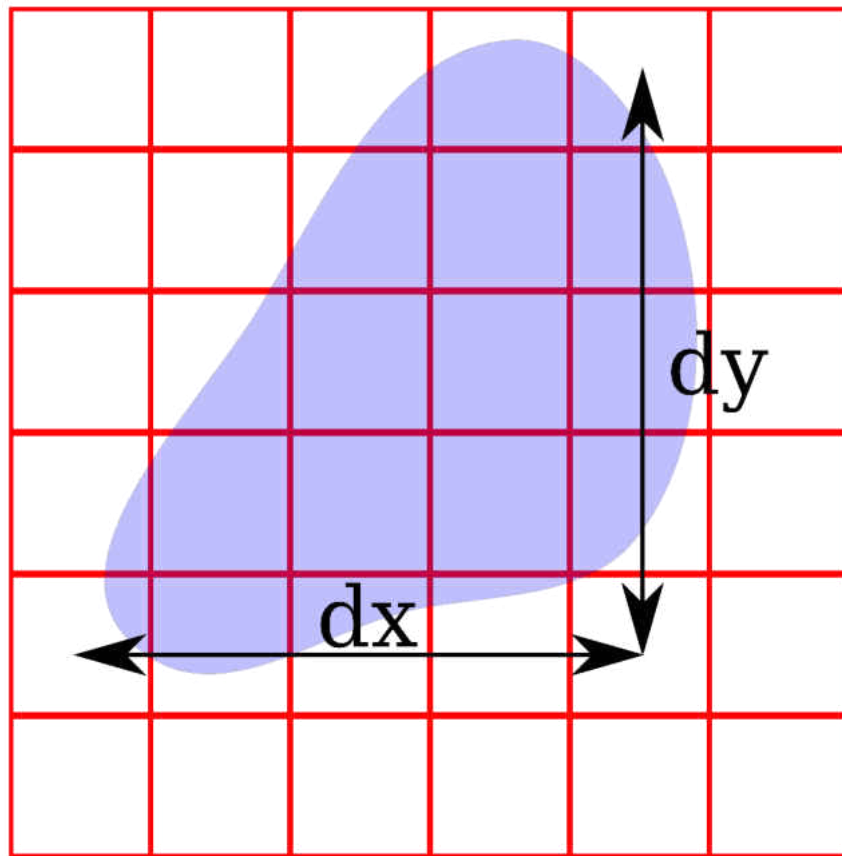


Figure 8 – Schematic of a 2-D ligament and aspect ratio calculations

Simulation Case Setup

The computational domain is designed based on a double induction, discrete nozzle, close-coupled gas atomizer, which consists of 18 circular gas nozzles evenly spaced around the melt tube. Figure 9 shows the atomization chamber and the gravity-driven molten metal. This atomizer is designed specifically for a batch process, and roughly around 2 kg of metal can be atomized in one batch. Initially, the metal blocks were placed in the double induction heater and heated it to the desired temperature. Then, the molten metal is poured into the atomization chamber, as shown in Figure 9b. It flows through the melt tube under gravity and interacts with the atomizing gas.



a.



b.

Figure 9 – a. Atomization chamber, b. Gravity-driven melt pouring into the atomization chamber.

Photo credit – Laboratory of Materials and Coatings for Extreme Environments, Advanced Materials Processing and Analysis Center at University of Central Florida

The simulation follows the experimental setup but uses an annular-slit gas nozzle instead of discrete circular gas nozzles. A schematic of the atomizer assembly, including the dimensions used in the simulation, is shown in Figure 10. The atomizer has a protrusion length of 3.6 mm, and the axial direction is 100 mm from the melt-tip.

Three structured meshes are considered in this study. Even though it is impossible to obtain grid independence in Eulerian-Eulerian atomization simulations (Gorokhovski & Herrmann, 2008; Ling et al., 2017; Shinjo & Umemura, 2010), a comparison is made to get an idea on the required grid resolution to achieve a feasible and sufficient accuracy. OpenFOAM inbuilt meshing utility, blockMesh, is utilized to

create these structured meshes. Strategically placed grid refinements are being used in the places where the atomization occurs. Grid statistics are provided in Table 1.

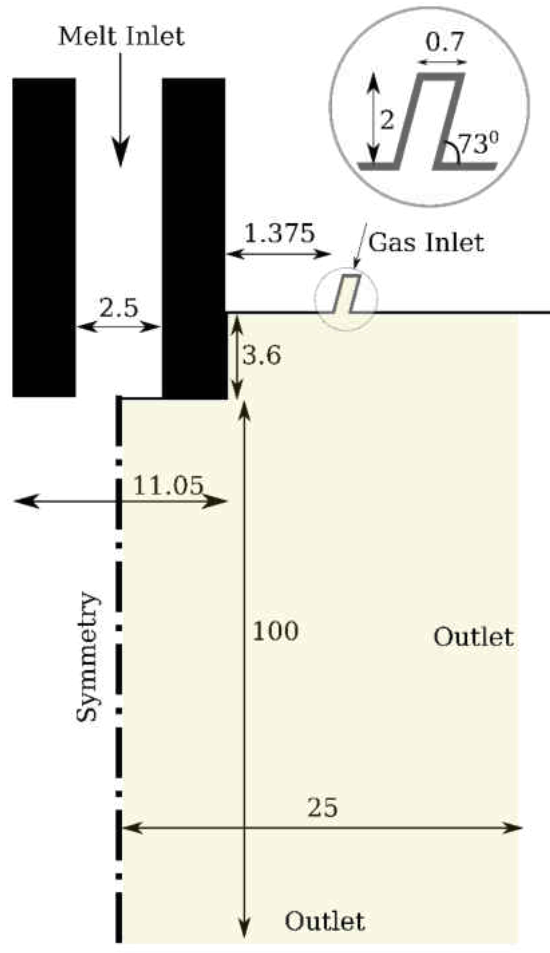


Figure 10 – Schematic of the atomization assembly. All the dimensions are in mm scale

Figure 11 shows the grid size distribution corresponding to the three meshes. It should be noted that only the mesh 2 and 3 are prepared with grid refinements. That is the reason for the sudden increment in the non-orthogonality from mesh 1 to 2 and 3.

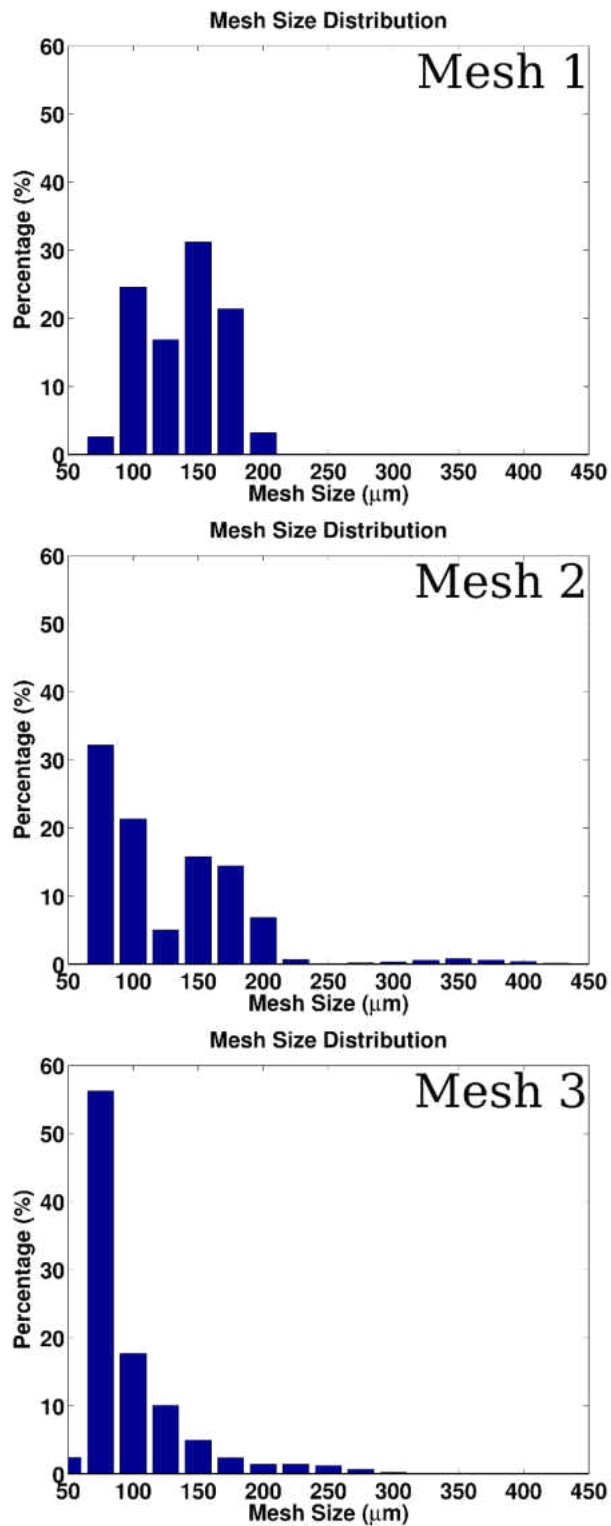


Figure 11 – Grid size distribution of three computational grids

In the localized grid refinements, the structured cells are divided into 8 (divided into 2 in each direction) and cell adjacent to the refined cell consists of high non-orthogonality and skewness. As shown in Figure 11, the percentage of the grid sizes smaller than $100 \mu\text{m}$ has increased significantly by using additional refinements. In the first computational grid, less than 30% of the computational grids are lower than $100 \mu\text{m}$ and the value for second and third meshes are around 50% and 75%, respectively.

Table 1 – Grid Statistics

	<i>Mesh 1</i>	<i>Mesh 2</i>	<i>Mesh 3</i>
Number of grid points (in millions)	10.7	16.0	20.2
Max.Non-orthogonality	31.2	54.5	57
Max. grid aspect ratio	6.5	5.2	4.2
Max. Skewness	0.96	1.43	1.19

Figure 12a shows the computational geometry and the initial distribution of the volume fraction. The volume fraction is initiated as a cylindrical shape with a diameter equal to the melt inlet diameter. The length of the cylinder is taken as 20 mm, and the value is carefully selected to ensure that the gas impingement occurs within the initial melt distribution. If the length of the initial melt stream is shorter than the gas impingement point, a strong circulation occurs towards the melt-tip, and the melt stream will be pushed in the upward direction. Figure 12b shows the localized grid refinements in mesh number 3. In the first level of grid refinement, all the grid points are divided are into eight cells, and in the second level of refinement,

each cell is divided into two in the axial direction. In the second mesh, only the first level of refinement is utilized.

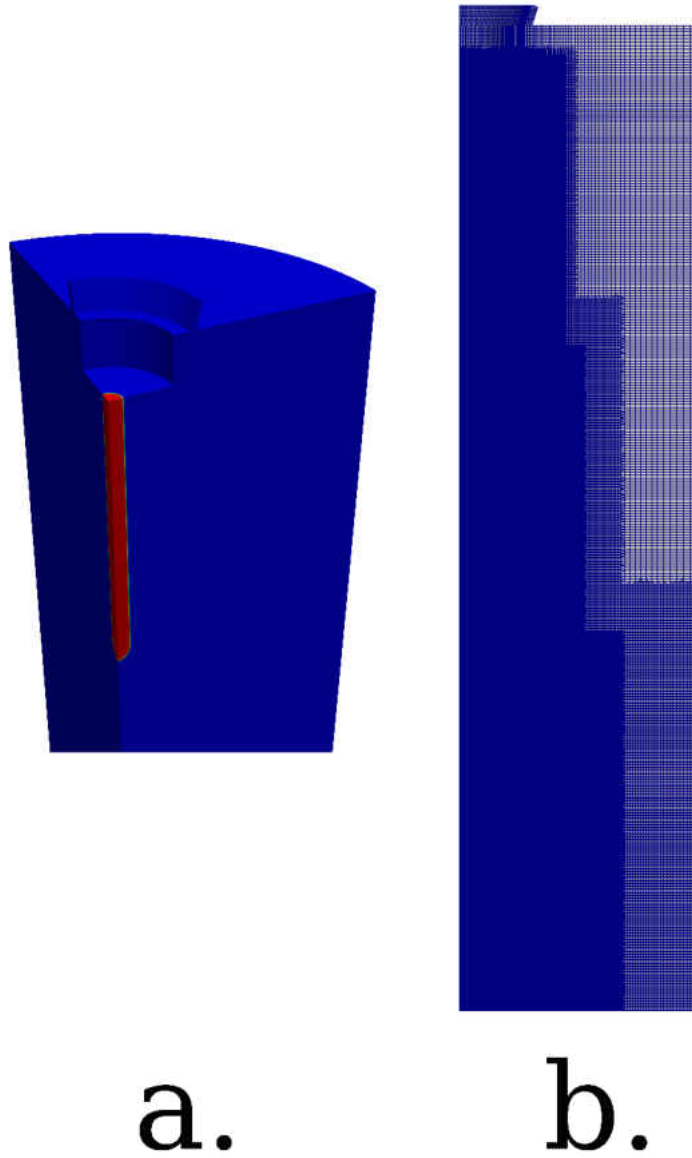


Figure 12 – a. Computational geometry and initial volume fraction distribution (red color – melt stream, blue color – gas stream) b. Localized grid refinements corresponding to mesh 3

Table 2 – Boundary Conditions

<i>Boundary</i>	Volume fraction	Pressure	Velocity	Turbulent kinetic energy
<i>Melt inlet</i>	Fixed value	Zero-gradient	Volume flow rate	Fixed turbulent intensity
<i>Gas inlet</i>	Fixed value	Total pressure	Pressure inlet	Fixed turbulent intensity
<i>Outlet</i>	Zero-gradient	Total pressure	Pressure outlet	Zero-gradient
<i>Walls</i>	Constant contact angle	Fixed-flux pressure	No-slip condition	Turbulent wall function
<i>Symmetry</i>	Symmetry	Symmetry	Symmetry	Symmetry

The boundary conditions used in the atomization simulations are shown in Table 2. The volumetric flow rate is specified at the melt inlet. As shown in Figure 9, the molten metal/alloy is poured into the atomization chamber, and it flows into the atomization chamber under gravity. Once the atomizing gas is introduced into the atomization chamber, the melt flow rate is governed by the gravitational forces and the pressure variation across the melt tube. Therefore, the melt flow rate changes with time. However, a fixed value is imposed at the melt inlet and the magnitude is obtained from the mean value from experiments. The total pressure is imposed at the gas inlet, and special care is given to the pressure and velocity conditions at the outlet to permit reverse flow. This boundary condition imposes zero Neumann condition if the boundary flux is pointed away from the computational domain. If the flux is pointed into the computational domain, a Dirichlet condition is imposed, and the value is obtained by the patch face normal component of the internal cell. Turbulent intensity of 2% and 5% is specified at the melt and gas inlets, respectively. This boundary condition calculates the turbulence kinetic energy based on the turbulence intensity and the induced velocity.

One of the main concerns in every transient CFD simulation is the stability conditions. Courant number is a non-dimensional number, which is often utilized as a stability condition in CFD simulations, and it is defined as follows.

$$Co = \frac{|\vec{u}|\Delta t}{\Delta x} \quad (18)$$

Where Δt and Δx are denoted by the time step and the local grid spacing, respectively. For explicit transient simulations, it is recommended to maintain the

Courant number below unity. However, the stability of the two-phase, Eulerian-Eulerian CFD simulations are more complicated than the usual transient CFD simulations, and it is required to limit the Courant number below 0.5. Further, it is essential to limit the progression of the interface to obtain a stable solution. Therefore, another non-dimensional number is defined as interfacial Courant number, which restricts the progress of the interface. The values used to limit the Courant, and the interfacial Courant numbers are 0.4 and 0.1, respectively. In other words, the progression of the interface within a given time step is limited to 10% of that local grid size. OpenFOAM allows providing the limiting values, and the time step is calculated based on the local velocity and the grid size. Since the high-pressure gas atomization process induces extremely high gas velocities, the time step of the numerical simulation is around one to ten nanoseconds. Therefore, the simulations are only conducted up to 2 ms (approximately around 0.2 to 2 million-time steps). The computational power required for the 1 MPa gas pressure simulation (mesh with 20.2 million cells) to reach 2 ms is around 84,000 processor-hours, which is equivalent to using 350 processors for ten days.

Computational Grid Comparison

As mentioned earlier, obtaining grid independence in two-phase, Eulerian-Eulerian numerical simulations, is not possible. However, a comparison of the three computational grids is provided here to find the influence of the grid resolution on droplet size distribution.

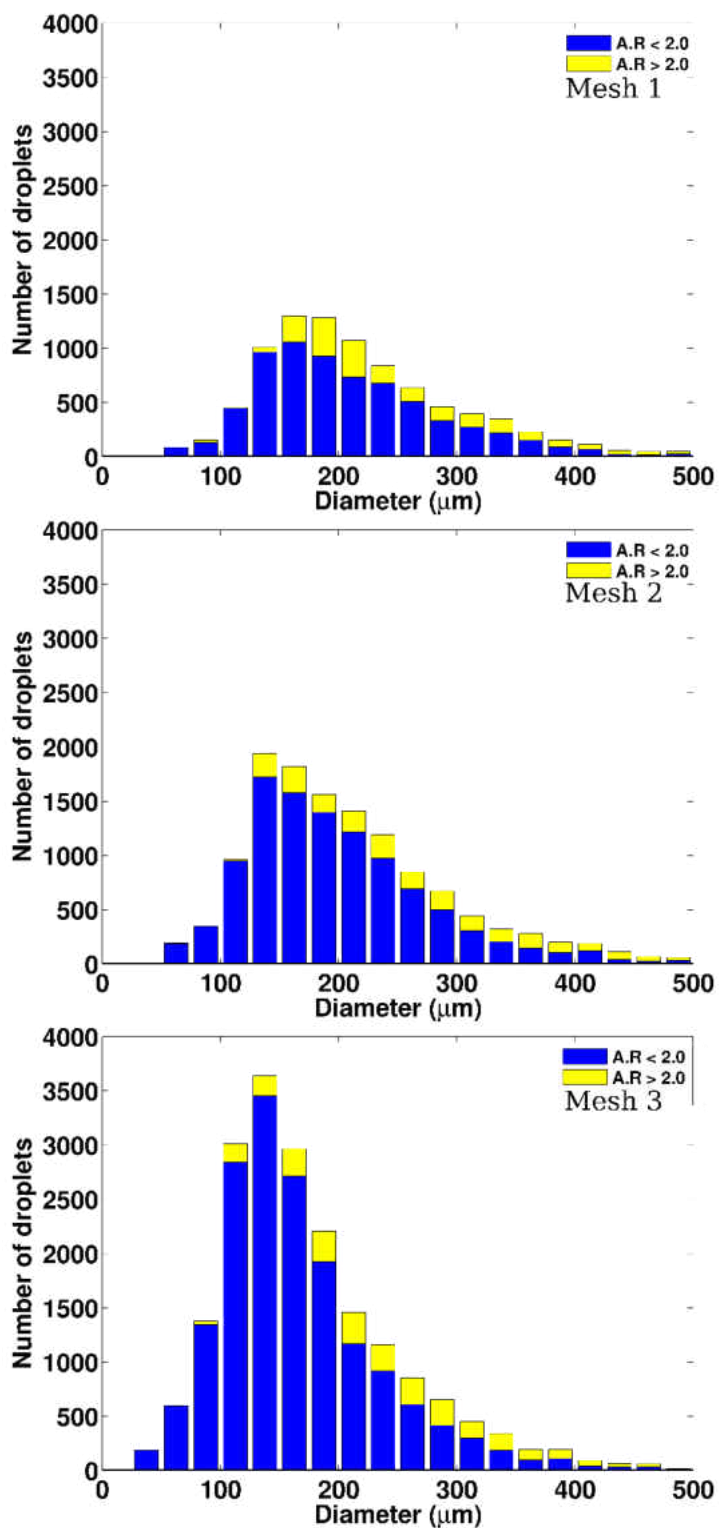


Figure 13 – Droplet size distribution at 2 ms – effect of grid resolution

Figure 13 shows the droplet size distribution histograms corresponding to the three grid resolutions at 2 ms. It should be noted that the droplets that are leaving the computational domain within the 2 ms time interval are accounted using the post-processing utility and added to make a proper comparison. More information will be provided in the next two chapters. It can be seen that the number of droplets increased drastically, with increasing grid resolution. As shown in Figure 11, the percentage of grid points that are smaller than $100\ \mu\text{m}$ is 30%, 50%, and 75% for the three meshes. This improvement in the grid density results in a significant increment in 100-200 μm diameter droplets. The mean diameter is reduced from 210.7 to 165.0 μm .

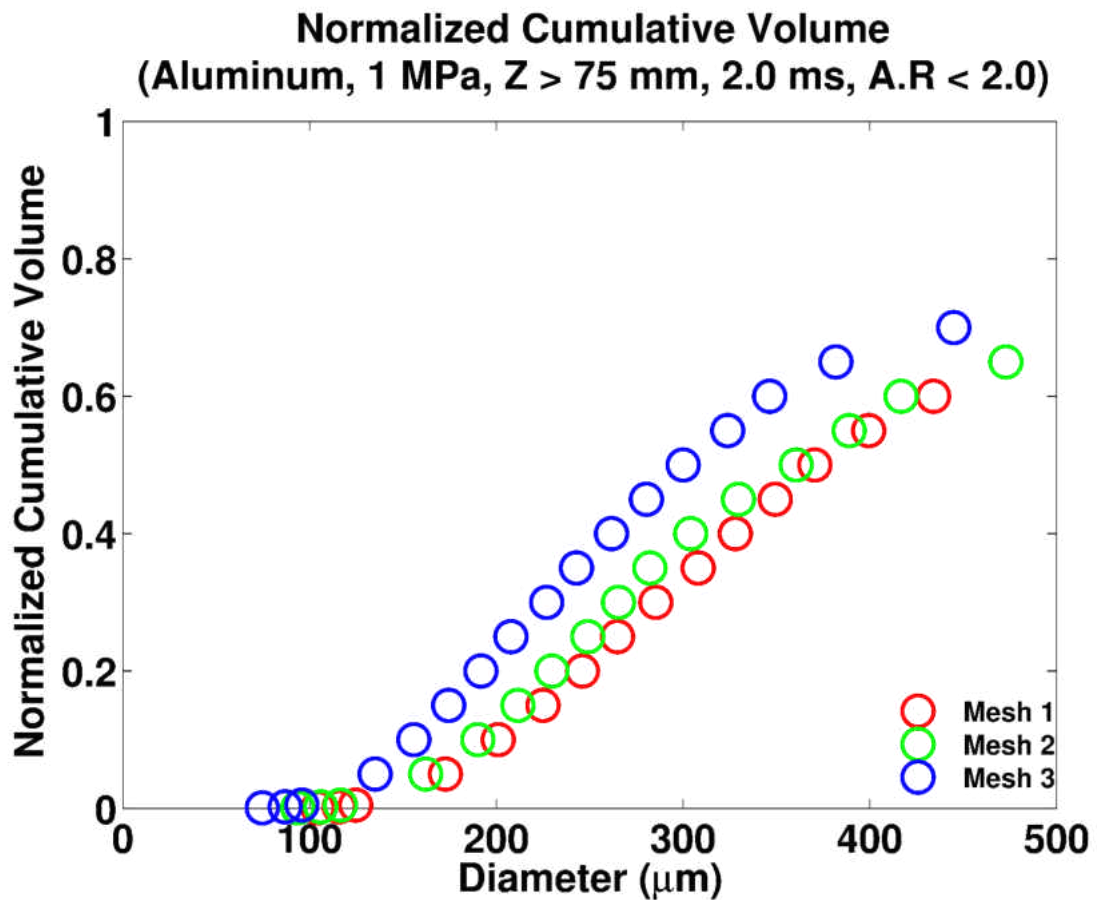


Figure 14 – Normalized cumulative volume – the effect of the grid resolution

Figure 14 shows the comparison of normalized cumulative volumes. It represents the droplets that satisfy the $AR < 2$ and $Z > 75$ mm conditions. $Z > 75$ mm condition consists of the droplets in the fourth quadrant (75 mm to 100 mm) and the droplets that have left the computational domain. These droplets are identified as the secondary atomized droplets. More information and the reasoning behind this droplet discrimination are provided in the next chapter. However, for the sake of completion, a comparison of cumulative volumes for the three meshes is presented here. Normalized cumulative volume is defined as a ratio between the cumulative volume and the total volume (including the droplets, which $AR > 2$). As an example, 20% of the total volume represents the droplets that are smaller than $200 \mu\text{m}$ (in mesh 3). In other words, it provides the yield of the atomization process. As expected, the 3rd mesh provides better yield compared to the 1st and 2nd computational grids. All three meshes show similar values until $100 \mu\text{m}$ and then deviate significantly.

Experimental Comparison

The results from aluminum atomization simulations at 1 MPa and 2 MPa gas pressures can be compared with the existing available experiments at different gas pressures in a close-coupled, discrete gas atomizer. Exact comparison is not possible since the experiments were done with 18 discrete circular nozzles. The current computations are done in an annular-slit to avoid excessively fine grid, which would be prohibitively expensive. The comparison plots are provided in Figure 15 as normalized cumulative volume in side by side plots.

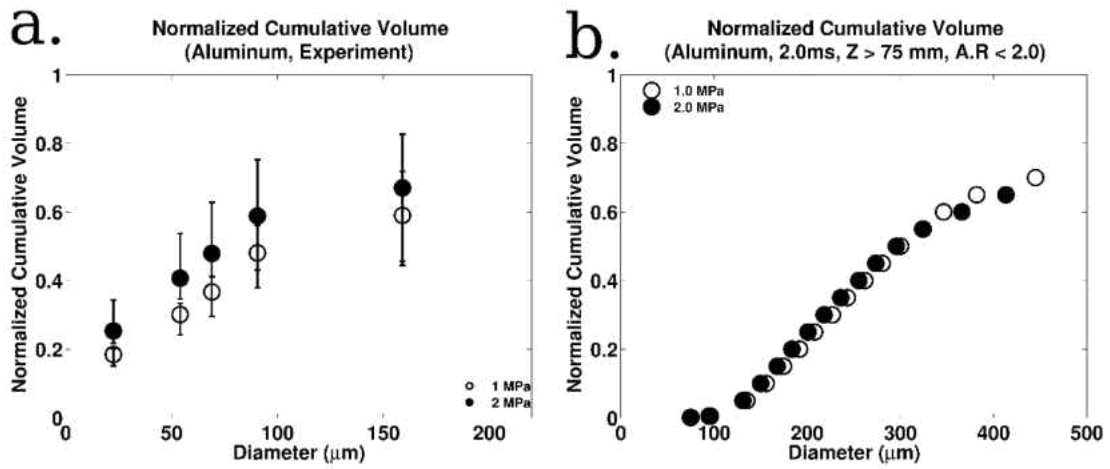


Figure 15 – Normalized cumulative volume, a. Experimental results (discrete gas atomizer), b. Simulation results (annular-slit gas atomizer)

The increasing gas pressure facilitates better atomization in terms of yield. The cumulative volume curve displays a steep slope with respect to droplet diameter. The numerical simulations in Figure 15b follow a similar trend with increasing gas pressure. However, a disparity in the droplet diameters can be observed. This is due to the current mesh resolution and the size of the computational geometry. As mentioned earlier, the computational geometry is 100 mm in length and 25 mm in radial direction. Therefore, droplets leaving the computational domain is inevitable. Even though these droplets are approximated and accounted in the calculations, the size of the droplet diameter remains the same once it leaves the computational domain. This is a crucial factor as the number of droplets leaving the computational domain is significant compared to the total number of droplets. As an example, in aluminum-nitrogen simulation (mesh 3, 1 MPa gas pressure), more than 17,000 droplets leave the computational domain within the 2.4 ms, and less than 7,000 droplets were inside the computational domain at 2.4 ms. More information will be provided in the next chapter. Further, the mesh resolution is not fine enough to capture the complete

atomization process. As mentioned earlier, the often-utilized condition to identify the required grid resolution is to have at least ten grid points along the diameter of a particular droplet. Therefore, to facilitate the breakup of a 100 μm droplet, the mesh resolution should be within 50-100 billion cells. It is impossible to run a practical engineering simulation with that capacity, even in the current state of the art computational facilities.

As the current grid resolution is capable of capturing the qualitative trends correctly (Figure 15), this grid is utilized for the rest of the simulations (i.e., the objective of the current research is to identify the trends in the powder size distribution and guide the powder manufacturing industries to make engineering decisions).

CHAPTER 4 – DYNAMICS OF ATOMIZING MOLTEN ALUMINUM

This chapter discusses the dynamics of the high-pressure gas atomization using aluminum as the molten metal and nitrogen as the atomizing gas. Table 3 shows the thermophysical properties of molten aluminum and nitrogen used in this investigation.

Table 3 – Thermophysical properties of aluminum melt and nitrogen

<i>Material</i>	Density $\left(\frac{kg}{m^3}\right)$	Kinematic viscosity $\left(\frac{m^2}{s}\right)$	Surface tension $\left(\frac{N}{m}\right)$
<i>Aluminum</i>	2400	1.23×10^{-6}	0.8
<i>Nitrogen</i>	1.205	15.11×10^{-6}	–

The melt flow rate is maintained at $7250 \text{ mm}^3/\text{s}$ and 1 MPa gas pressure at the gas inlet is used to atomize the molten aluminum.

Interfacial Instabilities in Atomization

In general, the atomization process is primarily governed by three interfacial instabilities. They are Rayleigh-Taylor instability, Rayleigh-Plateau instability, and Kelvin-Helmholtz instability. Kelvin-Helmholtz instability (Thomson, 1871) occurs when there is a relative velocity in the two phases. Due to the tangential component of the relative velocity, wave-like structures will appear on both sides. In other words, the discontinuity in the velocity at the interface induces a vortex sheet along the interface, which later rolls up the interface creating liquid layers. Rayleigh-Taylor

instability (Kull, 1991; Rayleigh, 1882; Taylor, 1950) occurs when there is a relative velocity perpendicular to the interface. As an example, when a high-density phase placed on a low-density phase, both phases try to penetrate the other to reach a stable state. These movements create the mushroom-like structures at the interface, which is considered as the main flow characteristic of the Rayleigh-Taylor instability. The size of these characteristic mushroom structures varies with the density ratio, and the shape is dominant when the lighter fluid penetrates the denser fluid. These two interfacial instabilities largely govern the primary atomization process. Rayleigh-Plateau instability occurs when the surface tension force adversely affects the surface curvature of a liquid interface (Eggers & Villermaux, 2008; Rayleigh, 1882, 1879). This instability can be observed in a liquid column flowing under gravity. When the liquid jet accelerates, the liquid column starts to stretch. It starts to deform to reduce the surface area while preserving the volume as the favorable condition is to minimize the surface energy.

Interfacial Dynamics

In this section, the time evolution of the melt stream is explained using the interfacial instabilities explained in the previous section. Figure 16 shows the time evolution of the melt interface (an isometric view). Yellow color contours denote the melt-gas interface (i.e., $\alpha = 0.5$), and the background color plots show the gas velocities at the two symmetry boundaries.

Following the standard practice, molten aluminum is allowed to flow for a few seconds prior to releasing nitrogen to prevent backflow. Initially, the melt stream starts to deform due to the high momentum expanding gas, resulting in interfacial

instabilities which break up the melt into ligaments and large droplets. This process is called the primary atomization. The large droplets and ligaments further break up into smaller droplets via Rayleigh-Plateau instability.

The white color circles are zoomed in and shown right below the corresponding time instant to emphasize additional details. Once atomizing gas is introduced to the atomizing chamber, the higher gas pressure induces extremely high gas velocities. The high momentum of the atomizing gas penetrates the melt stream near the point of impact. Low-density gas penetrating high-density melt is often identified as Rayleigh-Taylor instability. Additionally, further downstream (where the gases flow parallel to the melt stream), the relative velocities at the melt-gas interface result in wave-like structures as shown in Figure 16a. These wave-like structures further amplify with time (Figure 16b) creating melt sheets and ligaments (Figure 16c). This interfacial instability is often referred in literature as Kelvin-Helmholtz instability. Careful consideration of the zoomed-in views in Figures 16d and 16e shows how the ligaments form and break up. This breakup process is the main segment of secondary atomization and it was further discussed in the previous studies (Choudhury, 2015; Davanlou et al., 2015; Saha et al., 2012). The instabilities governing this process are Rayleigh-Plateau and capillary instabilities. A combination of these instabilities governs the dynamics of the secondary atomization.

The abovementioned gas penetration causes the melt stream to divide into two segments at the point of impact (Figure 16e). From this point onwards, the bottom disintegrated portion advects along the axial direction with the gas flow, while breaking up further into smaller droplets (Figures 16f and 16g) and staying as a cluster.

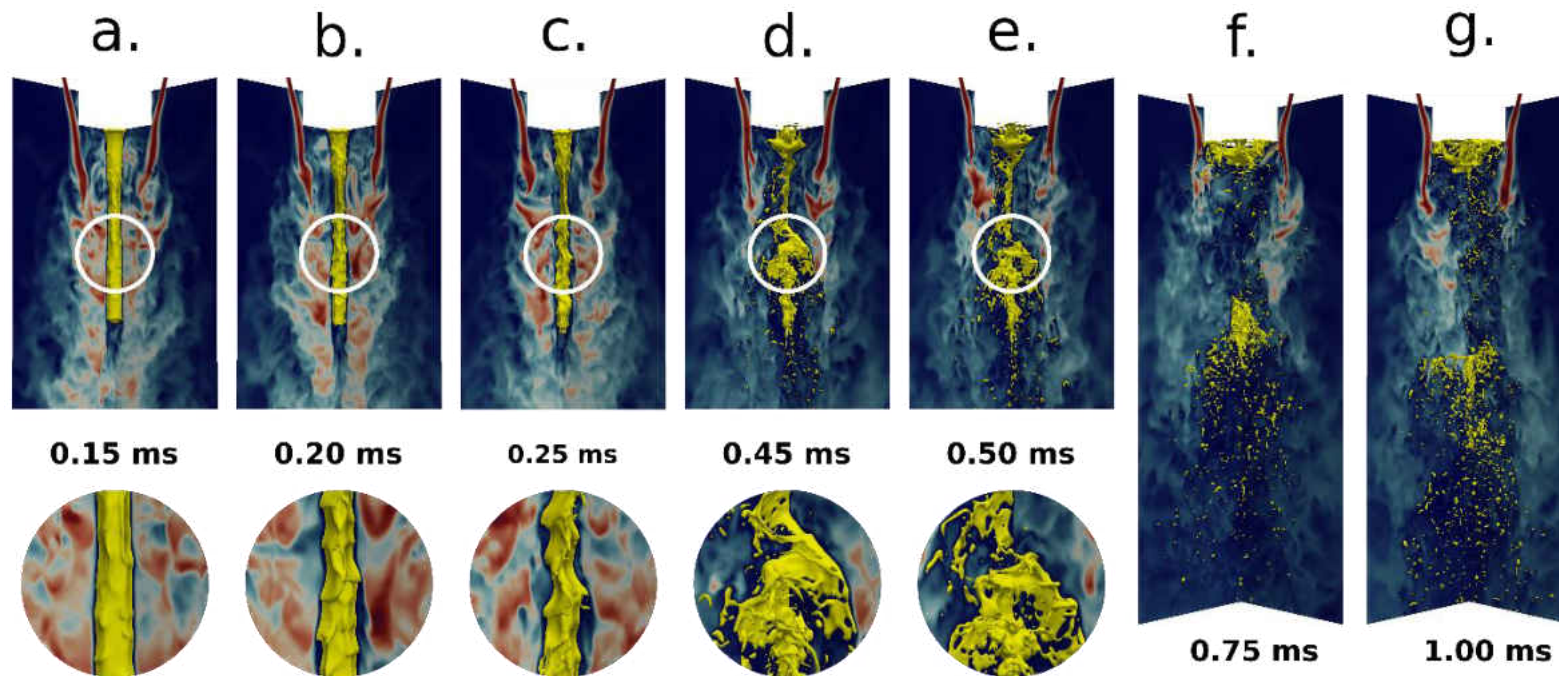


Figure 16 – Atomization physics – time evolution of the melt and atomizing gas interaction (Al-N, 1 MPa – mesh 3). Note – until 0.5 ms; images show only up to 30 mm from the melt-tip. 0.75 and 1 ms images show up to 50 mm from the melt-tip. The area enclosed in a white circle is zoomed in to emphasize the dynamics of the melt stream

Due to the variation of inertia of the individual droplet, the velocities of the cluster of droplets can be different. As time progresses, this cluster expands and spreads to a larger volume. This aspect is also observed in Figure 19, where the time evolution of the number of droplets along the axial direction is provided in the next subsection. The top portion of the melt moves upward towards the melt-tip due to the gas recirculation zone near the melt-tip. As a result of the gas recirculation, the melt accumulated near the melt-tip is experiencing a shear force in the radial direction along the melt-tip wall. Once the melt reaches the end of the horizontal wall, it interacts with the expanding gas and starts to breakup.

Figure 17 shows the breakup process of a small three-dimensional liquid structure. It shows the capability of the present grid resolution to capture secondary atomization to some extent. For clarity, this 3-D ligament circled at the top is divided into three ligaments as marked in red, blue, and black colors. The ligament marked in red, which was previously attached to the other two ligaments is separated around $510 \mu s$ (marked in yellow circle). At $550 \mu s$, this ligament is advected with the gas flow, displaying a neck that will be eventually pinched off into two segments. The ligaments marked in blue and black are extended along their axial direction due to Rayleigh-Plateau instability (Chandrasekhar & Gillis, 2009; Choudhury, 2015; Rayleigh, 1879) when the surface tension minimizes the ligaments into smaller packets with the smaller surface area for the same liquid volume. It can be seen that the liquid melt undergoes this instability first when the cylindrical volume thins, and the gas creates more perturbations on the surface. The liquid then collapses under the action of capillary forces due to surface tension and can be seen to break into smaller droplets.

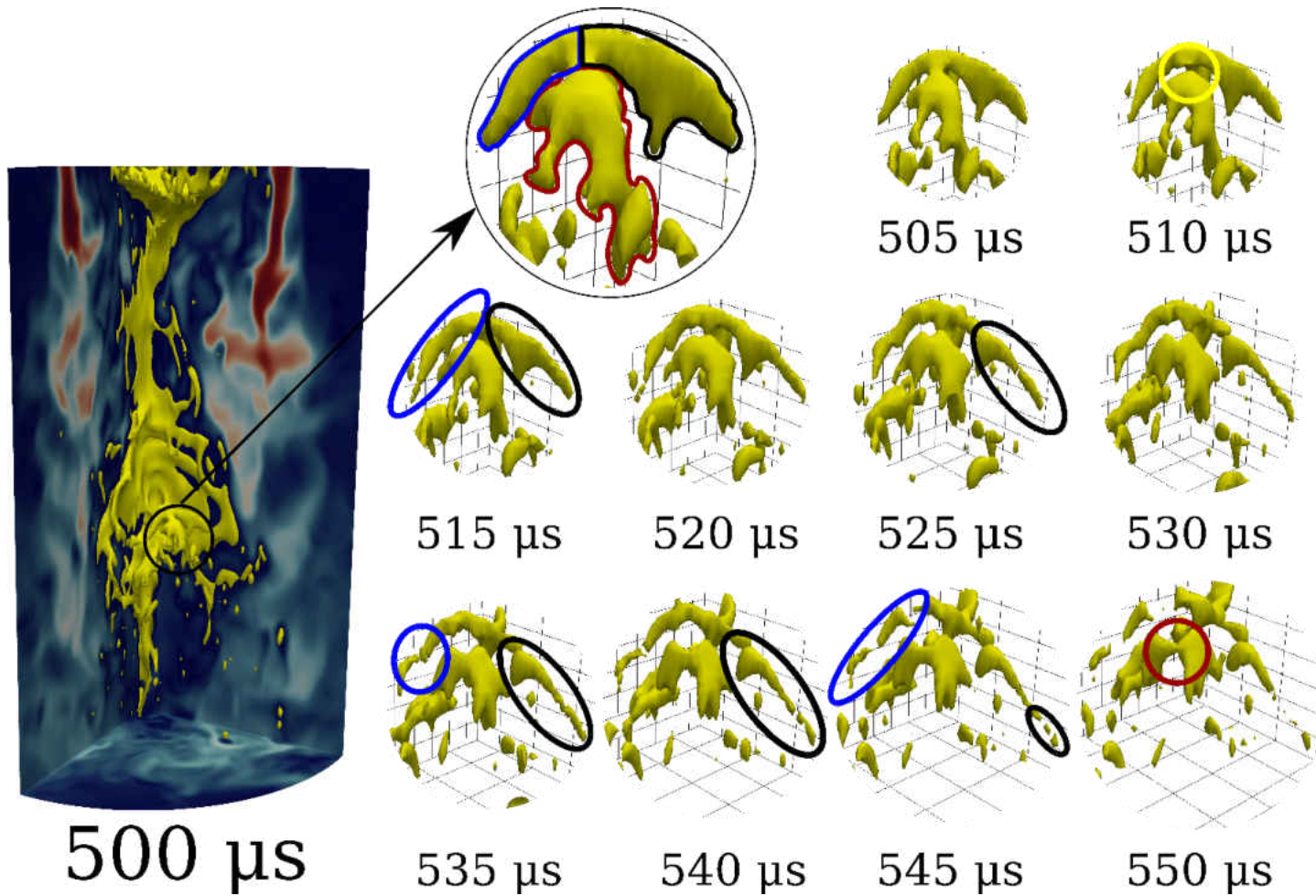


Figure 17 – Breakup mechanism of a 3-D melt structure at 1 MPa

These droplets and ligaments are circled in their respective colors to show the breakdown process in the subsequent time intervals. As previously mentioned in the literature, these ligaments are subjected to break into smaller droplets to reduce surface energy density. This instability plays a significant role in the secondary atomization process.

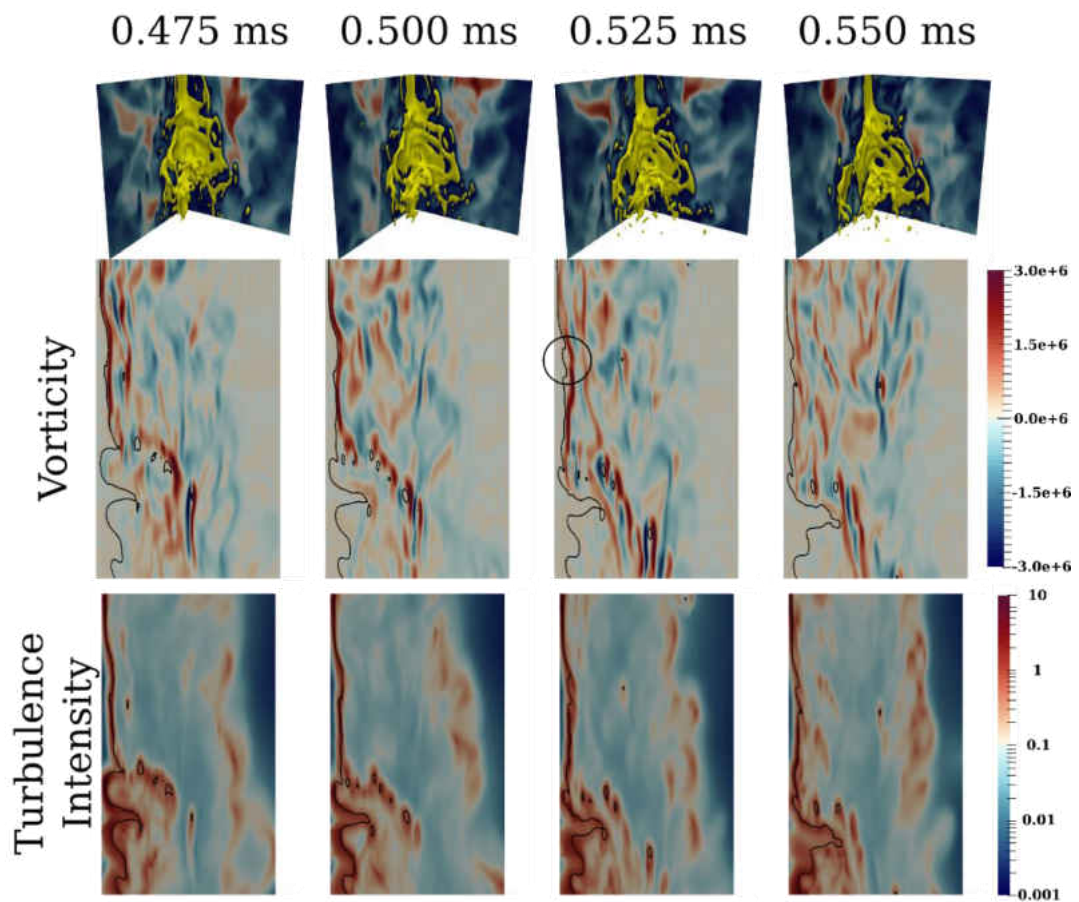


Figure 18 – Vorticity and turbulence intensity variation with the breakup. 2-D color plots represent the vorticity and turbulence intensity at the mid-plane (45° plane in 90° wedge)

In Figure 18, four images at incremental times, images of atomization, vorticity and turbulence intensity are displayed. The black contours indicate the melt-

gas interface. Note that the plane normal vorticity is shown. The positive vorticity values are pointed into the figure, and negative vorticity values are pointed in the opposite direction. The opposite directions in vorticity around the ligaments suggest that the flow structures induce torque, which leads to rupture. Thus, different types of instabilities contribute to secondary atomization. In the turbulence intensity plots (i.e., the log scale is used to properly visualize the variations), the turbulence intensity increases near the melt-gas interface. This is due to the chaotic interaction near the melt-gas interface, which creates perturbations and facilitates interfacial instabilities. The boundary layer developed near the melt-gas interface plays a major role in the breakup process since the shear forces exert on either side determine the deformation of the melt stream and the eventual breakup. The turbulence intensity plots indicate that the turbulence model and the current grid resolution can resolve these shear stresses even around the smaller droplets.

In Figure 18, the plane normal vorticity is displayed. It was primarily used as the positive and negative values of plane normal vorticity provides the direction of the rotational velocities in that two-dimensional plane. However, vorticity cannot be used to visualize the movements in the melt-gas interface in a three-dimensional representation. In literature, a parameter called Helicity ($\vec{U} \cdot (\nabla \times \vec{U})$) is utilized to represent the vorticity in the direction parallel to the flow velocity. By adopting a similar approach, a new scalar (interfacial normal vorticity, ω_{\perp}) is introduced to visualize the vorticity effects in a three-dimensional representation. The definition (Equation 19) is analogous to the Helicity equation; however, it takes the directional derivative in the direction of the interfacial normal instead of the flow velocity. The interfacial normal is calculated using the volume fraction, and the gradient of the

volume fraction provides the inward-pointing interfacial normal. The value is normalized by the product of the magnitude of the two vectors to obtain values between -1 to 1.

$$\omega_{\perp} = \frac{\nabla\alpha \cdot (\nabla \times \vec{U})}{|\nabla\alpha| |\nabla \times \vec{U}|} \quad (19)$$

Therefore, the positive values show the vorticity pointed into the interface, and the negative values show the opposite direction. They represent the clockwise and anticlockwise movements, respectively, in the plane tangential to the melt-gas interface.

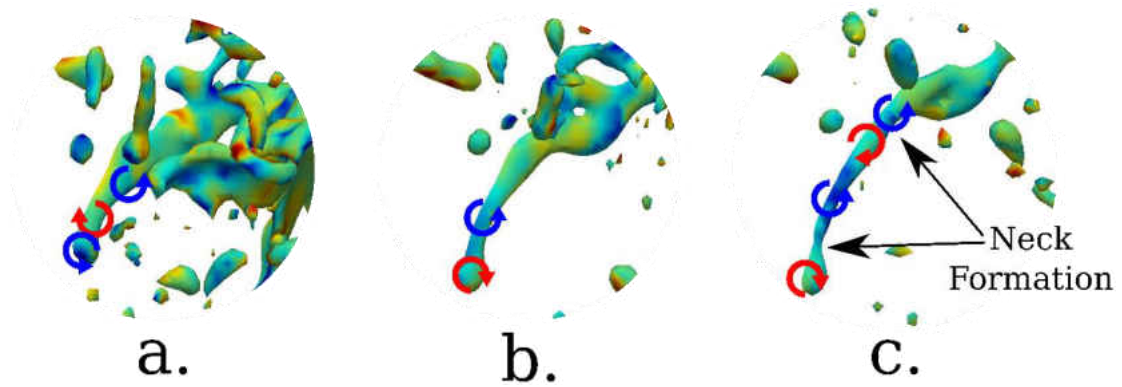


Figure 19 – Secondary atomization process – ligament breakup (color scheme – interface normal vorticity, red and yellow – positive values and blue – negative values)

Figure 19 shows the breakup process of a randomly selected ligament. The melt-gas interface is represented by the volume fraction contours at the value of 0.5. The interface is colored using the interface normal vorticity, which is defined in Equation 19. The red and yellow colors indicate the positive values (vorticity pointed

into the melt phase) have a rotation in a clockwise direction, and the blue color indicates the negative values, which has a rotation in the anticlockwise direction. As shown in Figure 19, the identified ligament is stretching with time, creating the characteristics of Rayleigh-Plateau instability. The curved arrows indicate the direction of the local rotational velocities based on the interface normal vorticity. Figure 19a and 19b show that the direction of these rotational velocities stretches the ligament, creating a neck. This ligament further stretches with time and results in multiple neck formations as shown in Figure 19c. This breakup mechanism is primarily due to the Rayleigh-Plateau instability, and the flow characteristics are matched with the previously published atomization studies (Choudhury, 2015; Eggers & Villermaux, 2008; Guildenbecher, López-Rivera, & Sojka, 2009; Marmottant & Villermaux, 2004). In other words, this shows the universal nature of the secondary atomization process and the feasibility of using empirical or semi-empirical methods (Eulerian-Lagrangian type approaches) to capture the secondary atomization process in high-pressure gas atomization process.

Figure 20 shows a closer view of the primary atomization process, mainly the ligament formation mechanisms in the high-pressure gas atomization process. The images show the interfacial dynamics in the molten steel atomization process. Even though this chapter discusses the atomization process of the molten aluminum, results corresponding to the molten steel are utilized as its atomization process evolves at a much slower rate than aluminum (refer Chapter 5). As explained in Figure 16, surface waves due to the Kelvin-Helmholtz instability appear downstream, where the gas flows parallel to the melt-gas interface. As shown in Figure 20a and 20b (blue color dashed line), axisymmetric surface waves can be seen at the early stages of the

atomization process. However, with time, these surface waves show non-axisymmetric characteristics as a result of two main phenomena. The main factor affecting these azimuthal variations is the interaction of the gas stream with the melt stream and melt tube geometry. These interactions induce perturbations in the melt-gas interface, which later amplify into these azimuthal variations. Perturbations due to the inlet turbulence conditions at the melt and gas streams also contribute to these movements; however, their effects are negligible compared to the fluctuations in the gas flow due to the interaction with the melt tube. The other factor affecting these azimuthal variations is due to the symmetry conditions imposed at the computational geometry. When the above-mentioned perturbations reach a symmetry boundary, it imposes a zero Neumann condition, and it results in an artificial perturbation in the melt-gas interface. This error can be minimized by using a hybrid boundary condition, which identifies the perturbation waves in the melt-gas interface and permits the advection through the symmetry boundary while imposing standard symmetry conditions for other aspects.

The green color circle in Figure 20a shows another mechanism in the high-pressure gas atomization process. As the higher gas pressures induce extremely high gas momentum, these previously mentioned surface waves (extended surfaces) could be stretched and perforated. This mechanism is previously reported by Jarrahbashi and Sirignano (Jarrahbashi & Sirignano, 2014). The arrows in Figure 20a and 20b show the direction of these azimuthal movements. When these azimuthal movements intercept with each other, it generates ligaments as shown in Figure 20c in blue color. These ligaments look like fingers. This mechanism primarily creates the ligaments at

the early stages. Similar characteristics can be observed in the area circled in red in Figure 20c and 20d.

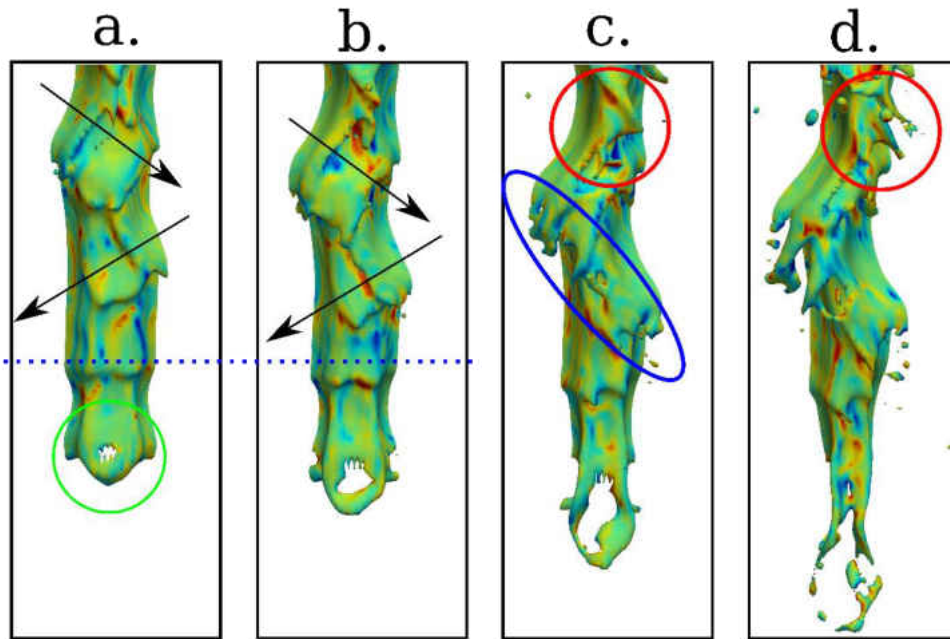


Figure 20 – Ligament formation (primary atomization process) – zoomed views show the interfacial dynamics (molten steel atomization) in the domain of 15 to 30 mm from the melt-tip in the axial direction. The used time frames are from 0.35 ms to 0.5 ms with 0.05 ms time intervals.

Processing of Droplet Size Distributions

This section provides the details on how the droplet size data are processed to obtain a deeper understanding of the atomization process. Figure 21 shows the time evolution of the number of droplets along the axial direction. The yellow patch in the histograms indicates the droplets with aspect ratio larger than 2 and blue color indicates the rest of the droplets. At 1 ms, most droplets are accumulated in the top quadrant between 20 – 30 mm from the melt-tip (the cluster of droplets in Figure 16g at 1 ms). With time, its peak moves downwards along the axial direction and several

droplets leave the computational domain as they undergo fragmentation. From 1 ms to 2 ms, the peak in the histogram moves from the first to the fourth quadrant of the computational domain. The total number of droplets with $AR > 2$ reduces from 17.2% to 13.3% due to secondary atomization when the ligaments break into smaller droplets with $AR < 2$. This phenomenon suggests that most of the secondary atomization has already taken place in 2 ms within 100 mm of the domain.

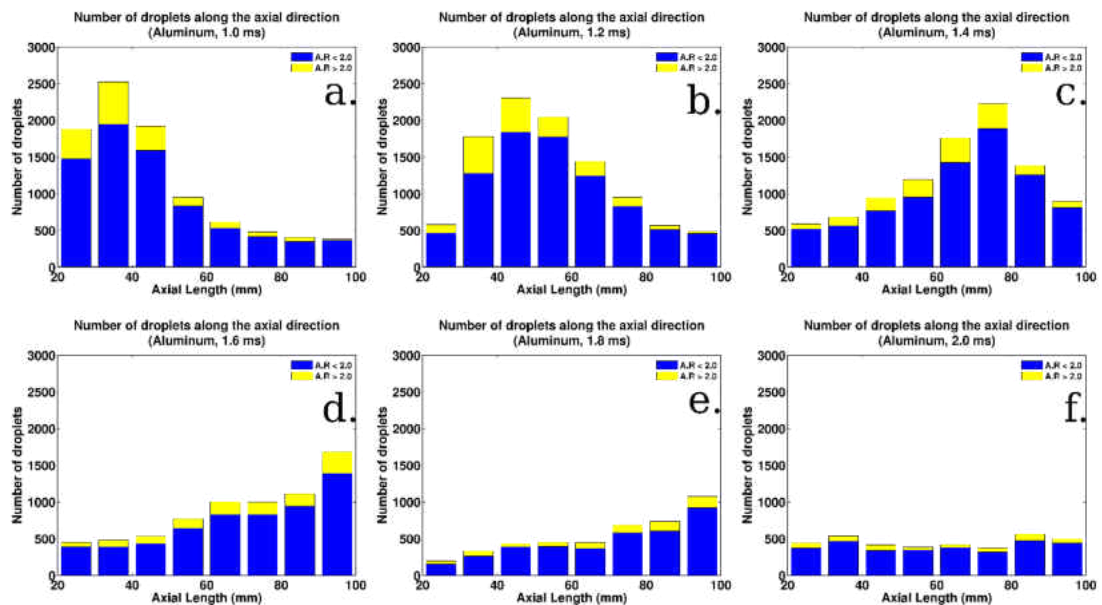


Figure 21 – Time evolution of the number of droplets along the axial direction (blue – droplet $AR \leq 2$, yellow – droplet $AR > 2$)

Both Figures 16 and 21 show the presence of droplets leaving the computational domain, and it is required to capture these droplets to make a proper comparison. As mentioned earlier, a post-processing utility is developed to capture these droplets. Figure 22 shows how the original distribution and how it changed after adding the droplets, which left the computational domain. In the original distribution, the number of droplets increases with time till 1.2 ms and then starts to decrease. As

shown in Figure 21, from 1.2 ms onwards, more droplets leave the computational domain, progressively. In the post-processing utility, the droplets (say at time t) which have the potential to leave the computational domain within 0.2 ms time interval (based on their velocities and location) are identified and appended to the next time step ($t + dt$, i.e., $dt = 0.2$ ms). The number of droplets leaving the domain increases from about 1500 to 17500 from 1 ms to 2.4 ms.

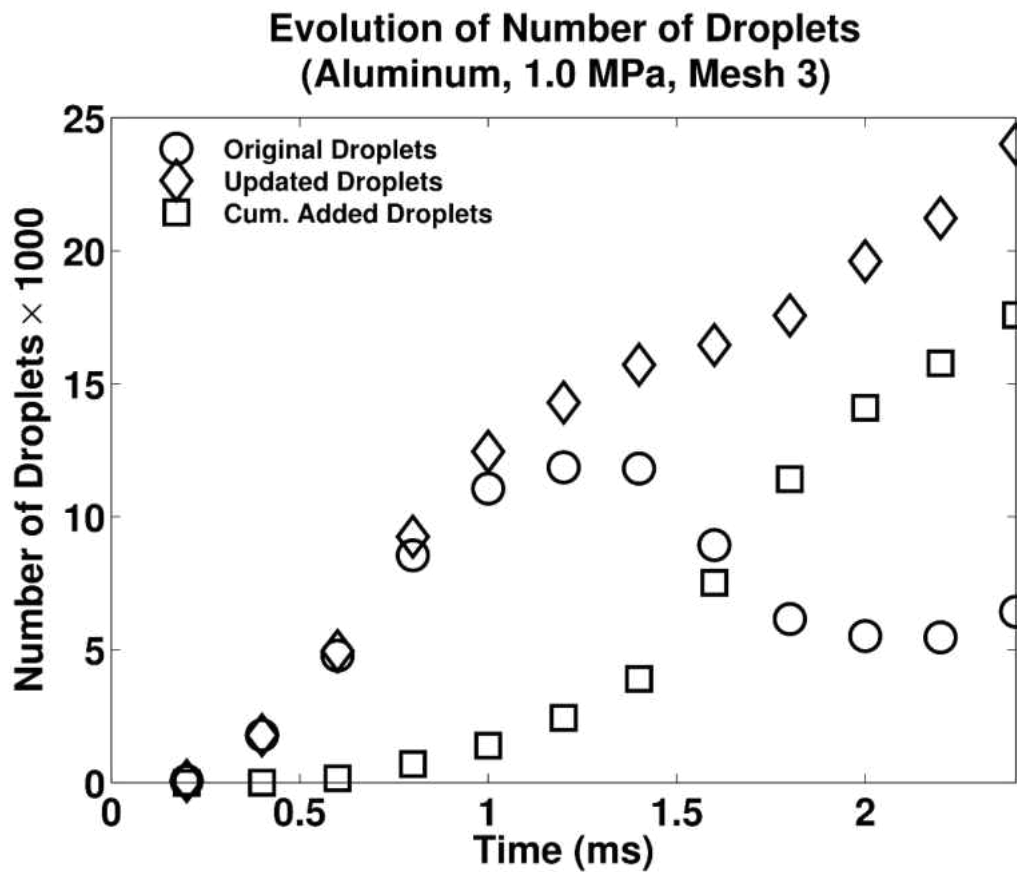


Figure 22 – Time evolution of the number of droplets – post-processing droplet size data

Figure 23a shows the time evolution in the number of droplets with spatial and aspect ratio based constrains. As mentioned earlier, the aspect ratio of the droplet is

utilized to understand the nature or the extent of the breakup process that droplet is being subjected to. As experimental results show the metal powder, which went through both primary and secondary atomization process as well as the solidification process, it is required to identify the droplets, which have gone through the secondary atomization process to make a fair comparison. However, characterization only based on aspect ratio is not adequate since there is a possibility of having large spherical droplets, which have not gone through the secondary atomization process. Therefore, another factor is identified to characterize the numerical results. Using a discrimination process with droplet $AR < 2$ and $Z > 75$ mm, only about 11% of the droplets at 2.4 ms are above $AR > 2$ (Figure 23a). Between 1.6 ms and 2.4 ms, the atomization process generates about 8100 new droplets in the $Z > 75$ mm, with the majority undergoing secondary atomization yielding a mean droplet size of $\sim 165 \mu\text{m}$.

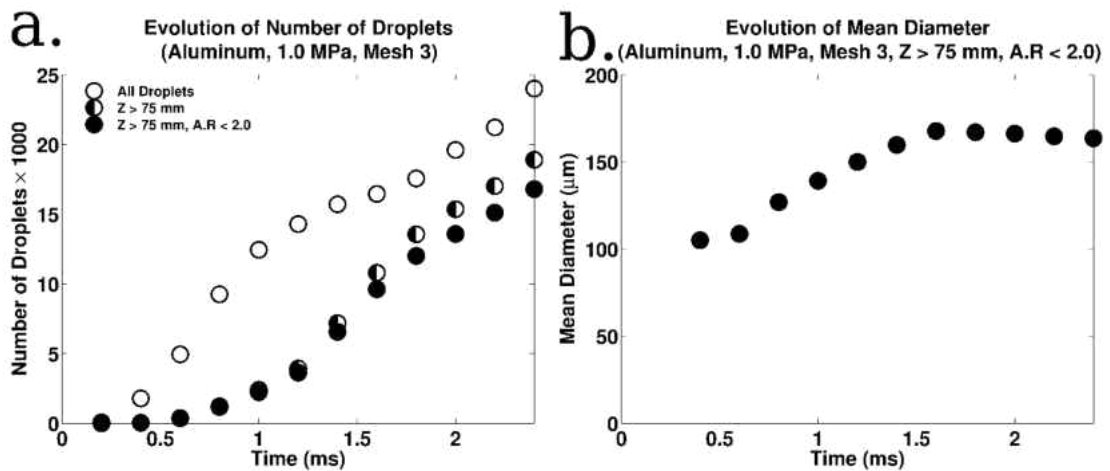


Figure 23 – Time evolution in the number of droplets, a) all the droplets compared to those at $Z > 75$ mm domain b) mean diameter variation ($Z > 75$ mm and $AR < 2$)

The mean diameter variation of the secondary atomized droplets is given for $AR < 2$ and $Z > 75$ mm in Figure 23b. The mean diameter increases monotonically up

to 1.6 ms before reaching a constant value. The $Z > 75$ mm domain consists of the droplets in the fourth quadrant and the droplets that have left the computational domain. As time progress, additional droplets reach the fourth quadrant as seen in Figure 21. As smaller diameter droplets have higher velocity, they reach the fourth quadrant earlier than the other droplets (as shown in Figure 16f). This allows the mean diameter to increase at the early stage. Figures 16 and 21 displayed melt disintegration with the droplets moving along the axial direction as a cluster, possibly atomizing further into smaller droplets. This cluster of droplets leaves the computational domain in the 1.6 ms – 1.8 ms time interval. The mean diameter of the droplets that leave the computational domain and remain in the fourth quadrant also show the peak mean diameter in this time interval. Henceforth, the mean diameters start to decrease slowly.

A characteristic time scale is introduced to understand the rate of the progression of the atomization process. Since the operational parameters (i.e., melt properties, gas properties, inlet gas properties, melt flow rate, etc..) considered in the current study vary the rate of progression, it is incredibly challenging to identify a characteristic time scale. Since the high-pressure gas atomization process primarily governed by the kinetic energy transferring from the expanding gas to the melt stream, the velocity scale is derived by equating the kinetic energy of the two phases. Then, the melt velocity becomes,

$$U_m \propto \left(\frac{\rho_g}{\rho_m} \right)^{0.5} U_g \quad (20)$$

Where, ρ is the density and subscripts m and g denote the melt and gas phases. as velocity is inversely proportional to the velocity, the characteristic time scale can be written as

$$\tau_c \propto \frac{1}{U_g} \left(\frac{\rho_m}{\rho_g} \right)^{0.5} \quad (21)$$

However, Equation 21 does not provide the effect of melt and gas flow rates. Therefore, an updated relationship is introduced in Equation 22. The validity of this equation will be discussed in detail in the Chapter 5.

$$\tau_c \propto \frac{1}{U_g} \left(\frac{\rho_m}{\rho_g} \right)^{0.5} \left(\frac{\dot{Q}_m}{\dot{Q}_g} \right)^{\frac{1}{3}} \quad (22)$$

\dot{Q} is the volumetric flow rate. As this characteristic time represents the rate of progression of the atomization process, the validity of the equation is checked for two different characteristics. The first one is the time taken to reach the peak in the original number of droplets distributions (τ_1), as shown in Figure 22. As explained earlier, it shows the balance between the number of droplets leaving the computational domain and the number of droplets generated. The second time scale is the time required to reach the peak in the mean diameter evolution (τ_2), as shown in Figure 23.

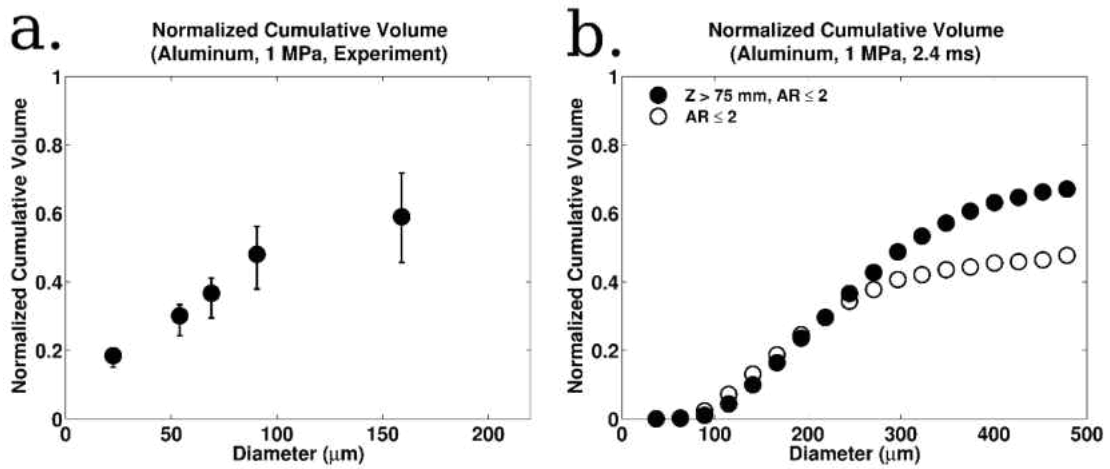


Figure 24 – Cumulative volume graphs, a. Experimental Results (Close-coupled, discrete gas atomizer), b. Simulation results – the effect of droplet discrimination (close-coupled, annular-slit gas atomizer)

Figure 24 shows the cumulative volume graphs with different constraints. The cumulative volume graph provides an estimation of the weight percentage corresponding to the desired diameter range. This is an essential factor deciding the effectiveness of the atomization process. It should be noted that the experimental results (Hanthanan Arachchilage et al., 2019) (Figure 24a) are obtained in a close-coupled, discrete-gas atomizer; hence, a direct comparison between experiments and numerical results cannot be made. Experimental results are presented merely to verify the capability of our numerical approach to capture the experimental trend. In the numerical results (Figure 24b), a comparison of cumulative volumes corresponding to two discrimination strategies are provided. It clearly shows that the best effectiveness is obtained when only the secondary atomized droplets are considered. The main difference between experimental results and numerical results is the diameter disparity. This is mainly due to grid resolution and the size of the computational geometry. As mentioned earlier, it is required to have an extremely fine computational mesh, and running such simulation is prohibitively expensive with the current

computational facilities. And the axial length used in the computational geometry is less than 5% of the actual atomizer geometry. Therefore, the present numerical simulation cannot capture all the length scales in the atomization process.

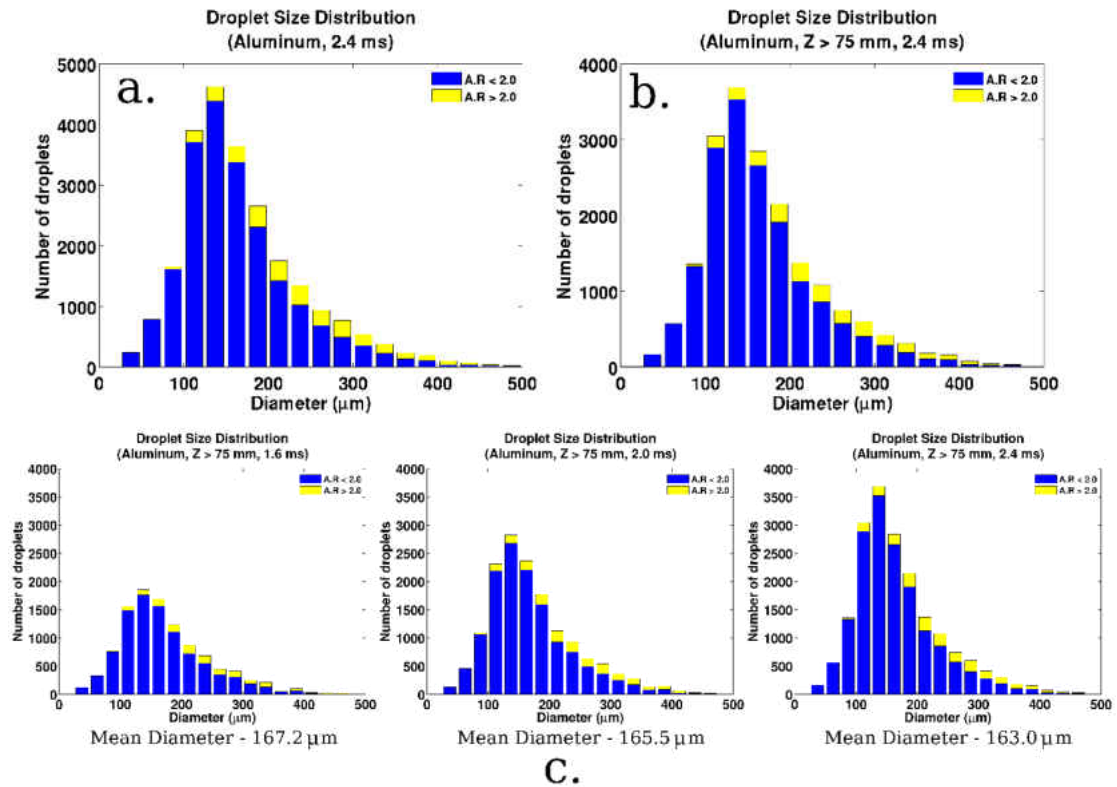


Figure 25 – Droplet size distributions, a. all droplets (2.4 ms), b. discriminated droplets (2.4 ms, $Z > 75$ mm), c. time evolution of the discriminated droplet size distributions

Figure 25 shows the droplet size distributions at different times and discriminations. Figure 25a represents all the droplets at 2.4 ms, and Figure 25b represents the discriminated droplets ($Z > 75$ mm) at 2.4 ms. Blue and yellow color bars indicate $A.R. \leq 2$ and $A.R. > 2$ conditions, respectively. The peak remains the same at 125 – 150 μm diameter range; however, the number of droplets is reduced considerably. Figure 25c shows the time evolution of the discriminated droplet size

distributions. The number of droplets keeps increasing, while the peak remains unchanged. However, the mean diameters are continuously getting smaller with time as expected.

CHAPTER 5 – EFFECT OF OPERATIONAL PARAMETERS ON THE ATOMIZATION PROCESS AND THE DROPLET SIZE DISTRIBUTION

This chapter discusses the effects of different operational parameters on the high-pressure gas atomization process, and the droplet size distributions. The operational parameters studied in this chapter are gas pressure, melt and atomizing gas thermophysical properties, and melt flow rate.

Table 4 – Simulation Matrix

<i>Case</i>	Mesh	Molten metal	Atomizing gas	Gas pressure	Melt flow rate $\frac{mm^3}{s}$
<i>1</i>	1	Aluminum	Nitrogen	1.0 MPa	7250
<i>2</i>	1	Aluminum	Nitrogen	1.5 MPa	7250
<i>3</i>	1	Aluminum	Nitrogen	2.0 MPa	7250
<i>4</i>	1	Aluminum	Nitrogen	2.5 MPa	7250
<i>5</i>	2	Aluminum	Nitrogen	1.0 MPa	7250
<i>6</i>	2	Aluminum	Argon	1.0 MPa	7250
<i>7</i>	3	Aluminum	Nitrogen	1.0 MPa	7250
<i>8</i>	3	Material X	Nitrogen	1.0 MPa	7250
<i>9</i>	3	Steel	Nitrogen	1.0 MPa	7250
<i>10</i>	3	Aluminum	Nitrogen	2.0 MPa	7250
<i>11</i>	3	Aluminum	Nitrogen	1.0 MPa	3625
<i>12</i>	3	Aluminum	Nitrogen	1.0 MPa	36250

Table 4 shows the simulations included in this chapter. Since higher gas pressures induce incredibly high velocities, time step decreases with increasing gas pressure. The time step would be further reduced if a finer mesh is utilized in the simulations. Therefore, the effect of gas pressure is obtained using mesh 1 (Cases 1 through 4 – gas pressures varied from 1-2.5 MPa). However, to understand the impact of the mesh, two gas pressures (1 and 2 MPa) are simulated using mesh 3 (Case 7 and 10).

Cases 7, 8, and 9 are used to obtain the effect of the melt properties. The three melts investigated in this study are aluminum, Material X (artificial material with intermediate thermophysical properties), and steel. 1 MPa gas pressure is used for all the simulations to reduce the computational time. Cases 5 and 6 are used to obtain the effect of atomizing gas properties. Molten aluminum is atomized using nitrogen and argon. Three melt flow rates (cases 7,11, and 12) are used to study the impact of melt flow rate. Table 5 shows the thermophysical properties used in the simulations.

Table 5 – Thermophysical Properties

<i>Material</i>	Density $\left(\frac{kg}{m^3}\right)$	Kinematic viscosity $\left(\frac{m^2}{s}\right)$	Surface tension $\left(\frac{N}{m}\right)$
<i>Aluminum</i>	2400	1.23×10^{-6}	0.8
<i>Material X</i>	4107	0.523×10^{-6}	0.793
<i>steel</i>	7000	4.285×10^{-7}	1.1
<i>Nitrogen</i>	1.205	15.11×10^{-6}	–
<i>argon</i>	1.449	26.6×10^{-6}	–

Effect of the Gas Pressure on the Atomization Process

Figure 26 shows the time evolution of 1 and 2.5 MPa gas pressure simulations. The main difference between these two gas pressures is the rate of progression of the atomization process. For the case of 2.5 MPa, the gas pressure induces a much higher gas velocity and contributes to enhanced atomization due to higher gas momentum flux. Consider the time evolution of 2.5 MPa gas pressure (second row). First, the gas stream impinges and penetrates the melt stream. At 0.4 ms, the gas penetrates the melt stream and divides it into two portions at the point of impact. The top melt portion moves upwards due to the strong gas recirculation for 2.5 MPa to accumulate near the melt-tip. For 1 MPa gas pressure, similar characteristics can be observed, however at a slower rate.

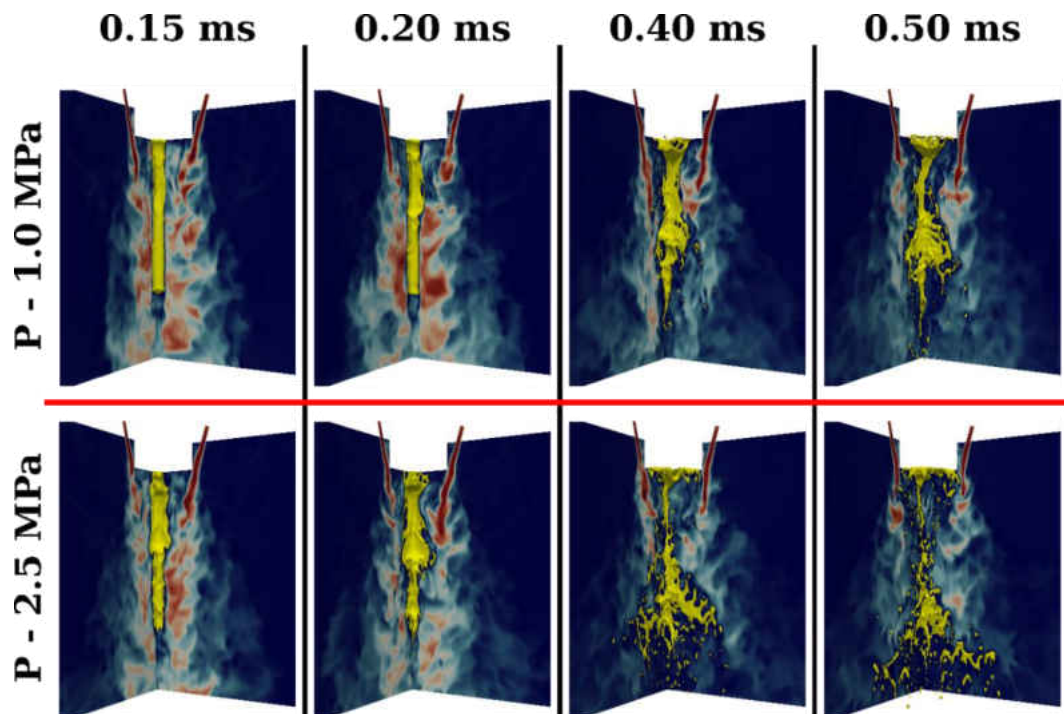


Figure 26 – Time evolution comparison of 1 and 2.5 MPa gas pressures

Figure 27 shows the droplet statistics for cases 7 and 10 (aluminum atomization with 1 MPa and 2 MPa gas pressures in mesh number 3). Figure 27a shows the time evolution of the number of droplets. The original distribution (red circle) of 1.0 MPa gas pressure shows a peak in the number of droplets at 1.2 ms and that for 2.0 MPa gas pressure is at 0.8 ms. It is due to the higher rate of evolution in the 2.0 MPa gas pressure. Also, in case 10, the number of droplets inside the computational domain comes to a steady-state around 1.2 ms.

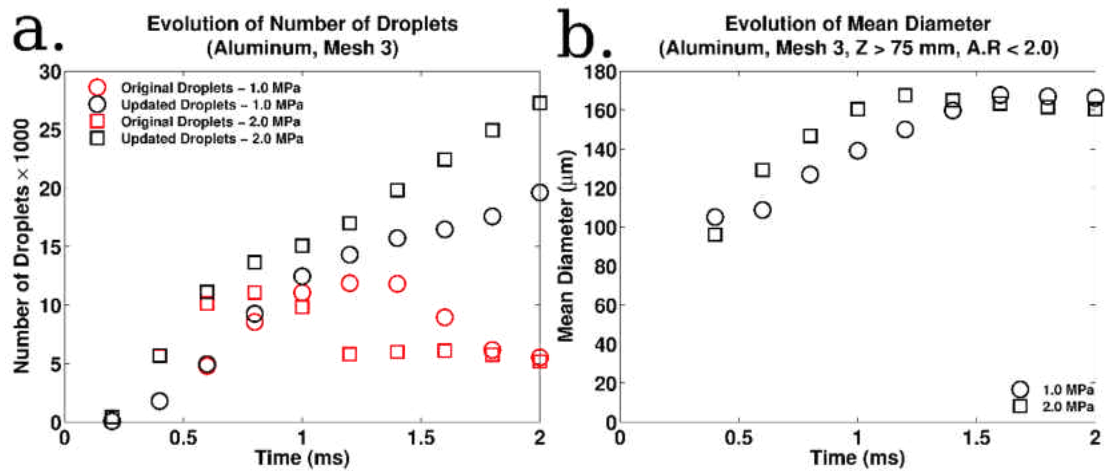


Figure 27 – Effect of gas pressure (Mesh 3), a. time evolution of the number of droplets, b. time evolution of mean diameter ($Z > 75$ mm, $AR < 2$)

Figure 27b shows the time evolution of the mean diameter of discriminated or secondary atomized droplets (refer Figure 23b for more information). Both gas pressures show an increasing mean diameter at the early stages of the atomization process, however, they reach the peak mean diameter at different times. Since 2 MPa gas pressure induces higher gas velocity, droplets have the potential to leave the computational domain at a much faster rate. Therefore, the mean diameter corresponding to 2 MPa gas pressure reaches the peak at an earlier time, around 1.2

ms, while 1 MPa gas pressure simulation reaches a peak around 1.6 ms. Once they reach the peak, a slight decrement in mean diameter can be observed with time. As expected, 2 MPa gas pressure simulations show a higher decrement in droplet diameter than 1.0 MPa gas pressure due to the higher momentum transfer.

Table 6 – Characteristic time scales – effect of inlet gas pressure

<i>Gas Pressure</i>	$U_g \left(\frac{m}{s} \right)$	$\tau_1 (ms)$		$\tau_2 (ms)$	
		Simulation	Estimated	Simulation	Estimated
1 MPa	1130	1.2	-	1.6	-
2 MPa	1630	0.8	0.73	1.2	0.98

Table 6 shows the characteristic time scales corresponding to the two gas pressures. Both τ_1 and τ_2 are estimated and compared with the simulation results shown in Figure 27. Since both simulations consider the atomization process of aluminum using high-pressure gas atomization with the same melt flow rate, the Equation 22 can be simplified as

$$\tau_c \propto (U_g)^{-\frac{4}{3}} \quad (23)$$

As shown in Table 6, the characteristic time scales are matched with the simulations for different gas pressures, confirming the validity of Equation 22.

Figure 28 shows a comparison of cumulative volume plots for different gas pressures with the experimental results obtained in a discrete gas atomizer. Figure 28 is a continuation of Figure 15. Four gas pressures (1, 1.5, 2 and 2.5 MPa) are

compared with the experimental results for five gas pressures (1, 1.5, 2, 2.5, and 3 MPa). The simulation results are obtained using the mesh one (Cases 1 through 4) as conducting higher gas pressure simulations in a fine mesh such as mesh three would be prohibitively expensive. It should be noted that the experimental cumulative volumes are normalized using the collected powder volume, and in the numerical results, all the droplets are considered without any discrimination based on the location or aspect ratio.

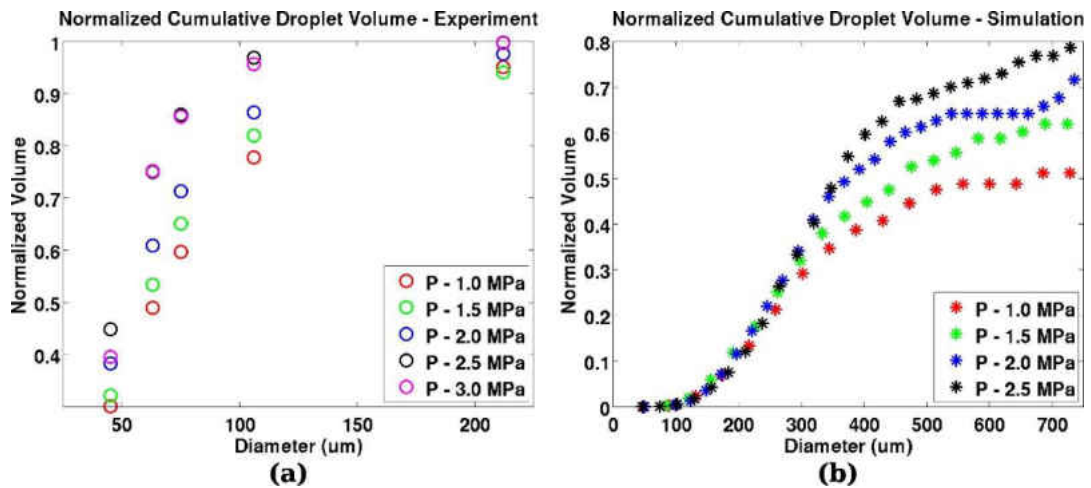


Figure 28 – Normalized cumulative volume, a. Experimental results (close-coupled, discrete gas atomizer), b. Numerical results – mesh 1 (close-coupled, annular-slit gas atomizer)

The numerical simulations show that up to $\sim 300 \mu\text{m}$ diameter, there is no significant difference in normalized volume for all gas pressures. The discrepancy becomes significant beyond $300 \mu\text{m}$. The numerical results show an improvement in the atomization with increasing gas pressure. For an example, the cumulative normalized volume for 1 MPa and 2.5 MPa at 0.6 mm droplet diameter is 0.48 and 0.73 respectively. The experimental results also show a similar trend. However, the

experimental results show no improvement in the atomization process beyond 2.5 MPa gas pressure. This may be due to the compressibility effect of the gas phase. At higher gas pressures, the structure of the shock waves does not change significantly with the increasing gas pressure. Therefore, the momentum transfer from the gas phase remains the same, irrespective of the gas pressure. However, the numerical simulations neglect the compressibility effects, hence could not show such variation.

Effect of the Melt Properties on the Atomization Process

Atomization of three molten metals (aluminum, Material X, and steel) with different thermophysical properties (Table 5) is investigated in this section. An artificial material (Material X) with intermediate thermophysical properties is introduced to obtain an accurate trend. More information on simulation parameters is included in Table 4.

Figure 29 shows the time evolution of melt-gas interaction for the three melts. The rate of evolution of the atomization process decreases with increasing melt density as in steel. Low-density aluminum atomizes at a much faster rate compared to material X and steel. The inlet gas pressure is maintained in the same for all three simulations. However, due to the density difference, the inertia of the melt and their resistance to deformation and breakup can vary. For example, in Figure 29, at $t = 0.75$ ms steel has still not undergone the melt disintegration at the point of impact. Thus, the density difference alone is the reason for the variation in rate of atomization with time. Irrespective of their rate of evolution, all three melts follow similar atomization physics as explained in Figure 16. All three melts display surface waves due to Kelvin-Helmholtz interfacial instability, and with time, these surface waves become

increasingly unstable creating liquid sheets and ligaments. Meanwhile, at the point of impact, the atomizing gas penetrates the metal and divide the melt into two segments. All three melts show these characteristics.

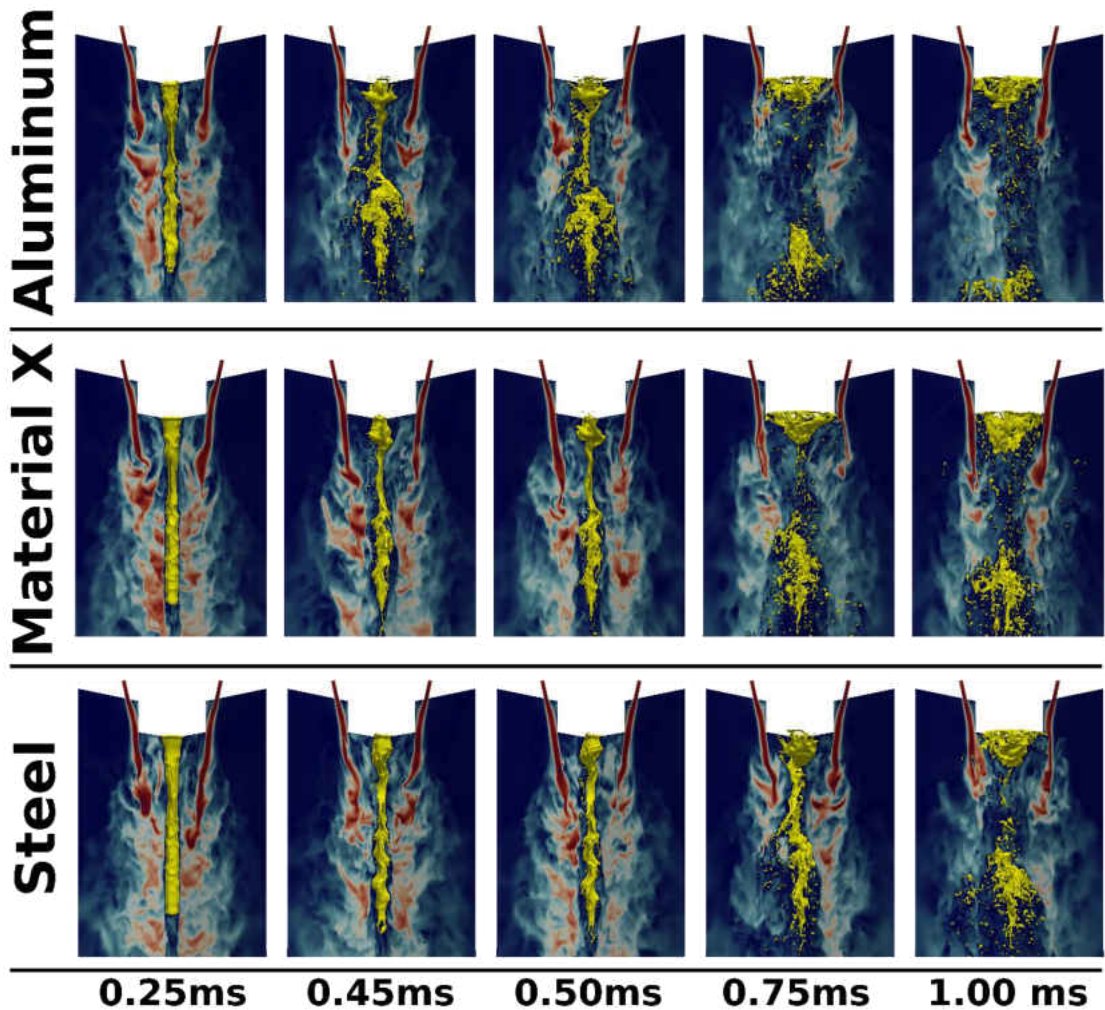


Figure 29 - Time evolution of the melt and gas interaction (effect of melt properties)

For a better understanding of the atomization process, the cross-sectional view at 30° is shown in Figure 30. The black color contours represent the melt-gas interface. The background colors represent the vorticities perpendicular to this plane. Yellow represents vorticity pointed into the page, and blue shows vorticity out of the

page. These images clearly show the variation of surface waves and the amplification of the instability with time. However, it should be noted that these are three-dimensional surface waves and deformations that include azimuthal transport. This can be seen in aluminum simulations at 0.35 ms (circled in red) when a sudden appearance of a ligament due to its azimuthal movement can be seen.

Since steel atomizes at a much slower rate, it can be used to investigate the generation of surface waves. At 0.2 ms, there is hardly any surface wave, however, slight surface modulations can be observed starting from 0.25 ms. Two parameters affect these surface waves. The first is the relative velocity between melt and gas phases. Once these surface waves are generated, the instability further grows until the ligament stretches and breaks up, as shown by the blue circle at 0.3 ms. The instabilities behind the generation of these surface waves and their subsequent breakup process are discussed in the previous section. The second factor that affects the surface wave is from Rayleigh-Taylor instability due to air penetration at the point of impact. This air penetration forces the melt to move either upward or downward direction. The downward moving melt counteracts with the surface waves partly due to relative velocities in the neighborhood of the ligament. This can be seen in material X at 0.3 ms and 0.35 ms time intervals (circled in black). At 0.3 ms, there are two distinct extended structures. However, these two structures are combined without breaking up as it does in aluminum (circled in blue). With the extra melt pushing towards these structures, the instability occurs due to relative velocity, which forces them to combine. Initially the upward moving melt facilitates surface waves as seen in steel simulations (circled in yellow).

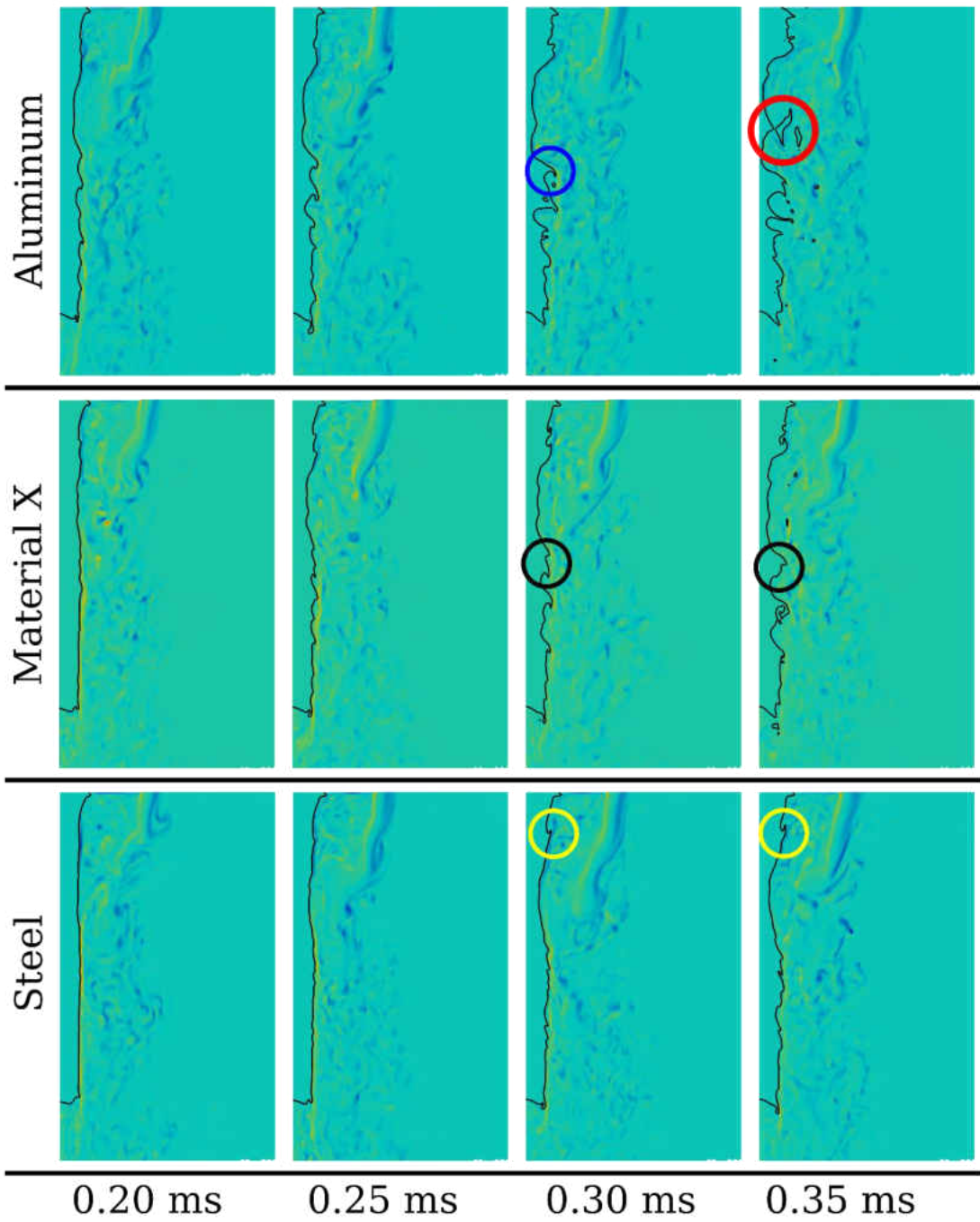


Figure 30 – Early stages of the atomization process – vorticity (2-D images show the cross-sectional view at 30° . The black color contours show the melt-gas interface (melt is present at the left side of the contour). The color plots indicate the vorticity perpendicular to the cross-section. Yellow color represents the vorticity vector pointing towards the page, and the blue color represents the opposite direction.

There is a strong circulation area in the gas side between the melt-tip and the point of impact. This also forces the melt in the upward direction, creating surface waves. Small portions of these melts are then accumulated near the melt-tip, as also observed in the experiments.

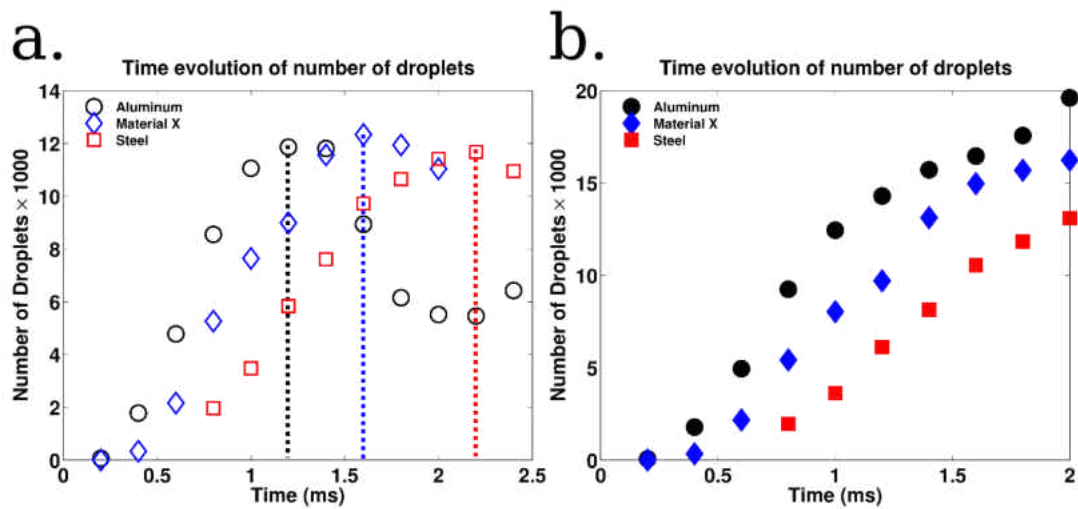


Figure 31 - Time evolution of the number of droplets – effect of melt properties, a. Original distribution, b. Updated distribution

Figure 31 shows the time evolution of the number of droplets for three different molten metals. The original distributions (Figure 31a) show that all three melts follow a similar trend. However, the peak time changes with the melt. The low-density aluminum reaches a peak around 1.2 ms and material X and steel at 1.6 ms and 2.2 ms, respectively. Since this peak occurs primarily due to the balance between the number of droplets generated and the number of droplets leaving the computational domain, it can be assumed that all three melts are at the same stage of the atomization process when the peak in number of droplets occurs. However, due to the variation in the rate of evolution (due to the inertia or the density of the melt),

each melt achieves the peak at different rates. Figure 31b shows the updated number of droplets. The total number of droplets decreases with increasing density as the higher density liquids atomize at a slower rate.

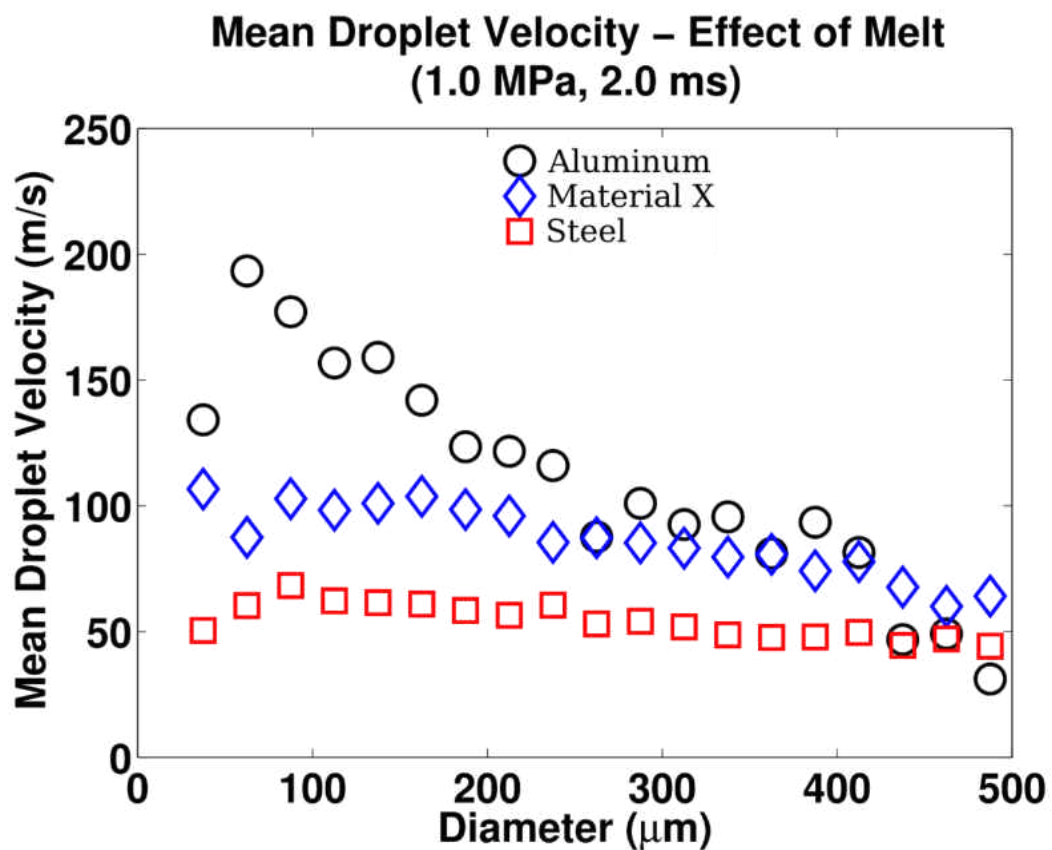


Figure 32 - Mean droplet velocities as a function of droplet diameter at 2 ms – effect of melt

Figure 32 shows the mean droplet velocities as a function of diameter for the three melts at 2 ms. The smaller droplets induce higher velocities and the droplet velocity decreases with the droplet diameter. This is due to the higher inertia of the larger droplets. This trend can be seen in all three melts. When comparing the three melts at a given droplet diameter, aluminum droplets have a higher mean velocity,

and the mean velocity decreases with the increasing melt density. As an example, for 100 μm droplet, the mean velocities of the aluminum, material X, and steel droplets are around 160, 110, and 60 m/s, respectively. Similarly, this variation is due to the differences in melt inertia.

In Figure 33, a comparison of normalized cumulative volume for the three melts is shown at 2 ms. Only the droplets which satisfy the conditions $AR < 2$ in $Z > 75$ mm (secondary atomized droplets) are considered. These cumulative plots provide the yield of the atomization process and display the effectiveness of the atomization process. Steel provides a better yield compared to other two melts and the yield increases with melt density. In the secondary breakup process, higher aerodynamic Weber number droplets tend to breakup further until they reach a critical Weber number (Choudhury, 2015; Saha et al., 2012). The aerodynamic Weber number is defined as $\frac{\rho_g U_{rel}^2 d}{\sigma}$, where U_{rel} is the relative velocity between gas and the droplet (i.e., $U_{rel} = U_g - U_l$). Since high-density liquids provide more resistance towards the gas flow (Figure 32), the induced velocities of the steel droplets are much smaller than that of material X and aluminum. Since the gas pressure is maintained at 1 MPa for all three simulations, the gas velocity is the same or in the same order of magnitude for all three simulations. Therefore, the aerodynamic Weber number of the high-density melts is much higher than low-density melts; hence high-density liquids have higher potential to breakup further.

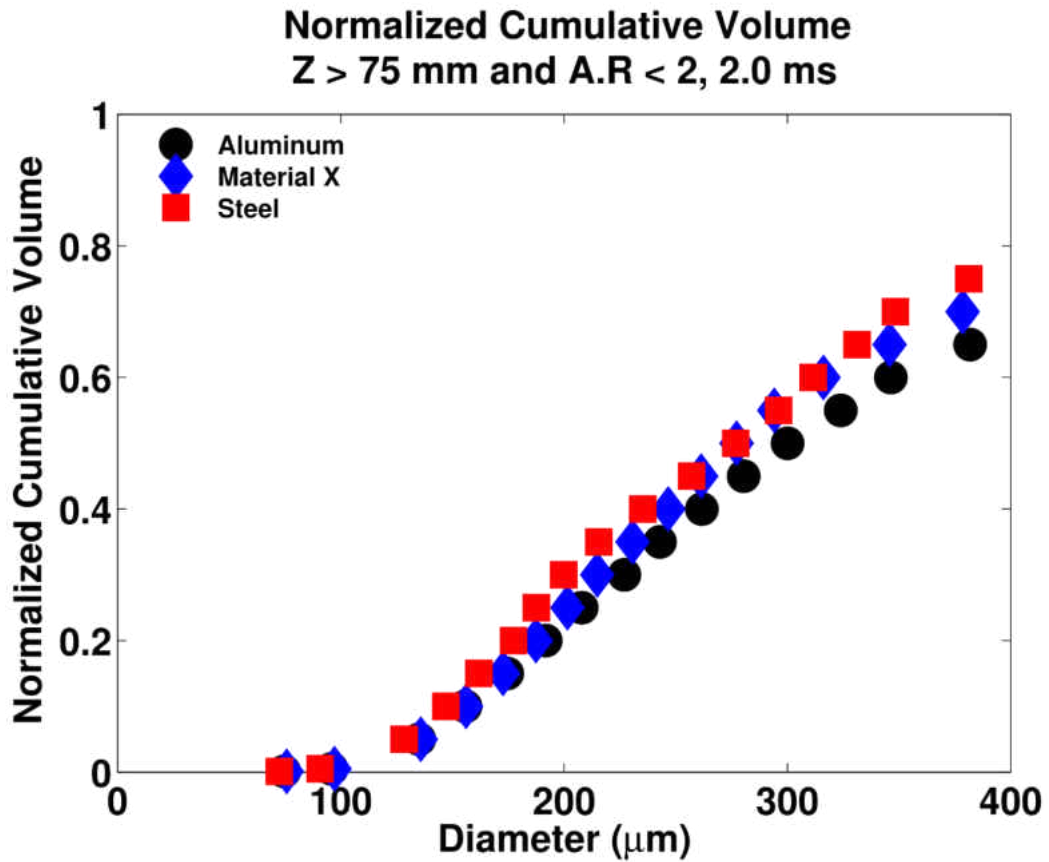


Figure 33 - Normalized cumulative volume graphs – effect of molten metal properties

Figure 34 shows the droplet size distributions corresponding to the droplets that are discriminated based on axial location ($Z > 75$ mm) at 2 ms. It should be noted that the number of droplets is decreasing with increasing density. As the droplets are discriminated based on the axial location, aluminum simulation provides the most droplets (i.e., – aluminum is evolving at a much higher rate than the other two melts). Irrespective of the melt properties, all three melts show the peak in the number of droplets in 120 – 140 μm diameter range.

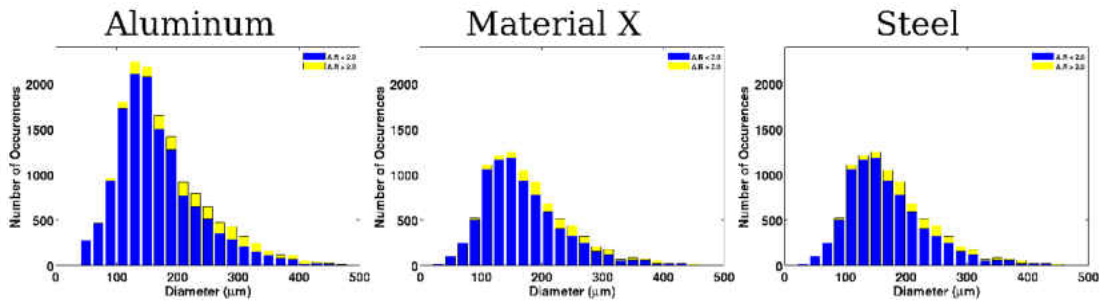


Figure 34 - Droplet size distributions (2 ms) – $Z > 75$ mm (blue color – droplets with $A.R \leq 2$, yellow color – droplets with $A.R < 2$)

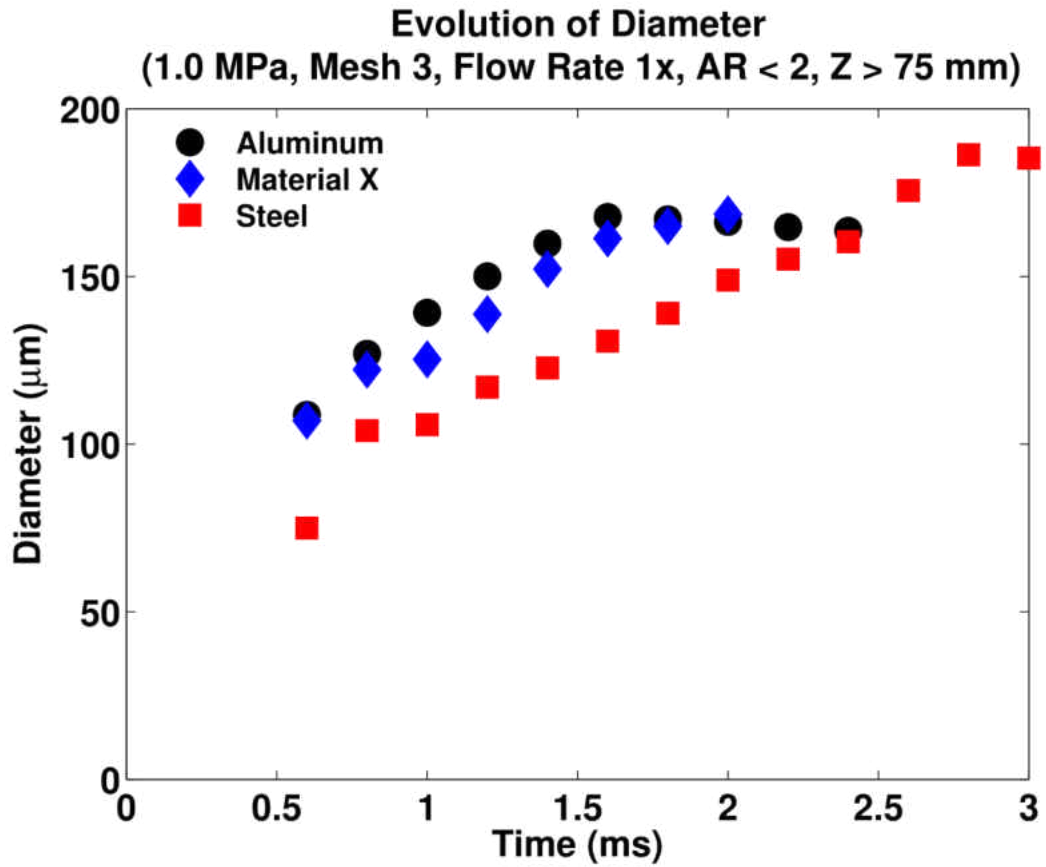


Figure 35 - Time evolution of mean diameter – effect of melt properties (Cases 7, 8 and 9, 2.0 ms, $Z > 75$ mm, $AR < 2.0$)

Figure 35 shows the time evolution of the mean diameter for the cases 7,8, and 9. The comparisons are made at 2 ms, and only the secondary atomized droplets are used for the mean diameter calculations. All three melts show similar variation in the mean diameter at the early stages of the atomization process. The mean diameter for the aluminum droplets reaches its peak around 1.6 ms, and the other two melts do not reach the peak within the time shown in Figure 35. The material X simulation shows that it is close to the peak location as the slope is getting smaller around 2 ms. However, the mean diameter of steel droplets continuously increases with time.

Table 7 – Characteristic time scales – effect of melt properties

<i>material</i>	τ_1 (ms)		τ_2 (ms)	
	Simulation	Estimated	Simulation	Estimated
<i>Aluminum</i>	1.2	-	1.6	-
<i>Material X</i>	1.6	1.56	-	-
<i>Steel</i>	2.2	2.05	2.8	2.73

Table 7 shows the characteristic times scales for the three melts. For these simulations, Equation 22 can be simplified as

$$\tau_c \propto \sqrt{\rho_m} \quad (24)$$

Table 7 also verify Equation 22 for both time scales. As Equation 22 can predict both time scales successfully, it can be used to predict the simulation times for future simulations (with different operational parameters) to achieve similar

atomization characteristics (i.e., time to reach the peak in number of droplets, time to reach the peak in mean diameter.).

Effect of the Gas Properties on the Atomization Process

This section discusses the effect of gas properties on the atomization process using cases 5 and 6. Molten aluminum is atomized using nitrogen and argon at 1 MPa gas pressure using the mesh number two. As shown in Table 5, the main difference between argon and nitrogen is the slight variation in density. It will slightly increase the gas momentum in argon, however, as the total pressure is specified at the gas inlet. Therefore, the inlet gas velocity of argon is somewhat lower than that of nitrogen.

Figure 36 shows a comparison of the interfacial dynamics for the two cases. It does not show any significant variation in the atomization process. Both simulations show the same characteristics and interfacial instabilities discussed in Chapter 4. However, a small delay in the atomization process can be observed in aluminum-nitrogen combination (i.e., time delay in flow disintegration at the point of impact at 0.5 ms).

Figure 37 shows the statistics of secondary atomized droplets. Figure 37a shows the droplet size histograms. A slight increment in the number of secondary atomized droplets can be observed. The mean diameters for argon and nitrogen simulations are $187.9 \mu\text{m}$ and $200.3 \mu\text{m}$, respectively.

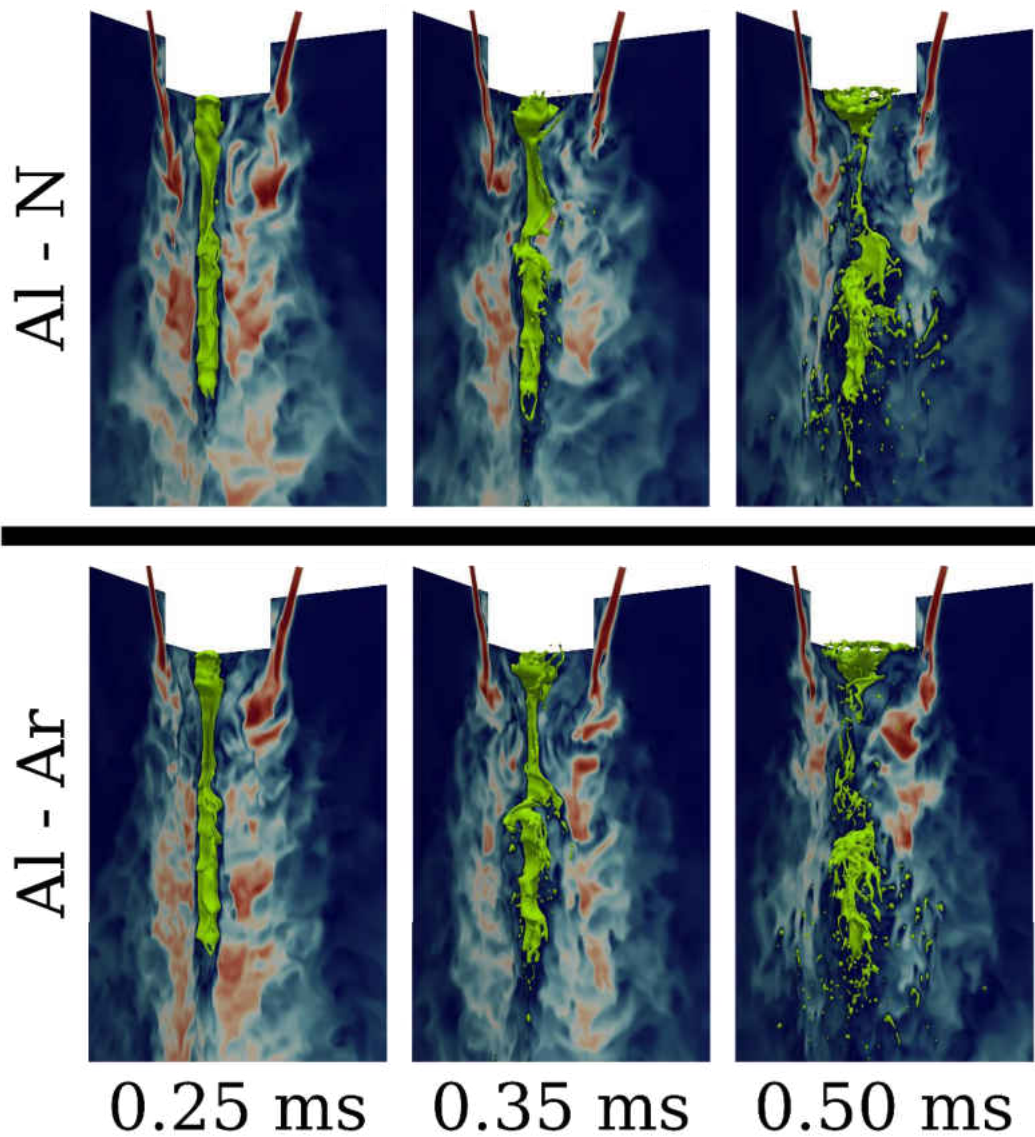


Figure 36 – Effect of atomizing gas on the aluminum atomization process, nitrogen (top row), argon (bottom row)

Figure 37b shows the normalized cumulative volume graphs for cases 5 and 6. Both simulations show an identical distribution beyond $200\ \mu\text{m}$ diameters. A slight improvement can be observed in Al-Ar simulation between $100\text{-}200\ \mu\text{m}$ diameters. This is due to increased number of droplets in the Al-Ar simulation within that diameter range.

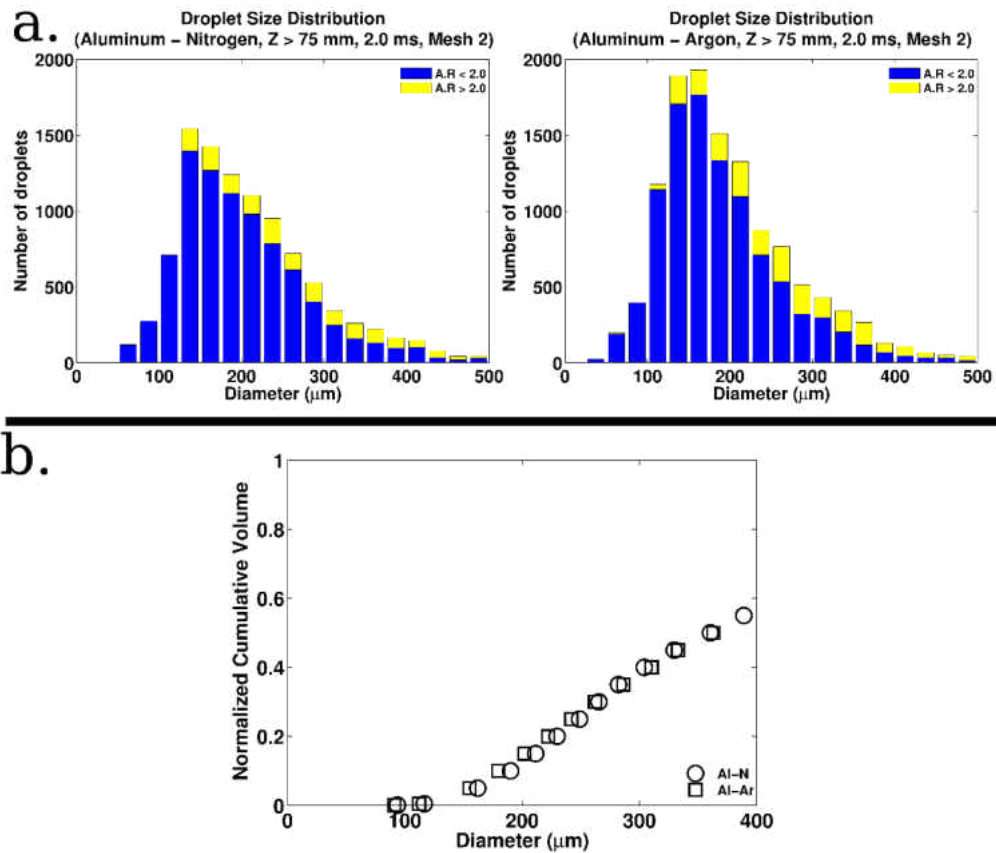


Figure 37 – Effect of the atomizing gas on aluminum atomization, a. The size distribution of the secondary atomized droplets, Aluminum – Nitrogen (left), Aluminum – Argon (right), b. Comparison of normalized cumulative volume of the secondary atomized droplets (2 ms)

Effect of the Melt Flow Rate on the Atomization Process

The effect of the melt flow rate on the droplet size distributions is considered next by changing the volume flow rate. Case 7 ($Q_0 = 7250 \frac{mm^3}{s}$) is taken as the base case and two other simulations (Cases 11 and 12) with $0.5Q_0$ and $5Q_0$ are used to make a comparison. As done for all cases, the simulations are initiated with the same amount of melt inside the computational geometry.

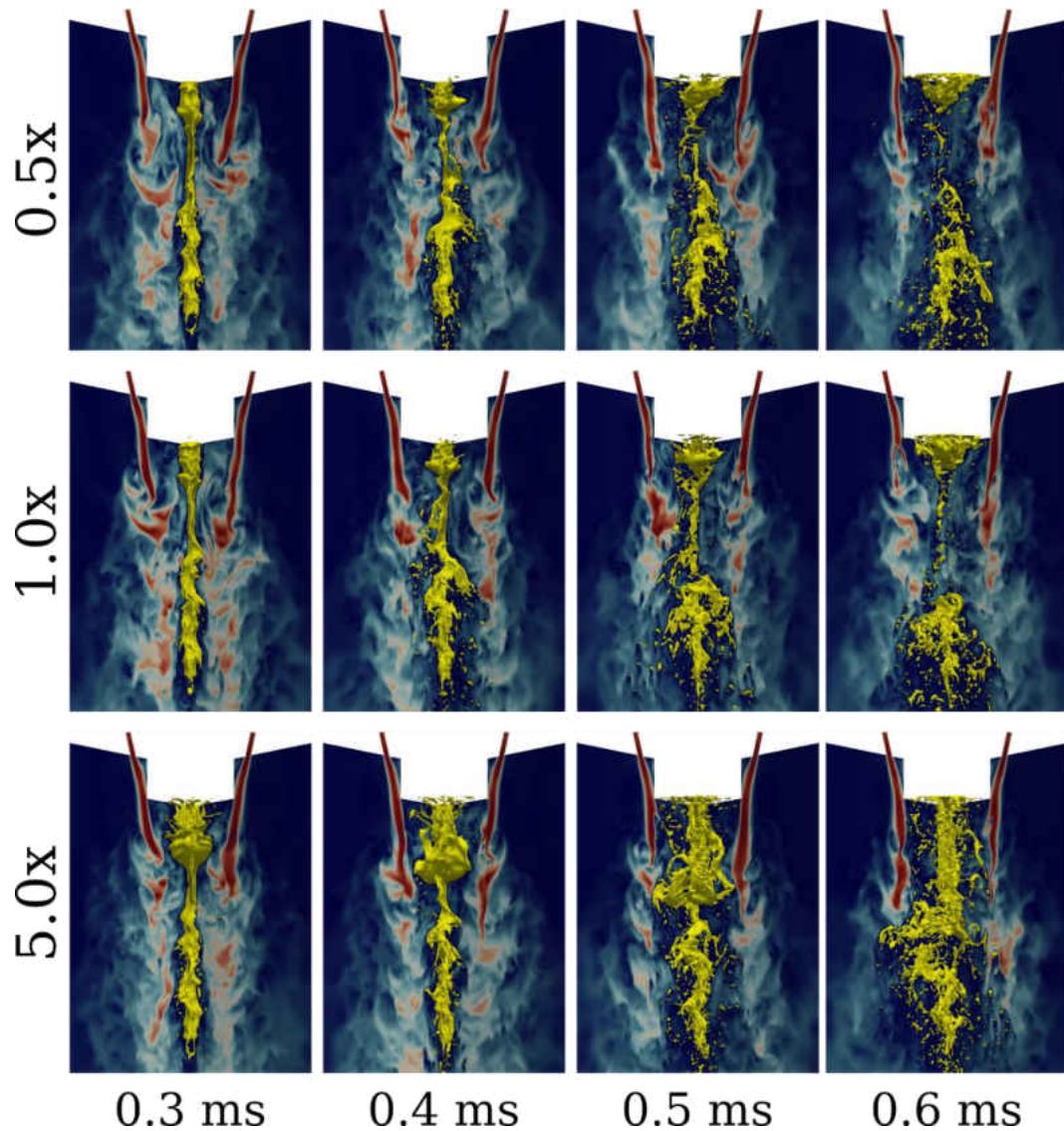


Figure 38 – Time evolution of melt-gas interaction – effect of melt flow rate (cases 7, 11, and 12)

The numerical flow visualization of atomization for $0.5Q_0$ and Q_0 (cases 11 and 7 respectively) in Figure 38 does not show significant differences in the flow patterns and atomization characteristics. Both simulations show the critical characteristics of surface waves, gas penetration at the point of impact, and flow disintegration.

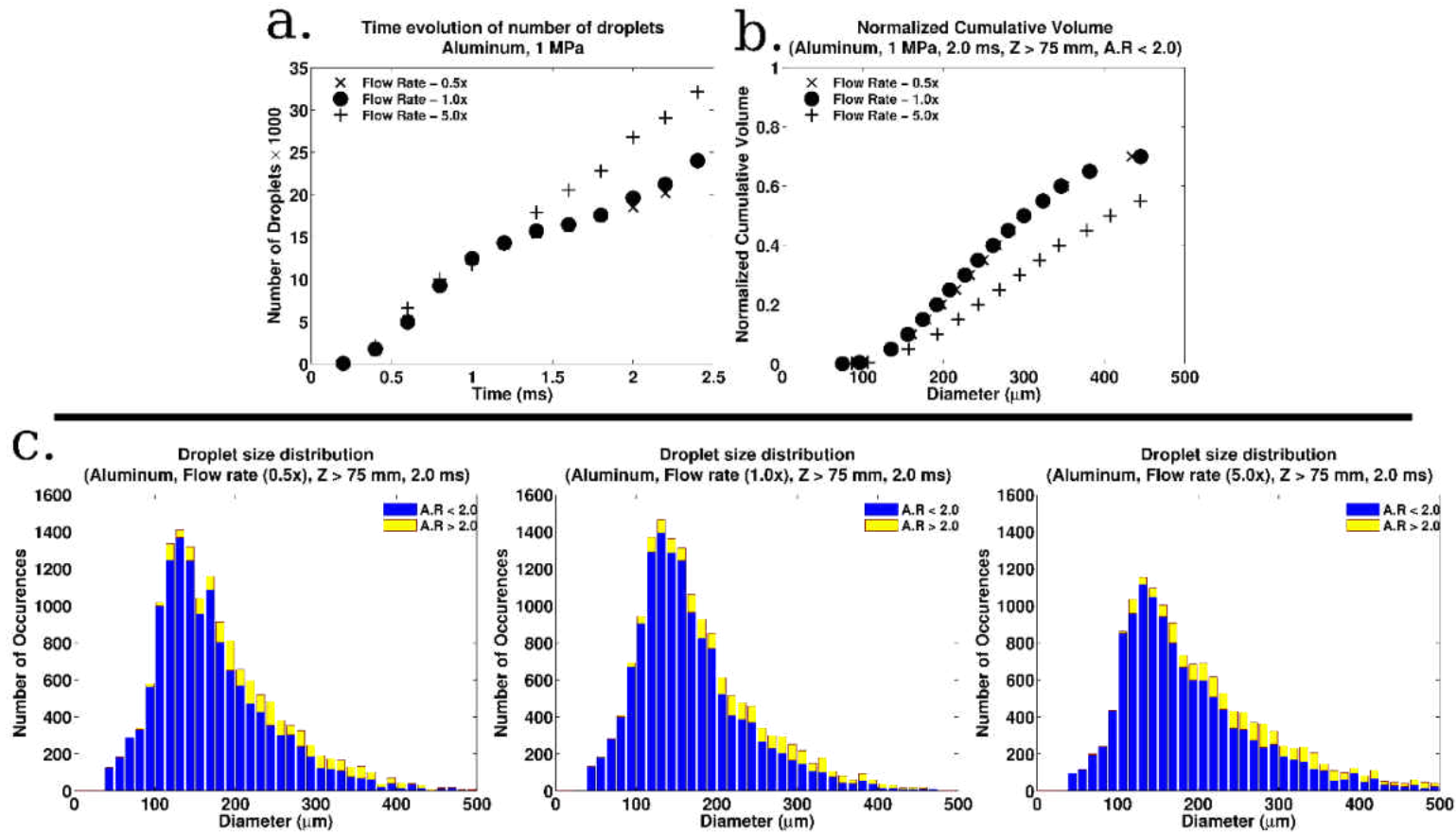


Figure 39 – Effect of melt flow rate (cases 7, 11, and 12), a. time evolution of the number of droplets, b. normalized cumulative volume, c. droplet size distribution

Only slight changes can be observed in the rate of progression of the atomizing melt stream. Due to the slower replenishment of the melt for low flow rate (Case 11), a faster upward movement can be observed near the melt tip. This enables the melt to disintegrate (at the point of impact) at a slightly faster rate.

However, significant differences in the atomization process can be observed between Cases 7 and 12. The higher melt flow rate (Case 12) replenishes the melt quickly and provides a higher resistance to the recirculating gas near the point of impact. A significant amount of melt accumulating within the point of impact, and the melt-tip can be observed at 0.3 ms. The downward melt velocity and the upward gas movement create a bag-like structure at 0.4 ms for Case 12, which breakup up in the subsequent time steps as a result of melt gas interaction. This bag-like structure creates a thin sheet of melt, and due to the gas interaction, it further stretches and tears into ligaments and droplets. This flow mechanism has some similar characteristics to the bag breakup in secondary atomization, even though it is categorized as primary breakup. A flow disintegration at the point of impact can be observed at 0.6 ms.

The flow characteristics of Case 12 are entirely different from Cases 7 and 11 and are seen to be less efficient, as seen in the cumulative volume plot in Figure 39. The total number of droplets in the fourth quadrant significantly increases for the higher flow rate but does not change for Cases 7 and 11. It is assessed that Case 12 is at a very early stage of the atomization process compared to the other two cases since the number of droplets that appear in the fourth quadrant is relatively small compared to those for low flow rates.

All three flow rates show the peak in droplet size distribution histograms in the 125-137 μm diameter range. However, the percentage of the number of droplets in

this diameter range varies as 7.2, 7.2, 9 in the order of increasing flow rate. The percentage of number of droplets larger than 300 μm diameter varies as 7.8, 7.2, and 30%. Cases 11 and 7 show similar values, and it shows that most of the atomization has already taken place within this time period and computational domain. However, for Case 12, around 30% of the droplets have diameters above 300 μm . It shows that the higher melt flow rates may need a longer computational domain and have to run for extended period to reach similar level of atomization.

Table 8 – Characteristic time scales – effect of melt flow rate

<i>Flow rate</i>	τ_1 (ms)	
	Simulation	Estimated
$0.5 \dot{Q}_0$	1.2	0.96
$1.0 \dot{Q}_0$	1.2	-
$5.0 \dot{Q}_0$	2	2.05

Table 8 shows the validity of Equation 22 for different melt flow rates. The simulation shows that both Cases 11 and 7 have the same characteristic time scale. Since the peak in the simulations are obtained by comparing the values at 0.2 ms time intervals, it only provides a rough estimation.

CONCLUSIONS

The effects of several operational parameters have been studied in the high-pressure gas atomization process. A VOF-based, three dimensional, Eulerian-Eulerian simulations, which do not involve any semi-empirical correlations, have been conducted to understand the simultaneous primary and secondary atomization processes and capture detailed information on the droplet sizes and cumulative volume. Thus, the simulation does not involve any facilitation of a breakup process as it occurs naturally without any modeling. The cumulative volume trends obtained for four gas pressures, three melts of different thermophysical properties, two atomizing gases and three different flow rates have been analyzed. Direct comparison with the experiments is not possible since an annular-slit nozzle is used for computations, whereas the experiments used multiple circular nozzles around the melt inlet; however the computations predict the correct trend. Filtering the droplets in the fourth quadrant including the droplets that left the computational domain and discriminating them based on an aspect ratio less than two, it is possible to simulate near-complete primary and secondary atomization in 2 ms for all melts within 100 mm in the axial direction of a larger chamber.

Interfacial dynamics in aluminum-nitrogen, melt gas combination shows the presence of several interfacial instabilities at different stages of the atomization process. The identified interfacial instabilities governing the primary atomization process are the Kelvin-Helmholtz instability and Rayleigh-Taylor instability. Due to the higher gas momentum, the melt-gas interface seems to be peeled off forming ligaments, instead of deforming and inducing bag like structures (bag breakup). Later these ligaments breakup into smaller droplets due to the Rayleigh-Taylor instability.

A combination of these two instabilities governs the generation of surface waves and their subsequent breakup process. Rayleigh-Plateau and capillary instabilities drive the secondary atomization process. A novel approach is introduced to visualize the vorticity variations at the melt-gas interface in three-dimension and described its capability to explain the breakup process. A ligament formation mechanism based on the azimuthal movements is identified at the early stages of the atomization process. The perturbations in the gas flow due to its interaction with the melt tube is found to be the origin of these azimuthal variations.

Increasing gas pressure is found to be favorable for the atomization process in terms of the yield due to the higher momentum transfer at the melt-gas interface. The rate of the atomization process is increased significantly with increasing gas pressure. However, the key characteristics of the atomization process did not change.

Three molten metals/alloys (aluminum, an artificial material, and steel) have been considered for capturing the effect of melt thermophysical properties. The rate of evolution of the atomization process decreases with increasing melt inertia. However, similar flow characteristics are observed irrespective of the differences in the melt properties. The dynamics of the surface waves are further investigated using two-dimensional cut planes. The presence of the abovementioned interfacial instabilities is observed. It is found that the melt inertia has a strong influence on how the interfacial instabilities interact with one another. The yield of the atomization process is found to be increasing with increasing melt density.

The effect of the atomizing gas on the high-pressure gas atomization process is studied by comparing the atomization of molten aluminum with nitrogen and argon as the atomizing gas. Significant changes in the atomization process have not been

observed in terms of the interfacial dynamics, and the cumulative volume plots as argon and nitrogen have relatively similar thermophysical properties. However, a slight improvement in the droplet size distribution can be observed in aluminum-argon, melt gas combination.

Three melt flow rates are compared to obtain the effect of melt flow rate on the atomization process and the powder size distribution. Increasing melt flow rate can significantly vary the characteristics of the primary atomization. Small flow rates are prone to experience a strong reverse flow near the melt-tip and obstruct the melt inlet. Higher melt flow rates replenish the melt inside the computational domain at a higher rate, increasing melt-gas interactions. However, due to added resistance towards the gas flow, the gas momentum decreases, resulting in a decrement in the effective momentum transfer to the melt stream. Therefore, the rate of evolution of the atomization process decreases, resulting in longer computational times.

A characteristic time scale has been introduced to describe the rate of progression of the atomization process for different operational parameters. The validity of the relationship is verified by comparing it with the simulations using two physical characteristic time scales. This characteristic time scale can be utilized to estimate how long does it needs to conduct a numerical simulation with different operational parameters to reach a similar level of the atomization process.

Despite the computational difficulties and the assumptions made in this investigation, the trends can be predicted reasonably well for the future design of experiments. A complete simulation of various melts at different flow rates and pressures may not be necessary for the entire duration of the atomization process in the entire chamber. Most of atomization is completed within 2 ms and 100 mm of the

atomization geometry. For high flow rates of the melt, longer computational times may be needed.

LIST OF REFERENCES

- Alan Lawley. (1978). PREPARATION OF METAL POWDERS. *Annual Review of Materials Research*, 8, 49–71.
- Albadawi, A., Donoghue, D. B., Robinson, A. J., Murray, D. B., & Delauré, Y. M. C. (2013). Influence of surface tension implementation in Volume of Fluid and coupled Volume of Fluid with Level Set methods for bubble growth and detachment. *International Journal of Multiphase Flow*. <https://doi.org/10.1016/j.ijmultiphaseflow.2013.01.005>
- Allimant, A., Planche, M. P., Bailly, Y., Dembinski, L., & Coddet, C. (2009). Progress in gas atomization of liquid metals by means of a De Laval nozzle. *Powder Technology*. <https://doi.org/10.1016/j.powtec.2008.04.071>
- Anderson, I. E., White, E. M. H., & Dehoff, R. (2018). Feedstock powder processing research needs for additive manufacturing development. *Current Opinion in Solid State and Materials Science*. <https://doi.org/10.1016/j.cossms.2018.01.002>
- Aydin, O., & Unal, R. (2011). Experimental and numerical modeling of the gas atomization nozzle for gas flow behavior. *COMPUT FLUIDS*. <https://doi.org/10.1016/j.compfluid.2010.10.013>
- Ayers, J.D., Anderson, I. . (1985). Very Fine Metal Powders. *Journal of Metals*, 37, 16–21.
- Basak, C. B., Krishnan, M., Kumar, R., Abdullah, K. K., & Anantharaman, S. (2014). Characterization and process evaluation of Ni-Ti-Fe shape memory alloy macro-spheres directly fabricated via rotating electrode process. *Journal of Alloys and Compounds*, 597, 15–20. <https://doi.org/10.1016/j.jallcom.2014.01.227>
- Bourlioux, A. (1995). A coupled level-set volume-of-fluid algorithm for tracking material interfaces. *6th International Symposium on Computational Fluid Dynamics, Lake Tahoe, Ca, Vol 15*.
- Brackbill, J. U., Kothe, D. B., & Zemach, C. (1992). A continuum method for modeling surface tension. *Journal of Computational Physics*, 100(2), 335–354. [https://doi.org/10.1016/0021-9991\(92\)90240-Y](https://doi.org/10.1016/0021-9991(92)90240-Y)
- Chandrasekhar, S., & Gillis, J. (2009). Hydrodynamic and Hydromagnetic Stability. *Physics Today*. <https://doi.org/10.1063/1.3058072>
- Chen, G., Zhao, S. Y., Tan, P., Wang, J., Xiang, C. S., & Tang, H. P. (2018). A comparative study of Ti-6Al-4V powders for additive manufacturing by gas atomization, plasma rotating electrode process and plasma atomization. *Powder Technology*. <https://doi.org/10.1016/j.powtec.2018.04.013>
- Choudhury, P. (2015). *Theoretical And Experimental Investigaton Of The Cascading*

Nature Of Pressure Swirl Atomization.

- Davanlou, A., Lee, J. D., Basu, S., & Kumar, R. (2015). Effect of viscosity and surface tension on breakup and coalescence of bicomponent sprays. *Chemical Engineering Science*. <https://doi.org/10.1016/j.ces.2015.03.057>
- Davies, T. V., & Batchelor, G. K. (1954). The Theory of Homogeneous Turbulence. *The Mathematical Gazette*. <https://doi.org/10.2307/3609796>
- Deshpande, S. S., Anumolu, L., & Trujillo, M. F. (2012). Evaluating the performance of the two-phase flow solver interFoam. *Computational Science & Discovery*, 5(1), 014016. <https://doi.org/10.1088/1749-4699/5/1/014016>
- Desjardins, O., Moureau, V., & Pitsch, H. (2008). An accurate conservative level set/ghost fluid method for simulating turbulent atomization. *Journal of Computational Physics*. <https://doi.org/10.1016/j.jcp.2008.05.027>
- Eggers, J., & Villermaux, E. (2008). Physics of liquid jets. *Reports on Progress in Physics*. <https://doi.org/10.1088/0034-4885/71/3/036601>
- Espina, P.E., Ridder, S.D., Biancaniello, F.S., Mattingly, G. E. (1989). Analysis of the Aspiration Phenomena in a Close-Coupled Inert Gas Atomizer, Characterization and Diagnostics of Ceramics and Metal Particulate. *TMS*, 49–62.
- Farvardin, E., & Dolatabadi, A. (2013). Numerical Simulation of the Breakup of Elliptical Liquid Jet in Still Air. *Journal of Fluids Engineering*. <https://doi.org/10.1115/1.4024081>
- Figliola, R.S., Anderson, I. E. (1993). Characterization of High Pressure Gas Atomization Flow Fields, Computational and Numerical Techniques in Powder Metallurgy. *TMS*, 29–39.
- Firmansyah, D. A., Kaiser, R., Zahaf, R., Coker, Z., Choi, T. Y., & Lee, D. (2014). Numerical simulations of supersonic gas atomization of liquid metal droplets. *Japanese Journal of Applied Physics*, 53(5 SPEC. ISSUE 3). <https://doi.org/10.7567/JJAP.53.05HA09>
- Fritsching, U. (2004). *Spray Simulation, Modeling and Numerical Simulation of Sprayforming Metals*.
- Fritshing, U., & Uhlenwinkel, V. (2012). Hybrid Gas Atomization for Powder Production. *Powder Metallurgy*, 99–124. <https://doi.org/10.5772/711>
- Gorokhovski, M., & Herrmann, M. (2008). Modeling Primary Atomization. *Annual Review of Fluid Mechanics*. <https://doi.org/10.1146/annurev.fluid.40.111406.102200>
- Grant, P. S., Cantor, B., & Katgerman, L. (1993a). Modelling of droplet dynamic and thermal histories during spray forming-I. individual droplet behaviour. *Acta*

- Metallurgica Et Materialia*. [https://doi.org/10.1016/0956-7151\(93\)90039-U](https://doi.org/10.1016/0956-7151(93)90039-U)
- Grant, P. S., Cantor, B., & Katgerman, L. (1993b). Modelling of droplet dynamic and thermal histories during spray forming-II. Effect of process parameters. *Acta Metallurgica Et Materialia*. [https://doi.org/10.1016/0956-7151\(93\)90040-Y](https://doi.org/10.1016/0956-7151(93)90040-Y)
- Guildenbecher, D. R., López-Rivera, C., & Sojka, P. E. (2009). Secondary atomization. *Experiments in Fluids*. <https://doi.org/10.1007/s00348-008-0593-2>
- Haghshenas, M., Wilson, J. A., & Kumar, R. (2017). Algebraic coupled level set-volume of fluid method for surface tension dominant two-phase flows. *International Journal of Multiphase Flow*. <https://doi.org/10.1016/j.ijmultiphaseflow.2016.12.002>
- Hanson, A. R., Domich, E. G., & Adams, H. S. (1963). Shock tube investigation of the breakup of drops by air blasts. *Physics of Fluids*. <https://doi.org/10.1063/1.1706864>
- Hanthanan Arachchilage, K., Haghshenas, M., Park, S., Zhou, L., Sohn, Y., McWilliams, B., ... Kumar, R. (2019). Numerical simulation of high-pressure gas atomization of two-phase flow: Effect of gas pressure on droplet size distribution. *Advanced Powder Technology*. <https://doi.org/10.1016/J.APT.2019.08.019>
- Hasslberger, J., Ketterl, S., Klein, M., & Chakraborty, N. (2019). Flow topologies in primary atomization of liquid jets: A direct numerical simulation analysis. *Journal of Fluid Mechanics*. <https://doi.org/10.1017/jfm.2018.845>
- Hattel, J. H., Pryds, N. H., Thorborg, J., & Ottosen, P. (1999). Quasi-stationary numerical model of atomized metal droplets. I: model formulation. *Modelling and Simulation in Materials Science and Engineering*. <https://doi.org/10.1088/0965-0393/7/3/309>
- Heck, U., Fritsching, U., & Bauckhage, K. (2000). Gas flow effects on twin-fluid atomization of liquid metals. *Atomization and Sprays: Journal of the International Institutions for Liquid Atomization and Spray Systems*, 10(1), 25.
- Hernandez, F; Riedemann, T; Tiarks, J; Kong, B; Regele, J.D; Ward, T; Anderson, I. . (2019). Numerical Simulation and Validation of Gas and Molten Metal Flows in Close-Coupled Gas Atomization. *He Minerals, Metals & Materials Series (Eds) TMS 2019 148th Annual Meeting & Exhibition Supplemental Proceedings*.
- Herrmann, M. (2011). On simulating primary atomization using the refined level set grid method. *Atomization and Sprays*. <https://doi.org/10.1615/AtomizSpr.2011002760>
- Hinze, J. O. (1955). Fundamentals of the hydrodynamic mechanism of splitting in dispersion processes. *AIChE Journal*. <https://doi.org/10.1002/aic.690010303>

- Hirt, C. W., & Nichols, B. D. (1981). Volume of fluid (VOF) method for the dynamics of free boundaries. *Journal of Computational Physics*, 39(1), 201–225. [https://doi.org/10.1016/0021-9991\(81\)90145-5](https://doi.org/10.1016/0021-9991(81)90145-5)
- Issa, R. I. (1986). Solution of the implicitly discretised fluid flow equations by operator-splitting. *Journal of Computational Physics*. [https://doi.org/10.1016/0021-9991\(86\)90099-9](https://doi.org/10.1016/0021-9991(86)90099-9)
- J.T, S. (2013). Lick back in close-coupled atomization: A phenomenological study. *5th International Conference on Spray Deposition and Melt Atomization, SDMA 2013*, 23–25.
- Jarrahbashi, D., & Sirignano, W. A. (2014). Invited Article: Vorticity dynamics for transient high-pressure liquid injection. *Physics of Fluids*. <https://doi.org/10.1063/1.4895781>
- Jasak, H., & Weller, H. (1995). Interface tracking capabilities of the inter-gamma differencing scheme. *Unknown*, (2), 1–9.
- Kaiser, R., Li, C., Yang, S., & Lee, D. (2018). A numerical simulation study of the path-resolved breakup behaviors of molten metal in high-pressure gas atomization: With emphasis on the role of shock waves in the gas/molten metal interaction. *Advanced Powder Technology*. <https://doi.org/10.1016/j.appt.2017.12.003>
- Kull, H. J. (1991). Theory of the Rayleigh-Taylor instability. *Physics Reports*. [https://doi.org/10.1016/0370-1573\(91\)90153-D](https://doi.org/10.1016/0370-1573(91)90153-D)
- Kuntz, D.W., Payne, J. . (1995). Simulation of powder metal fabrication with high pressure gas atomization. *Advances in Powder Metallurgy and Particulate Materials*.
- Lagutkin, S., Achelis, L., Sheikhaliev, S., Uhlenwinkel, V., & Srivastava, V. (2004). Atomization process for metal powder. *Materials Science and Engineering A*, 383(1 SPEC. ISS.), 1–6. <https://doi.org/10.1016/j.msea.2004.02.059>
- Li, X, Sander, S., & Ellendt, N. (2013). Coupled Simulation of Spray Process for Metal Matrix Composite Powder Production. ... *Atomization and Spray*
- Li, Xing gang, & Fritsching, U. (2017). Process modeling pressure-swirl-gas-atomization for metal powder production. *Journal of Materials Processing Technology*, 239, 1–17. <https://doi.org/10.1016/j.jmatprotec.2016.08.009>
- Ling, Y., Fuster, D., Zaleski, S., & Tryggvason, G. (2017). Spray formation in a quasiplanar gas-liquid mixing layer at moderate density ratios: A numerical closeup. *Physical Review Fluids*. <https://doi.org/10.1103/PhysRevFluids.2.014005>
- Lubanska H. (1970). Correlation of Spray Ring Data for Gas Atomization of Liquid

Metals. *J Metals*.

- Marmottant, P. H., & Villermaux, E. (2004). On spray formation. *Journal of Fluid Mechanics*. <https://doi.org/10.1017/S0022112003006529>
- Mates, S.P., Ridder, S.D., Biancaniello, F. S. (2000). Comparison of the supersonic length and dynamic pressure characteristics of discrete-jet and annular close-coupled nozzles used to produce fine metal powders. *TMS Annual Meeting in Nashville, Tennessee*, 71–81.
- Mates, S. P., & Settles, G. S. (2005a). A study of liquid metal atomization using close-coupled nozzles, Part 2: Atomization behavior. *Atomization and Sprays*, 15(1), 41–59. <https://doi.org/10.1615/AtomizSpr.v15.i1.30>
- Mates, S. P., & Settles, G. S. (2005b). Study of Liquid Metal Atomization Using Close-Coupled Nozzles, Part 1: Gas Dynamic Behavior. *Atomization and Sprays*, 15(1), 19–40. <https://doi.org/10.1615/AtomizSpr.v15.i1.20>
- Metz, R., Machado, C., Houabes, M., Elkhatib, M., & Hassanzadeh, M. (2008). Nitrogen spray atomization of molten tin metal: Powder morphology characteristics. *Journal of Materials Processing Technology*, 195(1–3), 248–254. <https://doi.org/10.1016/j.jmatprotec.2007.05.006>
- Mi, J., Figliola, R.S., Anderson, I. E. (1996). A numerical simulation of gas flow field effects on high pressure gas atomization due to operating pressure variation. *Material Science and Engineering A*, 208, 20–29.
- Mi, J., Figliola, R. S., & Anderson, I. E. (1997). A numerical investigation of gas flow effects on high-pressure gas atomization due to melt tip geometry variation. *Metallurgical and Materials Transactions B*. <https://doi.org/10.1007/s11663-997-0021-7>
- Miller, S. A., Miller, R. S., Mourer, D. P., & Christensen, R. W. (1997). High yield, nonaxisymmetric atomization of nickel base superalloys. *International Journal of Powder Metallurgy (Princeton, New Jersey)*. [https://doi.org/10.1016/S0026-0657\(99\)80018-6](https://doi.org/10.1016/S0026-0657(99)80018-6)
- Motaman, S., Mullis, A. M., Cochrane, R. F., & Borman, D. J. (2015). Numerical and Experimental Investigations of the Effect of Melt Delivery Nozzle Design on the Open- to Closed-Wake Transition in Closed-Coupled Gas Atomization. *Metallurgical and Materials Transactions B: Process Metallurgy and Materials Processing Science*, 46(4), 1990–2004. <https://doi.org/10.1007/s11663-015-0346-6>
- Motaman, S., Mullis, A. M., Cochrane, R. F., McCarthy, I. N., & Borman, D. J. (2013). Numerical and experimental modelling of back stream flow during close-coupled gas atomization. *Computers and Fluids*, 88, 1–10. <https://doi.org/10.1016/j.compfluid.2013.08.006>

- Osher, S., & Sethian, J. A. (1988). Fronts propagating with curvature-dependent speed: Algorithms based on Hamilton-Jacobi formulations. *Journal of Computational Physics*, 79(1), 12–49. [https://doi.org/10.1016/0021-9991\(88\)90002-2](https://doi.org/10.1016/0021-9991(88)90002-2)
- Patankar, S. V. (1980). *Numerical heat transfer and fluid flow*.
- Piomelli, U. (1992). *Numerical Solution of the Viscous Flow in an Atomization Die, NIST/Industrial Consortium on Intelligent Processing of Rapidly Solidified Metal Powders by Inert Gas Atomization*.
- Pryds, N. H., Hattel, J. H., & Thorborg, J. (1999). Quasi-stationary numerical model of atomized metal droplets. II: prediction and assessment. *Modelling and Simulation in Materials Science and Engineering*. <https://doi.org/10.1088/0965-0393/7/3/310>
- Rai, G., Lavernia, E., & Grant, N. J. (1985). Powder Size and Distribution in Ultrasonic Gas Atomization. *JOM*, 37(8), 22–26. <https://doi.org/10.1007/BF03257674>
- Rayleigh. (1882). Investigation of the character of the equilibrium of an incompressible heavy fluid of variable density. *Proceedings of the London Mathematical Society*. <https://doi.org/10.1112/plms/s1-14.1.170>
- Rayleigh, L. (1879). On the capillary phenomenon of jets. *Proceedings of the Royal Society of London*.
- Reitz, R. D., & Diwakar, R. (1986). Effect of drop breakup on fuel sprays. *SAE Technical Papers*. <https://doi.org/10.4271/860469>
- Reitz, R. D., & Diwakar, R. (1987). Structure of high-pressure fuel sprays. *SAE Technical Papers*. <https://doi.org/10.4271/870598>
- Roenby, J., Bredmose, H., & Jasak, H. (2016). A computational method for sharp interface advection. *Royal Society Open Science*, 3(11).
- Roenby, J., Larsen, B. E., Bredmose, H., & Jasak, H. (2017). A New Volume-of-Fluid Method in Openfoam. *VII International Conference on Computational Methods in Marine Engineering, MARINE 2017*, (February), 1–12.
- Sadhal, S. S. (2011). Transport Phenomena with Drops and Bubbles. In *Springer*. <https://doi.org/10.1007/978-1-4419-9872-9>
- Saeedipour, M., Schneiderbauer, S., Plohl, G., Brenn, G., & Pirker, S. (2017). Multiscale simulations and experiments on water jet atomization. *International Journal of Multiphase Flow*, 95. <https://doi.org/10.1016/j.ijmultiphaseflow.2017.05.006>
- Saha, A., Lee, J. D., Basu, S., & Kumar, R. (2012). Breakup and coalescence

- characteristics of a hollow cone swirling spray. *Physics of Fluids*.
<https://doi.org/10.1063/1.4773065>
- Shinjo, J., & Umemura, A. (2010). Simulation of liquid jet primary breakup: Dynamics of ligament and droplet formation. *International Journal of Multiphase Flow*. <https://doi.org/10.1016/j.ijmultiphaseflow.2010.03.008>
- Shinjo, J., & Umemura, A. (2011a). Detailed simulation of primary atomization mechanisms in Diesel jet sprays (isolated identification of liquid jet tip effects). *Proceedings of the Combustion Institute*.
<https://doi.org/10.1016/j.proci.2010.07.006>
- Shinjo, J., & Umemura, A. (2011b). Surface instability and primary atomization characteristics of straight liquid jet sprays. *International Journal of Multiphase Flow*. <https://doi.org/10.1016/j.ijmultiphaseflow.2011.08.002>
- Si, C., Tang, X., Zhang, X., Wang, J., & Wu, W. (2017). Characteristics of 7055Al alloy powders manufactured by gas-solid two-phase atomization: A comparison with gas atomization process. *Materials and Design*.
<https://doi.org/10.1016/j.matdes.2017.01.028>
- Strauss, J. (2000). Improvements in Close-Coupled Atomization: An Empirical Approach. *TMS Annual Meeting in Nashville, Tennessee*, 83–94.
- Strauss, J. T. (1999). Hotter gas increases atomization efficiency. *Metal Powder Report*. [https://doi.org/10.1016/S0026-0657\(00\)86269-4](https://doi.org/10.1016/S0026-0657(00)86269-4)
- Sussman, M. (1994). A level set approach for computing solutions to incompressible two-phase flow. *Journal of Computational Physics*.
<https://doi.org/10.1006/jcph.1994.1155>
- Sussman, M., & Puckett, E. G. (2000). A Coupled Level Set and Volume-of-Fluid Method for Computing 3D and Axisymmetric Incompressible Two-Phase Flows. *Journal of Computational Physics*. <https://doi.org/10.1006/jcph.2000.6537>
- Taylor, G. . (1950). The instability of liquid surfaces when accelerated in a direction perpendicular to their planes. II. *Proceedings of the Royal Society of London. Series A. Mathematical and Physical Sciences*.
<https://doi.org/10.1098/rspa.1950.0086>
- Thompson, J. S. (1948). A Study of Process Variables in the Production of Aluminum Powder by Atomization. *Journal of the Institute of Metal*, 74, 101–132.
- Thompson, J. S., Hassan, O., Rolland, S. A., Sienz, J., & LSN Diffusion Ltd. (2016). The identification of an accurate simulation approach to predict the effect of operational parameters on the particle size distribution (PSD) of powders produced by an industrial close-coupled gas atomiser. *Powder Technology*, 291, 75–85. <https://doi.org/10.1016/j.powtec.2015.12.001>

- Thomson, W. (1871). XLVI. Hydrokinetic solutions and observations . *The London, Edinburgh, and Dublin Philosophical Magazine and Journal of Science*.
<https://doi.org/10.1080/14786447108640585>
- Ting, J., Anderson, I. E. (2004). A computational fluid dynamics (CFD) investigation of the wake closure phenomenon. *Materials Science & Engineering, A*, 379, 264–276.
- Ting, J., Peretti, M. W., & Eisen, W. B. (2002). The effect of wake-closure phenomenon on gas atomization performance. *Materials Science and Engineering A*, 326(1), 110–121. [https://doi.org/10.1016/S0921-5093\(01\)01437-X](https://doi.org/10.1016/S0921-5093(01)01437-X)
- Tong, M., & Browne, D. J. (2008). Direct numerical simulation of melt-gas hydrodynamic interactions during the early stage of atomisation of liquid intermetallic. *Journal of Materials Processing Technology*, 202(1–3), 419–427. <https://doi.org/10.1016/j.jmatprotec.2007.10.012>
- Tong, M., & Browne, D. J. (2009). Modelling compressible gas flow near the nozzle of a gas atomiser using a new unified model. *Computers and Fluids*. <https://doi.org/10.1016/j.compfluid.2008.11.014>
- Umemura, A., & Wakashima, Y. (2002). Atomization regimes of a round liquid jet with near-critical mixing surface at high pressure. *Proceedings of the Combustion Institute*.
- Unal, A. (1987). EFFECT OF PROCESSING VARIABLES ON PARTICLE SIZE IN GAS ATOMIZATION OF RAPIDLY SOLIDIFIED ALUMINIUM POWDERS. *Materials Science and Technology*.
- Ünal, A. (1989). Liquid break-up in gas atomization of fine aluminum powders. *Metallurgical Transactions B*, 20(1), 61–69. <https://doi.org/10.1007/BF02670350>
- Weber, C. (1931). Disintegration of liquid jet. *Math. Mech*.
- Weller, H. G., Tabor, G., Jasak, H., & Fureby, C. (1998). A tensorial approach to computational continuum mechanics using object-oriented techniques. *Computers in Physics*. <https://doi.org/10.1063/1.168744>
- Weller, Henry G. (2008). A New Approach to VOF-based Interface Capturing Methods for Incompressible and Compressible Flow. *Technical Report*.
- William, R. C. (2016). *The experimental analysis and simulation of the breakup of a liquid filament jetting from a rotary laminar spray nozzle*.
- Yoshizawa, A. (1986). Statistical theory for compressible turbulent shear flows, with the application to subgrid modeling. *PHYS. FLUIDS*, 29(7, Jul. 1986), 2152–2164. <https://doi.org/10.1063/1.865552>

- Yoshizawa, Akira, & Horiuti, K. (1985). A Statistically-Derived Subgrid-Scale Kinetic Energy Model for the Large-Eddy Simulation of Turbulent Flows. *Journal of the Physical Society of Japan*. <https://doi.org/10.1143/JPSJ.54.2834>
- Zeoli, N., & Gu, S. (2008a). Computational simulation of metal droplet break-up, cooling and solidification during gas atomisation. *Computational Materials Science*. <https://doi.org/10.1016/j.commatsci.2007.10.005>
- Zeoli, N., & Gu, S. (2008b). Computational validation of an isentropic plug nozzle design for gas atomisation. *Computational Materials Science*, 42(2), 245–258. <https://doi.org/10.1016/j.commatsci.2007.07.013>
- Zeoli, N., Tabbara, H., & Gu, S. (2011). CFD modeling of primary breakup during metal powder atomization. *Chemical Engineering Science*, 66(24), 6498–6504. <https://doi.org/10.1016/j.ces.2011.09.014>
- Zeoli, N., Tabbara, H., & Gu, S. (2012). Three-dimensional simulation of primary break-up in a close-coupled atomizer. *Applied Physics A: Materials Science and Processing*, 108(4), 783–792. <https://doi.org/10.1007/s00339-012-6966-7>
- Zhang, D. L. (2004). Processing of advanced materials using high-energy mechanical milling. *Progress in Materials Science*, 49(3–4), 537–560. [https://doi.org/10.1016/S0079-6425\(03\)00034-3](https://doi.org/10.1016/S0079-6425(03)00034-3)